ACTA METALLURGICA SLOVACA
2020, VOL. 26, NO. 4, 138-140

SHORT COMMUNICATION

KOSICE SELF-GOVERNING REGION AND THEIR INTERNATIONAL COOPERATION IN THE AREAS OF THE SPACE INDUSTRY AND AVIATION

Róbert Bidulský[1], Juraj Seman[1]*

[1]Košice Self-Governing Region, Námestie Maratónu mieru 1, 042 66 Košice, Slovakia

*Corresponding author: robert.bidulsky@vucke.sk, Office of the Košice self-governing region, Námestie Maratónu mieru 1, 042 66 Košice, Slovakia

Received: 24.11.2020
Accepted: 24.11.2020

ABSTRACT

The short communication presents the Košice self-governing region (KSK) potential and forming new international partnerships within the aviation and space sector via online meeting Slovak space tech day and Slovak aviation industry day. The main idea of the co-organize the event was to prove the position of KSK, as a space in which suitable conditions are created for development in the areas of the space industry and aviation. The basis is a long-term historical context in the form of educational and research institutions in the KSK, as well as their involvement in international cooperation projects. KSK intended to declare demand for investments and international cooperation in the areas of the space industry and aviation. The given industries have long been among the most technologically advanced (technical standards and regulations, the precision of production and production tolerances, research and development of materials, new processes, and applications in other industries).

Keywords: innovation; aviation; aerospace; technological transfer

SLOVAK SPACE TECH DAY AND SLOVAK AVIATION INDUSTRY DAY

The main idea of the event was to prove the position of the Košice Self-Governing Region (KSK), as a space in which suitable conditions are created for the development in the areas of the space industry and aviation. The basis is a long-term historical context in the form of educational and research institutions in the KSK, as well as their involvement in international cooperation projects (Slovak Academy of Science and JAXA, Faculty of Aviation, Technical University of Kosice).
KSK intended to declare demand for investments and international cooperation in the areas of the space industry and aviation. The given industries have long been among the most technologically advanced (technical standards and regulations, the precision of production and production tolerances, research and development of materials, new processes, and applications in other industries).
The advantage of both segments is their high-quality level and degree of sophistication and success in them is considered almost an automatic admission to any industry. At the same time, they represent the central government's efforts through economic policies to diversify the national economy, reduce automotive dependency, capture future trends and create high value-added jobs, as well as the usability of future investors to participate in the R & D & I ecosystem (Industry 4.0).
The original concept included a 4-day program, two focused on the conference part held in the East Slovak Museum (subsequently the venue was exchanged because of technical reasons for the East Slovak Gallery) and a weekend in which the Košice Aviation Days are traditionally held by KSK and at the same time it is one of the most visited events of the year. The premises of the *Aeroclub* in the form of a VIP lounge were to serve as a background for B2B meetings of the KSK management and conference participants - potential investors.

Due to the pandemic spread of the COVID - 19, the Aviation Days in Košice were cancelled, which halved the scope of the event. The subsequent development of the pandemic situation caused a change in the format of the event from full-time to distance one (online).
Despite the unfavorable circumstances, the event can be considered a success, as it is clearly stated in the following indicators:

- 86 registered participants
- 88 confirmed B2B negotiations
- 20 countries

The clear outputs of the event include the following facts:
- meetings with various national and international organization, for example: Japan External Trade Organization (JETRO), **Fig. 1**, Hong Kong Trade Development Council, Hong Kong Economic and Trade Office Berlin, Korea Trade-Investment Promotion Agency (KOTRA), Changzhou Productivity Promotion Center, Jiangsu Province, P R China, Embassy of Japan in the Slovak republic, British Embassy in the Slovak republic, Ministry of Economy of the Slovak Republic, Ministry of Foreign and European Affairs of the Slovak Republic, Ministry of Education, Science, Research and Sport of the Slovak Republic, Slovak Investment and Trade Development Agency (SARIO), Slovak Liaison Office for Research and Development (SLORD).
- All Nippon Airways (ANA) as a Keynote of the Slovak Aviation Industry Day [1]
- ANA entered the Slovak market for the first time in the summer of 2019, when during the visit of the director of JETRO - Japan External Trade Organization, the airline presented itself in Slovakia for the first time in the history at the reception of the chairman of KSK, *Rastislav Trnka*:
- KSK hosted negotiations taking place between representatives of Košice Airport and VP General Manager of ANA

- ANA was subsequently a participant in the Business Mission of Japan in the Slovak Republic, whose opening reception, as well as the 2-day programme, was provided by KSK, **Fig. 2**

Fig. 1 Official visit to JETRO Vienna HQ, from left: Takuro Nozawa, Juraj Seman, Róbert Bidulský, Eckhart Derschmidt

Fig. 2 Opening reception of the Business Mission of Japan in the Slovak Republic, from the left: Juraj Seman, Rastislav Trnka, Róbert Bidulský, Boris Vaitovič

- As a result of the Business Mission, ANA established a Sales Representative for Slovakia
- JETRO informed more than 275 Japanese companies operating in the EU about the involvement of ANA

Profile of the ANA:

- established in 1952 as a helicopter transport service
- 28 employees at the time of establishing
- current situation: 43 466 employees
- fleet of 264 aircraft
- 5-star rating from SKYTRAX 8 years in a row (since 2013)

Also, significant output was the participation of the Hong Kong International Airport (HKIA) in the program provided by KSK, as well as the subsequent B2B with KSK representatives. The inclusion of a Hong Kong entity fully reflects the ambitions of KSK's management to join the international transport and logistics network, also known as "Belt and Road". The conference on this project was attended in 2019 by a KSK delegation led by the chairman of KSK, *Rastislav Trnka*.

Close and systematic cooperation with Hong Kong Trade Development Council (HKTDC) was a necessary pre-requisite for the possibility of engaging the HKIA entity in terms of size and importance. An equally important role was played by the change of the technology platform. By exchanging Zoom - a platform whose use for the needs of the public administration is not recommended by the NBU - National Security Office. The recommendation not to use the given platform was issued on April 10, 2020. An alternative solution was to use the CISCO Webex platform, whose 5 valid licenses were purchased by the KSK office. Another important consequence of the change in the platform was the acceptability of mutual interaction for partners from Asia, where, especially in the case of some types of political regimes, the use of the Zoom platform is out of the question.

Profile of the HKIA:

- 78,000 employees
- 100 airlines
- No.1 Cargo Airport of the World (continuously since 2010)
- 3rd busiest airport in the world in passenger international transport
- 71.5 mil. of transported passengers (2019)

Previous ongoing negotiations and working trips to Italy in the field of Innovation, Research and Technology Transfer for companies in the Piedmont region showed the success of presentations of the intention to establish the "*Košice Regional Institute of Innovation and Technology*" for additive production and innovation technology potential of the Košice region. The 15 innovative companies, representatives of educational institutions and universities, as well as national institutions responsible for R & D & I in the field of aerospace.

Juraj Seman, President's Executive Advisor for Foreign Affairs & Protocol at Košice Self - Governing Region opens expert panels mainly dedicated to the Asian Innovation in Aviation. Long-term negotiations with foreign representatives of the regions, or representatives of university clusters and consortia in Asia and Europe led to the successful presentation of several important representatives of the space industry, *Le Xuan Huy*, Deputy Director of the Vietnam National Satellite Center presented Vietnamese industrial applications, satellite researches and the development of the space technology institute in Vietnam and the first Vietnamese satellite "PicoDragon" [2, 3]. *Dang Quoc Khan*, Hanoi Science and Technology University, Vietnam, presented works at the School of Materials Science and Engineering, Hanoi University of Science and Technology, mainly research in Materials Engineering. The interesting research fields are iron and steel alloys, especially abrasion and corrosion resistance alloys for mining and chemical industrial applications such as High Manganese Steel, High Chromium Cast Iron (White Cast Iron) [4]. Chinese professors, *Wei Wei*, executive director of the Sino-Russian Joint Laboratory for Functional Nanostructured Metals, and *Jing Hu*; Vice-Dean of the School of Materials Science and Engineering, Changzhou, University presented the possibilities of cooperation with KSK for advanced materials [5, 6]. *Róbert Bidulský*, authorized representative for innovation and technological transfer at Košice Self - Governing Region opens the last session related to the European Innovation in Space & Aviation. *Bruno Vicenzi*, Technical Director of EPMA, presented the reasons why, in terms of the entry of Slovak companies, universities, scientific clusters, it is necessary to have a European leader in the field of powder metallurgy as a partner [7]. *Marco Actis Grande* presented a world-class extra for additive technologies and possibilities of use in the aerospace industry, and also showed the possibilities of cooperation with KSK [8, 9]. *Ľudmila Kučerová* shows recent development of high strength or even ultra-high strength steels as a mainly driven factor for the aviation industry which strives to reduce the weight of individual parts, fuel consumption, and CO_2 emissions [10].

The undoubted outcome of the conference is 4 memorandums of cooperation:

- Changzhou Science and Technology Bureau, Jiangsu Provincia,
- European Powder Metallurgy Association,
- Consorzio Interuniversitario Nazionale per la Scienza e Tecnologia dei Materiali, consortium of

Italian national universities in the R & D & I field of materials,
- Toyama prefecture.

CONCLUSION

Slovak space tech day and Slovak aviation industry days were mainly devoted to current trends in the space industry, as well as the application of a wide range of technologies, such as information and telecommunication technologies, production of innovative materials and many others. Slovak Aviation Industry Day, which was held for the first time, focused mainly on such areas as the production of aircraft and components, software solutions and innovations in air transport. The programme also includes expert panels organised by Košice Self-governing region and online B2B matchmaking with Slovak companies and institutions.

REFERENCES

1. H. Kondo, M. Hegedus: Acta Metall. Slovaca, 26(4), 2020, 141-143. https://doi.org/10.36547/ams.26.4.763.
2. P.A. Tuan, L.X. Huy, N.T. Thanh: Proceedings of the International Astronautical Congress, IAC 13, 2015, 10182-10186.
3. P.A. Tuan, L.X. Huy: Human resource programs for space technology and application in Vietnam. In.: *60th International Astronautical Congress 2009*, IAC 2009, Daejeon; South Korea, Volume 5, 2009, p. 3486-3491, Code 80592.
4. H. T. H. Dang, P. T. Thuy, D. M. Ngung, P. Quang, V. Y. Shchukin: Acta Metall. Slovaca, 24(1), 2018, 43-51. https://doi.org/10.12776/ams.v25i1.1218.
5. K.X. Wei, L. Niu, W. Wei, Q.B. Du, Q.B. I.V. Alexandrov, J. Hu: Acta Metall. Slovaca, 24(1), 2018, 43-51. http://dx.doi.org/10.12776/ams.v24i1.1021.
6. W. Mei, J. Wu, M. Dai, K. Wei, J. Hu: Acta Metall. Slovaca, 25(2), 2019, 130-135. https://doi.org/10.12776/ams.v25i2.1271.
7. B. Vicenzi, K. Boz, L. Aboussouan: Acta Metall. Slovaca, 26(4), 2020, 144-160. https://doi.org/10.36547/ams.26.4.656.
8. D. Manfredi, R. Bidulsky: Acta Metall. Slovaca, 23(3), 2017, 276-282. https://doi.org/10.12776/ams.v23i3.988.
9. E. Pošković, F. Franchini, M. Actis Grande, L. Ferraris, R. Bidulský: Acta Metall. Slovaca, 23(3), 2017, 276-282. https://doi.org/10.12776/ams.v23i4.1032.
10. H. Jirková, K. Opatová, Š. Jeníček, J. Vrtáček, L. Kučerová, P. Kurka: Acta Metall. Slovaca, 25(2), 2019, 101-106. https://doi.org/10.12776/ams.v25i2.1267.

ACTA METALLURGICA SLOVACA
2020, VOL. 26, NO. 4, 141-143

LETTER TO EDITOR

CURRENT TRENDS AND CHALLENGES IN THE GLOBAL AVIATION INDUSTRY

*Hironobu Kondo[1], Martin Hegedűš[1]**

[1] All Nippon Airways CO., LTD., Objekt 680/Office Park 1, Wien - Flughafen, Wien, 1300 Austria

*Corresponding author: m.hegedus@ana.co.jp, All Nippon Airways CO., LTD., Objekt 680/Office Park 1, Wien - Flughafen, Wien, 1300 Austria

Received: 20.11.2020
Accepted: 25.11.2020

ABSTRACT

This paper is based on Slovak Space Tech Day 2 & Slovak Aviation Industry Day keynote speech from Hironobu Kondo and Martin Hegedűš. It shortly described All Nippon Airways (ANA) as a company and the trends and issues of the aviation industry from ANA perspective, furthermore future projects and prospects. It gave insights into the efforts of ANA to battle the carbon footprint of the company, social aspects of the globalized world, and cooperation of multiple elements to achieve a better and more sustainable future for all of us, nonetheless measures taken to fight against the spreading of the Covid-19. Information was obtained from official All Nippon Airways sources, statistics, and press releases. To conclude paper described the reason and significance of aviation and the need to adjust according to the new standards.

Keywords: innovation; aviation; aerospace; travel; drone

ANA ORIGIN

Following the "Inspiration of Japan" high quality of service, ANA has been awarded the respected 5-Star rating every year since 2013 from SKYTRAX. Additionally, ANA has been recognized by Air Transport World as "Airline of the Year" three times in the past 10 years - 2007, 2013, and 2018, becoming one of the few airlines winning this prestigious award for multiple times.

ANA was founded in 1952 with two helicopters and 28 employees, and has become the largest airline in Japan, as well as one of the most significant airlines in Asia, operating 42 international routes and 52 domestic routes.

ANA has been a member of Star Alliance since 1999 and has joint venture partnerships with United Airlines, Lufthansa German Airlines, Swiss International Airlines, and Austrian Airlines. Besides the full service and award winner carrier ANA, the ANA Group has merged two LCCs, Vanilla Air Inc. and Peach Aviation Limited, into one consolidated subsidiary - Peach. The ANA Group carried 59.6 million passengers in FY2019, has approximately 45,000 employees, and a fleet of 260 aircraft. ANA is a proud launch customer and the biggest operator of the Boeing 787 Dreamliner.

ANA lives by the Japanese motto:

"Anshin, Attaka, Akaruku-Genki!" = "Trustworthy, Heartwarming, Energetic!" This motto represents ANA's way which consists of 5 elements:

Safety - This is our utmost priority, our promise to the public, and is the foundation of our business. It is enhanced through individual performance and dedication. Safety is the most important element of the aviation business.

Customer Orientation - We create the highest possible value for our customers by viewing our actions from their perspective. Right after the safety, the customer is priority #2, customers are the reason why we exist.

Social Responsibility - We are committed to contributing to a better, more sustainable society with honesty and integrity. Pilots, technicians, administrative or ground staff, we all work as one team, we coordinate and use our resources in the most efficient way to make our customers happy towards a sustainable future.

Team Spirit - We respect the diversity of our colleagues and come together as one team by engaging in direct, sincere, and honest dialogue. From Japan to India, Australia, Russia, Germany, or Slovakia our goals are the same but not our cultures. We respect our nature and differences and we bond to become a better, even more emphatic, and honest society.

Endeavor - We endeavor to take on any challenge in the global market through a bold initiative and innovative spirit. It will be 68 years, in December 2020, our company has been constantly adjusting, evolving, and overcoming any challenge in front of us. During these hard times, we are dedicated even more to be the global leading airline group by satisfying our customers and creating value.

ANA CARE PROMISE

To battle the increasing risk of spreading the virus and to reassure all the passengers traveling with us ANA has introduced a set of new requirements and safety precautions called "ANA Care Promise".

At ANA, we promise to create a safe, comfortable, and enjoyable experience for all passengers. Safety and peace of mind is our number one priority and is considered at every stage of the journey. In the following 5 areas we took numerous measures to demonstrate we will do all in our powers to adapt during such a troubling time and show to our customers their safety and feeling of security is our highest priority:

- Before departure
- Security area
- Lounges

- Gate area
- In-flight

Of course, there are some special services and measures taken to respective areas but in general, we can speak about following measures: All the staff wearing Facial Covering and Face Shield, Installation of vinyl curtains and transparent acrylic panels, Installation of disinfectants and hand sanitizers, Securing Social Distance, Disinfection of equipment, Temperature measurement, Improved Lounge Services, Precautions on busses, Improved Boarding Procedure, Cleaning and Disinfection of Aircraft, Cleansing Wipes, In-flight Service, Ensuring air circulation in the cabin

Current situation and the New Normality

The whole aviation industry was hit exceptionally hard by the Covid-19 pandemic resulting in a decrease in passenger and cargo transportation. On average since April 2020 in our case, the decrease in passenger transportation is around 96% on international routes and 84% domestic, that said in other words there are only 4% operable international passenger flights and 16% domestic. We estimate to close FY2020 with a 5 billion USD deficit.

For the first time in modern history, when we have the technology to travel daily from the Pacific to Europe and back in just 2 days, humankind is facing the global pandemic restricting us from traveling. We literally cannot travel, borders are closed, and quarantines are taken in place. The core of our business, moving people, disappeared in just a couple of months. Meetings, discussions even contracting is being held online. Visiting friends or relatives, exploring the world? Sometimes impossible. This is what we have to fight and overcome.

We are facing other issues as well. Aging population on the one side, and the booming population on the other. In Japan people aged 65 and older make up 1/4 of its population, by 2050 it's estimated to reach 1/3. In Europe in 2019 more than 1/5 (20.3%) were aged 65 and over. On the other hand, there is a booming population in India and Africa, people will want to travel, to explore, to visit friends and family and if there is a chance we will be there for them. Not just ANA, but the whole aviation industry will have to reflect the changes and evolve.

We became a partner of the United Nations Development Programme (UNDP) and integrated 17 sustainable development goals into our own goals.

To reduce the carbon footprint ANA flew with Boeing 777-300ER from Everett, Washington to Japan using LanzaTech's sustainable aviation fuel (SAF) produced from waste gas derived ethanol. Earlier in 2019 ANA already purchased 70 thousand US Gallons of SAF and used it on commercial flights from San Francisco to Tokyo. ANA signed Offtake Agreement for Sustainable Aviation Fuel allowing ANA to purchase SAF in the future and was also selected by the New Energy and Industrial Technology Development Organization (NEDO) - a prominent Japanese public research and development body - to develop integrated production technology for sustainable aviation fuel and bring it to market. ANA was chosen after a comprehensive review process to conduct studies on the production and commercialization of LanzaTech's sustainable aviation fuel and will work alongside Mitsui & Co., LTD., and JXTG Energy to achieve these goals. ANA and its partners will work together to construct a supply chain for sustainable aviation fuel as part of a process that is aiming to achieve large-scale commercial production of sustainable aviation fuel in Japan with ANA providing detailed research on the impact of fuels developed through this partnership.

Boeing B787 aircrafts and Airbus A320/A321neo aircrafts are the most efficient and effective aircrafts currently available, therefore ANA is centering purchase of new aircraft on these advanced models.

We adopted next-generation coating to be even more efficient and we are lightening passenger seats in collaboration with Toyota Boshoku.

The ANA Group has developed its own dedicated vehicle to clean the engine compressor leading to a reduction of the fuel by 1% annually.

ANA tests self-driving electric bus at Haneda International Airport.

We have 2.5% employees with disabilities, as part of our diversity efforts, we increased the hiring of people with disabilities.

There are 14.6% women in management positions, we have 5 women in ANA's top executive positions and more than half of our employees are women. ANA ranked third place in Japan for 100 best companies for women in 2015.

At the end of September 2020, Japan Aerospace Exploration Agency (JAXA) and ANA Holdings Inc. announced Joint Research on Remote Sensing Observation of Atmospheric Components using Passenger Aircraft and Satellites. Since 2009, JAXA has been monitoring the increase of greenhouse gas on a global scale by Greenhouse Gases Observing Satellite "IBUKI" (GOSAT). The greenhouse gas emissions from city areas are estimated to account for approximately 70 - 80% of anthropogenic CO2 emissions. However, achieving both observations on the amount of greenhouse gas emissions associated with human activities in the city and on a global scale is difficult for satellites. In this joint research, the carry-on luggage sized the observation instrument developed by JAXA applying space technology will be placed in the cabin of passenger aircraft operated by ANA. This instrument observes the detailed concentration distribution of the atmospheric components such as carbon dioxide and nitrogen dioxide while flying over cities. The purpose of this research is to understand the emission distribution in city areas according to emission sources such as traffics and industries by combining the data obtained by aircraft and satellites such as "IBUKI". First, we start this observation experiment flight between Tokyo (Haneda) and Fukuoka.

Furthermore, this research aspires to contribute to the Paris Agreement by providing useful data for considering measures to reduce emissions from cities and for evaluating the effect of emission reduction efforts.

ANA's Future

Space project

In cooperation with PD Aerospace Co., Ltd. and H.I.S. Co., Ltd., and other shareholders, we are working on a fully reusable suborbital spacecraft that will be capable of alternating combustion methods between jet mode and rocket mode, and capable of take-off and landing like ordinary aircrafts. In outer space, we will be able to provide a microgravity environment during ballistic dives from high altitude for several minutes, allowing for filming and other experiments opportunities. It can be applied to the various fields of science, research, industry, and other services. On the earth, a multipurpose observation service is suitable for observations of dangerous areas that require a prompt response (Local weather observation, large scale disaster, etc.), **Fig. 1**.

In this project, our role will be to take care of the flight operation, daily maintenance, ground operation, and customer service, exactly as with our daily passenger or cargo flights. Currently, we are at the key elemental technology development phase for unmanned spaceplane. Unmanned flight was planned for 2020 but it seems due to pandemic it will be postponed for

2021. The manned commercial flight was planned for 2024 after certification in Japan.

Fig. 1 Fully reusable spacecraft by PD AeroSpace

Drone project

In Zambia, ANA is working with drone firm Aerosense Inc. and the National Center for Global Health and Medicine to build a sustainable drone transportation network for blood samples, **Fig. 2**. This will allow people to get proper healthcare in hardly accessible places where infrastructure is missing or is not developed yet.

Fig. 2 One of the drone prototypes being used for the logistics development

ANA will be also building drone infrastructure and with the partners will work together to establish a logistics network that uses drones to improve delivery between the remote islands of the Japanese Goto City.

Avatarin Inc.

Humanity has evolved over 6 million years. And in that process, discoveries and inventions were constantly being made.
With the mastery of fire, humans learned how to stay warm, to live in groups, to cook meat, and our physique grew stronger. With the domestication of livestock, in particular horses, humans started traveling to faraway lands, leading to the creation of empires, where cultures were born. With the invention of letterpress printing, the ability to store and communicate information increased dramatically. With the invention of the steam engine came the industrial revolution, which allowed humans to travel even farther. With the invention of the car, travel time was shortened even more. With the invention of the airplane, the distance traveled by humans increased dramatically, thus becoming the cornerstone of a connected world. With the invention of the internet, humans were able to obtain information anytime, anywhere.
Humans have experienced tremendous progress. The shift from walking to flying has increased the distance we can travel dramatically at a fraction of the time. Yet, to go to the other side of the Earth, it takes more than half a day, no matter how fast the airplane.
But now - finally, humans will be unbound by the limitations of distance. Instant transportation will be possible, no matter how far. Avatars will make this possible. While sitting in bed at home, be instantly transported to a place far away, gaze at giant sea creatures at an aquarium, enjoy shopping, and even fish in the vast ocean. You may think, "but isn't that just in a virtual world?" But when vision, hearing, and sensations are completely synchronized, the human consciousness is in the same exact state as being there. These experiences are indeed, real. Yes, with Avatars, humans will no longer be bound to distance or to their bodies and will be able to move instantly to anywhere they desire, making it possible to experience everything the world has to offer. A new invention that accelerates humanity is right before your eyes. In the not so distant future, Avatars will be installed everywhere. People will "avatar-in", using smartphones and VR goggles going anywhere as they please and experiencing those unique moments that can only be experienced by being there. Building a lunar base and exploring the deep-sea, all the while staying on land. This too, will become commonplace. A world where everyone can "avatar-in" to experience the reality of all kinds. The door to a new world is now open.

AVATAR X

ANA and JAXA have partnered to create AVATAR X, a collaborative program for the advancement of space exploration and development using Avatar technology. The initiative is part of ANA's overarching ANA AVATAR Vision and JAXA's new research and development program, J-SPARC (JAXA Space Innovation through Partnership and Co-creation), which was created to encourage new innovative collaborations between JAXA and the private sector.
AVATAR X will bridge the gap of science fiction and non-fiction. We aim to bring scenes like those found in the popular Japanese comic series "Space Brothers" to life, by making remote operation of Avatar robots on the surface of the Moon and treatment of patients on space stations in Low Earth Orbit by doctors on Earth a reality.
But the AVATAR X movement will not end there. We will continue to push the limits of Avatars beyond the lunar surface to Mars, and further into deep space.

CONCLUSION

The significance of the aviation industry remains unchanged. We connect people and businesses, transport goods, and materials. We would like to make sure you meet the people you would like to meet when you would like to meet them. Go when and where you want to go. However, it is necessary to tune up according to changes in the environment. Nothing is going to be the same in our business after we beat the Covid-19 pandemic. But that's what the current life on earth is about, constantly changing, adapting to the new normality. This is what we do from the beginning and this is what we will always do.

ACTA METALLURGICA SLOVACA
2020, VOL. 26, NO. 4, 144-160

RESEARCH PAPER

POWDER METALLURGY IN AEROSPACE – FUNDAMENTALS OF PM PROCESSES AND EXAMPLES OF APPLICATIONS

Bruno Vicenzi[1], Kenan Boz[1], Lionel Aboussouan[1]*

[1] European Powder Metallurgy Association, 1 Avenue du Géneral de Gaulle, F-60500 Chantilly (France), www.epma.com

*Corresponding author: bv@epma.com, tel.: +33 (0)344 581 524, European Powder Metallurgy Association, 1 Avenue du Géneral de Gaulle, 60500 Chantilly, France

Received: 14.08.2020
Accepted: 20.09.2020

ABSTRACT

Powder Metallurgy (PM) is one of the technologies that are going to play an important role in manufacturing in all sectors in the future, including aerospace, as it can combine the ease of alloying with net shape capabilities, freedom of design and high performance. Over the years, several different processes have established, each with distinctive features, using dedicated metal powders, and delivering materials that rival the properties of conventionally produced ones. The portfolio of available compositions, properties and part shapes is constantly increasing and penetration in many sectors, including automotive and aerospace, is also deeper year by year. Especially Additive Manufacturing, the latest big development in powder metallurgy, is attractive because of the unprecedented possibilities of weight optimization to obtain at the same time a lower mass and outstanding performance. In this review, a number of examples of applications in aerospace taken from the available literature are shown.

Keywords: powder metallurgy; additive manufacturing; hot isostatic pressing; metal injection moulding; press&sinter; aerospace; case studies

INTRODUCTION

Powder Metallurgy (PM) [1, 2] is a wide range of technologies that allows for the fabrication of solid metal parts starting from elemental or prealloyed powders of almost any kind of metal, and it relates and combines with similar technologies and methods for the fabrication of even more complex materials including ceramics. The main reason for the success of PM in many fields is in fact the ease of alloying, as this can ultimately be obtained even just by mixing of appropriate powders. Sintering, i.e. heat treatment under suitable atmospheres (and sometimes added external pressure) but below the melting range of the bulk material, is also used in most of the PM processes to obtain a solid body, with a shrinkage from the initial formed shape or not, although some remarkable exceptions have been developed over the years where conventional sintering is not the densification step.
Among PM processes we can list:

- The common, and most widely used, Press&Sinter (P&S) route, consisting of compressing the powders in rigid dies, ejecting the parts using the movements of the punches, and sintering them into solid components after removal of the lubricants contained in the parts to aid compaction.
- Metal Injection Moulding or Molding (MIM), where the powders are mixed with an organic "binder" to confer the ability of being injection moulded, like in the case of plastics, into moulds: the complex shaped components are then treated to remove the binder and sintered to the final (almost full) density.
- Hot Isostatic Pressing (HIP), where the powders are poured into a sealed metal container with a suitable shape (simple but sometimes already with some geometrical details) and then pressed isostatically at high temperature to compact them to almost full density (to be distinguished from Cold Isostatic Pressing that is only a way to compact powders at room temperature, prior to sintering).
- Metal Additive Manufacturing (AM), that is a family of methods all starting from metal powders, where the parts are built by 3D printing addition of layer after layer. This can happen in:
  - Beam Based AM: a beam of focused energy (laser, or electron beams, normally) is guided by a CAD-driven 3D actuator to "draw" sections of the part in a bed of powders, melting them so that a solid section is prepared. After that, the base on which the part is gradually built is lowered by a typical layer thickness of a few tens of microns and a new layer of powders is deposited on top, so that a new layer can be drawn and welded and the part can grow layer by layer. This process is not requiring sintering as the part coming out of the printer is already a solid metal part.
  - Sinter Based AM: similar technique to the beam based, but without powder melting, as the powders are just "glued" by inkjet printing so that the printing is quicker than in the beam based. On the other hand, printed parts need to be treated to remove the binder and then sintered in a furnace like for MIM parts. In a variant, Fused Filament Fabrication, a powder/binder mixture feedstock shaped into thin wires is extruded and deposited in sections to build the parts, that need as well debinding and sintering afterwards.
  - Direct Deposition, where a flow of heated (with a laser, plasma, etc.) powders or a wire is impacted on the surface of the part to add another

section. This technique does not require subsequent sintering and can be seen as a variant of the Beam Based methods.
- Other densification techniques, like Fast Sintering, Spark Plasma Sintering, Field Assisted Sintering, etc., which combine high temperature obtained quickly by flowing a strong electrical current through the powders with the mechanical pressing of the softened body via punches. These techniques are normally exploiting much quicker densification processes that are not activated in common sintering and are less used in industrial production.

Sometimes the process includes a combination of techniques, like for instance when HIP is used on already dense parts to achieve full density, like in MIM + HIP or AM + HIP processes.
PM also includes of course all the technologies for the production of metal powders, the widest share of which is represented by the various atomization processes from the metal melt, that can be tuned to obtain powders with different particle size and particle size distribution, and particle shape. Different PM processes will normally use different powders, larger of finer, rounder or more irregular and so on.
In this paper we will discuss in some details the various PM technologies, and finally show several applications of these to aerospace parts.
The authors belong the European Powder Metallurgy Association, that gathers most European companies and research groups devoted to PM.

MAIN POWDER METALLURGY PROCESSES

Production of metal powders

Metal powders are the common denominator of all powder metallurgical processes. They are produced in many ways and variants and are available nowadays in a very wide range of chemical compositions, size, size distribution, and shapes. The possibility of further mixing among different powder compositions and grades opens the field to a virtually infinite number of starting points for the fabrication of complex and performant materials.
Apart from composition, the further processing and the properties achieved in the PM final solid part are influenced by the characteristics of the powder [3], like:
- particle size and size distribution
- particle shape
- particle bulk structure and surface condition
- that are strongly dependent on the powder production process.

We will give here just a short description of the main production routes, namely:
- Atomization
- Chemical routes
- Mechanical routes

Atomization

Atomization [4] is the source of most of the powders used in common powder metallurgy processes, like Press&Sinter, MIM, HIP and AM. It is the choice when the metal composition can reasonably be produced from the melt, thus for instance iron based compositions, that are by far the bulk of the global consumption, are normally produced this way, and also for the production of copper, tool steels, alloy steels, brass, bronze and the low melting point metals, such as aluminium, tin, lead, zinc and cadmium.
It consists in melting the alloy in a suitable crucible, with the usual metallurgical procedures to control the composition and the impurities, and then letting the melt flow through a nozzle at the bottom of the crucible so that a thin stream of molten metal is created. Very close to the nozzle orifice, this stream is impacted by a strong high-pressure jet of gas or liquid (normally water) and "atomized" into small droplets that while further falling in the container below cool and solidify into metal particles that are collected at the bottom of the container and sieved or classified to separate them in different size classes.
There is normally a clear difference between powders atomized in water and powders atomized in inert or protective gas: because of the different mechanical and thermal properties of the atomizing media, gas atomized particles of the larger sizes are very round in shape, almost spherical or anyway rounded, whereas water atomized powders appear irregular in shape. Also, atomizing in water brings to a higher O content in the final composition, that must be reduced afterwards or anyway taken into account. The readily oxidizable metals (e.g. chromium-bearing alloys) are thus being atomized on an increasing scale by means of inert gas, especially argon.
Depending on nozzle geometry, gas or water pressure, and other parameters, the particle size distribution obtained with these processes can be changed, so that the yield in a certain size fraction can be optimized. Atomized powders will have different particle size distributions, often with a peak at a characteristic size, and tails at lower and larger sizes. Sizes may vary from submicron and micron size to 150 μm or more. The so-called close-coupled nozzle design is usually more suitable to produce finer powders, in the range below 50 μm, thus MIM and AM powders, whereas larger powders can be obtained with the simpler free fall design.
In more recent developments, rotating cups, plates or cones (or just a rotating bar of the source alloy which is heated at one end) on which the metal melt is centrifugally forced to produce radially travelling droplets that solidify in a very controlled atmosphere, allow the production of very clean (but larger) powders of highly reactive metals (centrifugal atomization).
An interesting procedure to fabricate alloyed powders consists in atomizing a master alloy, for instance even just Fe or Fe-Cr, mixing it with finer alloying powders (like Mo, etc.) and heat treating the mixture so that the smaller particles stick to the larger base powders by contact and diffusion. Each final particle contains roughly the final composition, even if alloying will have to be completed during the sintering, later. This gives the possibility of having a softer matrix, with very good compressibility during compaction, whereas a fully alloyed powder could be difficult to process by simple pressing.

Fig. 1 Gas atomizer for fine metal powders (courtesy Atomizing Systems Ltd)

Chemical routes

Even before atomization was developed, solid state reduction was for a long time the most widely used method to produce iron

powder from crushed ore mixed with carbon and passed through a continuous furnace. This brings to a cake of sponge iron which is then further crushed, purified from impurities, and sieved. The purity of the powder, soft irregular sponge-like particles that readily compressible, is dependent on that of the raw materials. Refractory metals are normally made by hydrogen reduction of oxides, and the same process can be used for copper.
Electrolysis can be used for many metals to deposit them in a spongy or powdery state, and then by washing, drying, reducing, annealing and crushing the relevant powders are obtained. Copper is the main metal to be produced in this way, but chromium and manganese powders are also produced, and in the past even iron, but environmental regulations are making production less and less popular.
Thermal decomposition of a chemical compound is used in some cases, like in the Carbonyl Process, that was originally developed to refining Ni. Crude metal was made to react with carbon monoxide under pressure to form the carbonyl which is gaseous at the reaction temperature and which decomposes on raising the temperature and lowering the pressure. The same process is used for iron, and carbonyl iron powder finds small scale application where its very high purity, and its small grain size (1-5 µm), is useful.
Thermal decomposition is used for platinum powder (from platinum ammonium chloride) and Ni (by hydrogen reduction of a solution of a nickel salt under pressure).
Chemical precipitation of metal from a solution of a soluble salt is used in other cases, e.g. Ag, and Co. Powders of the latter are also produced by reduction of cobalt carbonate powder, produced by chemical precipitation with CO_2, starting from cobalt amino-sulphate solution.

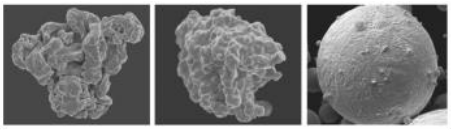

Fig. 2 Left to right: Sponge iron powder NC 100.24 (courtesy Höganäs AB); atomized iron powder ASC 100.29 (courtesy Höganäs AB); spherical ex-carbonyl iron powder

Mechanical routes

Mechanical comminution is normally used for brittle materials such as inter-metallic compounds, ferro-alloys (ferro-chromium, ferro-silicon, etc.). These are mechanically comminuted in ball mills sometimes with very high impact energies, a process (particle-to-particle welding, embrittlement by mechanical strain, fracture, etc.) that can also be used for mechanical alloying of heterogenous powders, even for mixtures that would not normally form alloys. Powder shapes and sizes can very but the shape is normally very irregular, usually platelet-like, while the size can even reach the submicron range, so behavior in the subsequent process is strongly influenced. Other special processes, like the Coldstream Process (used to reduce the size of coarsely atomized powder) can be included in this category.

Press&Sinter

The Press&Sinter process [5] is so established that it is commonly referred to as "powder metallurgy" or "conventional powder metallurgy" [5] as it has been the dominating process since its adoption, although PM is truly the name of the set of processes using metal powders, and not just of this particular route.
The process is shown schematically in Fig. 3. The powders are mixed homogenously together with a lubricant, poured to fill a die and compacted under pressure (or no pressure to obtain porous bodies as e.g. bronze filters), after which the compact is sintered and can later be subjected to further post-treatments.

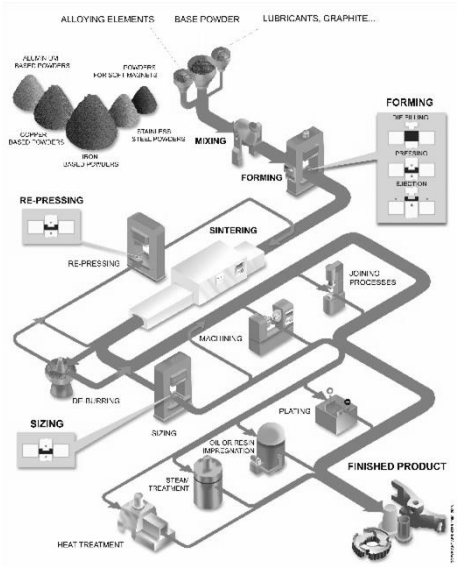

Fig. 3 Scheme of the Press&Sinter process

Mixing

Mixing provide a homogeneous mixture comprising the powders and the lubricant (usually stearic acid, stearin, metallic stearates, especially zinc stearate, and increasingly, other "waxy" organic compounds). The choice of the lubricant and its amount must take into account the need

- to be easily removed during or better before sintering without unwanted residues or reactions,
- not to reduce the maximum attainable density during pressing by occupying excessive volume in the mixture,
- to have a flowable mixture that will evenly fill the compaction die.

Compaction

The mixed powders are pressed to shape in a rigid steel or carbide die under pressures of 150-900 MPa. The tools to impart the desired geometry are mounted in hydraulic or electrical presses, with several independent highly precise punch and die movements. Depending on geometry, the tools may have relatively thin or relatively bulky punches and features, thus the maximum safely attainable pressure to avoid tool damages can be lower (e.g. only 600 MPa) or higher (even more than 1000 MPa), choosing a compromise between part density and tool wear. After pressing, the compacts maintain their shape because of cold-welding of the powder grains within the mass and are sufficiently strong to withstand ejection from the die and subsequent handling before sintering.
The final shape and mechanical properties are essentially determined by the level and uniformity of the as-pressed density. Powders under pressure do not behave as liquids, the pressure is not uniformly transmitted, and very little lateral flow takes place within the die. The attainment of satisfactory densities therefore depends to a large degree on press tool design and the actual

pressing procedure. To produce parts safely, the tool must be designed [7] with several factors in mind:

- Length-to-Width-Ratio: because of the compression behavior of the granular material, the pressure locally applied and therefore the density decrease over the length of the compact: this can be strongly reduced by lubrication and double-sided compaction, but a lower density region at the middle section of the part is unavoidable, so length-to-width ratios in excess of 3:1 are not recommended.
- Reverse tapers and lateral holes cannot be normally produced by pressing because of the impossibility of ejection (they are normally machined afterwards), although elaborate, sometimes flexible die assemblies have been designed, patented and industrially used that overcome this limitation.
- Bevels require feather-edged tools, which are fragile and easily fractured; so, if design permits, the beveled edge of the component should end in a small flat.
- Abrupt changes in sections should be avoided since they introduce stress raisers, which may lead to crack formation especially during ejection.

Roughly, the size of the part that can be made is a direct function of the capacity of the press available, but the complexity of the part and number of punch motions also play a role. The simpler the part, the easier it is to press at high speed, up to roughly 1 part per second, but 10 parts per minute is a typical compaction rate for parts of comparatively simple geometry.

Special variants include: warm compaction, where the material and/or the die itself are heated to a point where the yield stress of the powder is significantly lower, attaining thus higher compact (and final) densities with lower amount of lubrication; hot pressing, where the temperature is so high (a special high temperature press is needed) that densification happens during pressing (also used for non-metallic parts); and high velocity compaction, where a more impulsive pressing is imparting compaction in milliseconds.

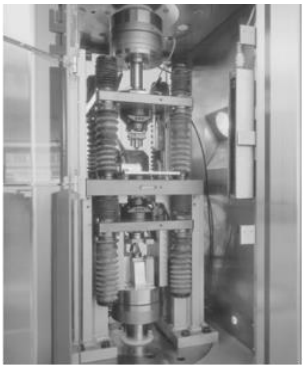

Fig. 4 Powder compacting press (courtesy Fette GmbH)

Another possibility for compacting finer powders is to cold press them isostatically (Cold Isostatic Pressing, CIP [9]) using rubber moulds ("wet" or "dry" bag variants) immersed fully or partially into a fluid (water/oil emulsions or similar) that is brought to high pressure and held under pressure for a few minutes, typically at 200 MPa (2000 bar, for powders mixed with binders) and up to 700 MPa (for pure metal powders). The compacts can then be treated for sintering, although they are previously machined to a more complex shape (the shape complexity attainable with the CIP is somewhat basic, although some features, like internal cylindrical cavities, for instance, can be achieved by using rigid steel inserts in the mould). Dry bag systems are preferred when productivity is a critical factor, whereas wet bag systems are normally used for larger parts with lower production volumes.

Sintering

During sintering the compact acquires the strength needed to fulfil the intended use. In general, sintering is a thermal treatment of a powder or compact at a temperature below the melting point of the main constituent, for the purpose of increasing its strength by bonding the particles together [15]. At a such temperature, atomic diffusion takes place with various mechanisms and the welded areas formed during compaction grow until eventually the primary particles may be lost completely. Recrystallisation and grain growth usually happen, pores in the part tend to become rounded and the total porosity, as a percentage of the whole volume, tends to decrease.

Due to the high reactivity of the powders, sintering is carried out under a protective atmosphere (H_2, N_2/H_2 mixtures, dissociated ammonia, exo- or endogas produced from hydrocarbons, depending on the material to be sintered, to achieve the right control over oxides, carbides and other unwanted phases), at maximum temperatures between 60 and 90% of the melting-point of the particular metal or alloys (this might mean, for powder mixtures, that the sintering temperature may be above the melting-point of the lower-melting constituent, e.g. copper/tin alloys, iron/copper structural parts, tungsten carbide/cobalt cemented carbides, hence the term "liquid phase sintering", but the amount of liquid phase must be low in order to avoid impairing the shape of the part). During the first part of the cycle, at lower temperatures, the lubricant, if present, is removed thermally. Heating rate, time, temperature and atmosphere control is required for reproducible results. Generally, electrically heated continuous belt furnaces are preferred, with typical sintering temperatures up to 1150°C, but higher temperatures (up to 1350°C) can be achieved with the walking beam design.

In recent years new types of sintering furnaces allow low alloy steel parts to be sintered with neutral carbon potential (without decarburization or carburization) and then to be hardened in a rapid cooling zone (sinter hardening).

For special applications batch vacuum or hydrogen furnaces are used, normally when higher temperatures are needed.

Sintering can be enhanced under certain conditions, like for liquid phase sintering. In activated sintering, a special "activator" (normally finer powders or an alloying component), may be used to promote diffusion at the early stages, sometimes by reacting with the thin oxides on particle surfaces. In sintering of iron alloys, a ferrite phase stabilizer can be added so that the much higher self-diffusion of iron in ferrite compared to austenite can be exploited.

Sintering leads to progressively increased strength by diffusion-driven welding of the primary particles. Generally, the part tends to increase in density as well, with an overall shrinkage; but in some systems even a growth may happen, because of gases that develop inside the part during the process or, in reactive sintering mixtures where alloying takes place during sintering (e.g. Cu diffusing into Fe), because the new phase formed by the alloying has a higher volume. Under controlled plant conditions, reproducible size change can be maintained, and this must be foreseen in the design and manufacture of tools, but it is increasingly practiced balancing the composition and sintering regime so that no dimensional change takes place. As dimensional change is influenced also by compact density (the lower, the greater the tendency to shrink), this is one of the reasons why uniformity of density of the compact is of such importance. If there is significant variation from one part to another the differential dimensional change in the various sections can lead to warpage.

Final sintered parts normally achieve a density ranging from slightly below 90% and about 95% of the theoretical density, with typical values for most popular compositions and parts just above 90%.

Fig. 5 Continuous belt sintering furnace (courtesy Mahler GmbH)

Further treatments and variants

Many treatments can be carried out on sintered parts to improve them for several aspects.
In repressing, an improvement of the already good tolerances is achieved (sizing and coining), with often an associated density increase. When followed by a second sintering, this is normally referred to "double pressing -double sintering".
As an extreme, if a simple blank is produced by sintering it can be forged, i.e. hot repressed in a closed die [8]. This is very popular especially for automotive high strength applications and is named powder forging.

Fig. 6 Powder forged connecting rods (courtesy Metaldyne Sintered Components)

Even HIP (see below) can be used on pressed parts, but this is normal for special materials like cemented carbides, not for steel or metal parts in general.
A further surface densification can be achieved by Surface Cold Rolling, that is common for gear teeth, and resembles a "localized" repressing.
As porosity is a typical feature of pressed&sintered parts, as it might represent 5-12% of the body of the part (and ranging from completely interconnected to not interconnected depending on part density), there are treatments that use or try to compensate the presence of porosity.
Infiltration is a method of improving the strength of inherently porous sintered parts filling the surface connected pores with a liquid metal having a lower melting point (e.g.: ferrous parts using copper as infiltrant). This can be used also to make composite electrical contact materials such as tungsten/copper and molybdenum/silver.
In impregnation the pores are filled with an organic as opposed to a metallic material: oil-impregnated bearing materials are the best example, but also thermo-setting or other plastic materials are used, to increase mechanical properties or seal of the pores (for pressure-tightness or to prevent the entry of potentially corrosive electrolyte during a subsequent plating operation), or to improve part machining.
Heat treatment is very common for steels, that often are used just as sintered or sized, but many times are supplied in the hardened and tempered condition (frequently sinter hardened, see above). If steel density does not exceed 7.2 g/cm^3, interconnected porosity imposes the use of processes where heating is done in a gas atmosphere, followed by oil-quenching. Similarly, PM parts can be carburized and carbonitrided, but again gaseous media are indicated, and porosity will bring the effect inside the first layers of the part so the 'case' is generally deeper and less sharply defined than with fully dense steels.
Steam treatment is a process peculiar to PM steel parts: exposing them at a temperature around 500°C to high pressure steam, a layer of magnetite (iron oxide) forms on all accessible surfaces and:

- corrosion resistance is increased by the filling of some of the porosity;
- the reduction in porosity of the surface layer leads also to improved compressive strength;
- the oxide layer significantly increases the surface hardness and the wear resistance.

At a lower temperature (200-250°C) in air a thin magnetite layer that gives some increase in corrosion resistance, but it is much less effective than steam treatment, is formed ("blueing").
As mentioned earlier, with a previous impregnation in case of interconnected porosity, parts can be plated, e.g. with copper, nickel, cadmium, zinc, or chromium plating. are all used.
Parts are also often machined, for several reasons: usually because of limitations to the geometry that can be pressed in rigid dies, for example for transverse holes. Although porosity alters the machining characteristics and in general tool wear is greater than with the same composition in the fully dense form, with carbide tools and relatively low cutting speeds this is quite possible.
Deburring, and tumbling, sometimes in a liquid medium with an abrasive powder, is normally employed to remove machining burrs.
Parts can be joined by welding or brazing, although special care may again be needed to accomplish for open surface porosity.

Materials and typical applications

P&S is commonly used to produce a wide variety of materials and parts.
It is also used to produce non-metallic materials and composites like metal matrix composites, cemented carbides [10], diamond cutting tools [11], and ceramics, that are not discussed here.

Structural Parts:

The bulk of structural P&S parts, that means parts with a mechanical function, is based on iron, but significant quantities of copper, brass, nickel silver, aluminium and bronze parts are made.

Ferrous structural parts are the core of the P&S offer, and are usually chosen by customers for cost reduction, yet performing the function, over the cast or machined counterparts. The net shape capability of the powder route avoids costly machining and, in the end, proves to be a winner, despite the reduced properties deriving from the residual porosity.

In order to be cheap, compositions are based on iron, with additions for strength starting from simple C and Cu; to achieve better properties, Ni and Mo have been added (frequently by diffusion alloying), and more recently also Cr, Mn and Si have been gradually introduced to obtain better hardening.
As properties are strongly depending from density, techniques for density improvement, many of which have been listed above, have been introduced: a special mention must be made for powder forging, that has the great advantage of reaching almost theoretical density. Simultaneously, an effort to expand the limits in geometrical features is continuously undertaken by the major producers and some very clever solutions for, e.g. transversal details are nowadays used in industrial practice for many parts.
These advances both in geometrical complexity and performance level have led to a great expansion in the types of P&S ferrous structural part applications.
The automotive sector is the dominant customer industry for P&S structural parts: worldwide, 75-80% of these go to the automotive sector. Engine (timing pulleys, sprockets and hubs, valve train parts like valve seat inserts, valve guides, valve timing control and coupling devices, balancer gears, main bearing caps, engine management sensor rings, oil and water pump gears) and transmission (synchronizer system parts, clutch hubs, gear shift components, planetary gears and carriers, turbine hubs, clutch and pocket plates) components are particularly important, accounting for at least 70% of total automotive usage (other parts include shock absorber components like piston rod guides, piston valves and end valves, Anti-lock Braking System (ABS) sensor rings, exhaust flanges and oxygen sensor bosses out of P&S stainless steel, gears and bearings in small electric motors, door lock parts)
P&S ferrous structural parts are also popular in a number of important non-automotive markets, like DIY hand power tools, domestic appliances, business machines, leisure and garden, industrial motors and controls, and general hardware like lock parts, latches, etc.).

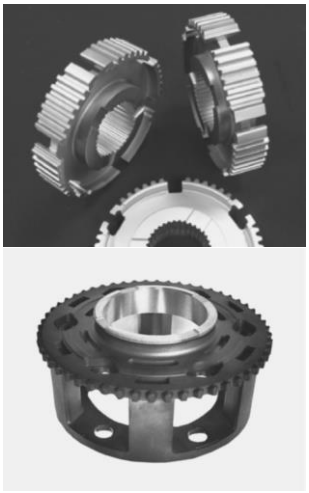

Fig. 7 Left: Synchronizer hubs for automotive (courtesy PMG Füssen); right: planetary carrier for automotive transmission (courtesy AMES SA)

Non-ferrous structural parts: The production of structural parts in non-ferrous materials is on a much smaller scale but significant quantities of copper, brass, nickel silver, and bronze parts are made, and the production of aluminium from powder is now developing, driven largely by the automotive sector's desire for weight reduction. Camshaft bearing caps have emerged as a leading application for P&S aluminium parts. Aluminium can of course be considered for some aerospace applications for weight reduction.

Bearings and filters

The advantage of porosity is used to produce bearings. As explained, the pores can be filled with lubricating oil, so that the bearing requires no further lubrication during the whole life of the machine in which it is used. The pores form an interconnected system of controlled size and volume, so that oil is supplied to the entire bearing surface and the rate of oil supply automatically increases with temperature and, therefore, with increasing speeds of rotation, to achieve optimum working conditions. Election material is bronze, or sometimes iron, iron copper, or iron mixed with bronze is used.
Alternatively, copper/lead or copper/tin/lead (leaded bronze) non-porous bearings can be also produced.
Controlled porosity is also employed in the manufacture of metal filters and diaphragms out of bronze (e.g. 89/11 Cu/Sn), copper, nickel, stainless steel and 'Monel', and are widely used for the filtration of fuel oils, chemical solutions and emulsions, separating liquids of varying surface tension (like water from fuels in jet engines), or sound damping on air compressors and the like.

Friction Materials

Sintered metal friction components, consisting essentially of a continuous metal matrix, into which varying amounts of non-metallic friction generators, such as silica and emery, but also copper, tin, iron, lead, graphite, carborundum, alumina and asbestos substitutes are bonded, are particularly useful for heavy-duty applications, e.g. aircraft brakes, high speed train brakes, race cars brakes, heavy machinery clutch and brake linings etc. The resistance to wear is superior to resin-bonded materials, and therefore, permits the use of components of thinner section. Compared with solid phosphor bronze or aluminium bronze friction elements, the sintered material offers many advantages, the most important is probably the much wider range of friction characteristics, which can be obtained from variations in the dispersion of non-metallic particles, that is a feature distinctive of powder metallurgy

Magnetic and Electric Components

A range of soft magnetic materials can be processed by P&S [12], like iron, silicon-iron and iron with about 5% of phosphorus, overcoming difficulties due to the limited ductility of the alloyed compositions. These are widely used in the manufacture of pole pieces and armatures for DC application.
For AC applications, minimized eddy current losses can be obtained via the Soft Magnetic Composite (SMC) materials. In these materials, the individual powder particles are insulated from one another by a resin addition, which is cured in a baking process after compaction, so that the thickness of the flux path becomes equivalent to the powder particle size, i.e. very small. Sintering in the accepted sense is not required, the parts are just pressed, cured and stress relieved. Cores for self-inductance coils in high-frequency communication equipment are a typical application.
Sintered high-permeability laminated components in nickel-iron and permalloy-type materials are also used for transformer applications.
Soft ferrites or magnetic oxides have the widest application in the manufacture of cores for radio and television.

But especially the hard magnets are nowadays mostly processed by P&S: hard ferrites (maybe over 90% of the current market by volume), AlNiCo, CuNiFe and CuNiCo, but also Sm-Co, and later Nd-Fe-B magnets are all successful examples.
Composite structures attainable only by powder metallurgy methods have been used extensively in the manufacture of electrical contacts and current collector brushes, combining the desirable conducting properties and low contact resistance of silver or copper with the strength, heat-resistance, and resistance to arc erosion of tungsten, molybdenum, nickel, etc., or with the lubricating qualities of graphite.

Metal Injection Moulding

A technology developed in the 1980's and that started gaining industrial significance in the 1900's is Metal Injection Moulding [13, 16]. Stemming from the sister technology developed for ceramics, it combines the ease of shape fabrication of injection moulding with the typical powder metallurgical advantages of alloying and net shapes, with the bonus that the use of very fine powders brings to very high, sometimes, almost theoretical, sintered densities. In its basic form (See the scheme in Fig. 8) it includes the fabrication of the so-called feedstock, a mixture of metal powders and organic binders, the injection moulding into the desired shape, the removal of the organic binders, and the sintering at high temperature to almost full density. Due to its characteristics, it suits especially small parts with high demands in terms of properties, and large series.

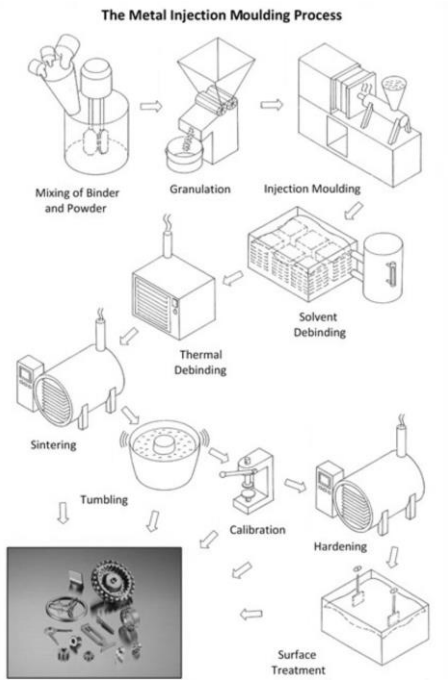

Fig. 8 Scheme of the Metal Injection Moulding process

Feedstock compounding

The powders for MIM are somewhat specific as they must possess properties that are quite different from the ones necessary for P&S and other part fabrication routes. The powders are not mechanically deformed during the process, so they can be as alloyed as desired, on the other hand they have to be highly flowable, able to mix well with the organic binders, and finally with high sinterability to achieve the high density. Thus, the ideal MIM powder is normally very fine (even <20 μm) but with a wide particle size distribution, and spherical. Nevertheless, applications to other less ideal powders are possible and the tuning of the mixing can compensate for that.
The organic binders are normally thermoplastic polymers and waxes, with other additions to ease wettability to the powder and decrease or control mixture viscosity and other features.
In the mixing, a volume ranging from about 50% to about 70% of powders are added to a complementary part of organic binders (usually a mixture of different components) and mixed in the melting range of the binders, by extrusion or shear rolling or kneading, until the desired homogeneity is achieved. This high fraction of binders determines one of the important factors in the MIM process, i.e. the shrinkage during sintering (compare with Press&Sinter, where the lubricant has a volumetric fraction of some %). The cooled and granulated feedstock can be subsequently moulded.
Feedstock technology is the characterizing point in the process, and affects the rest of the steps, injection moulding (via its rheology), debinding (via the route for removal) and sintering (via the residual debinding and the shrinkage). Nowadays a significant fraction of the feedstock is made by specialized companies, although some producers prepare their mixes in-house.

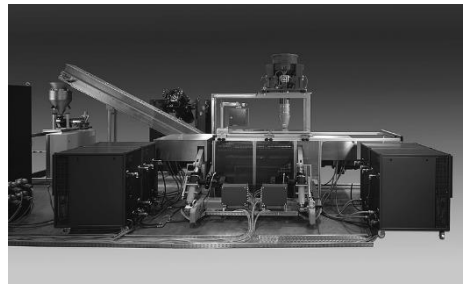

Fig. 9 Shear roll mixer for metal injection moulding (Courtesy Bellaform GmbH)

Injection moulding

Injection Moulding in MIM is somewhat similar to the injection moulding of plastics, as the equipment (injection moulding presses and accessories) are the same (with small but important modifications) and tool designs can be similar (but normally with more wear resistant tool steels to accomplish for the higher wear). The injection moulding of the metal feedstock itself, however, is more complex, as rheology is affected by the different properties of the mixture. Furthermore, all defects introduced in this phase are likely to be amplified by the subsequent steps, so although the process is truly offering a wide freedom of shape, mould design and part design must be addressed properly, to avoid or reduce distortion, flow lines, junction lines, powder and binder separation and errors in final dimensions, taking into account the specific properties of the feedstock used (flowability, green strength limitations, etc.). Design guidelines are available with general recommendations about thickness, sizes, tolerances, position of injection gates, etc., and respecting them is preferable, although some challenging parts have been produced successfully. An "ideal" design will deliver the best properties at the lowest cost and effort.

The mould must be oversized by a factor (mould or shrinkage factor) to compensate the shrinkage during sintering and sometimes slightly unbalanced oversizing factors in different areas should be considered to compensate for later deformation in sintering. Many cavities can be placed in the same mould (normally copies of the same part to avoid unbalanced injection) and that enhances productivity.
For a typical thermoplastic feedstock, the process starts with the loading of the press by rotating the screw inside the heated barrel and bringing the molten feedstock to the front of the screw; then the screw is brought forward with a precisely controlled movement to push the feedstock (maximum pressures are around 1000 bar typically) though the mould channels until they reach the cavities and fill them. During a pressurization phase the injected material cools and solidifies in the cavities, then the screw rotates again to load more material for the next injection, and the mould is opened and the parts pushed out of the cavities via ejection pins. Parts are checked and normally placed onto trays for the debinding. The solidified channels (sometimes minimized using heated sections in the mould) and all scrap parts are separated but can normally be recycled in later mouldings by remixing, improving process efficiency.

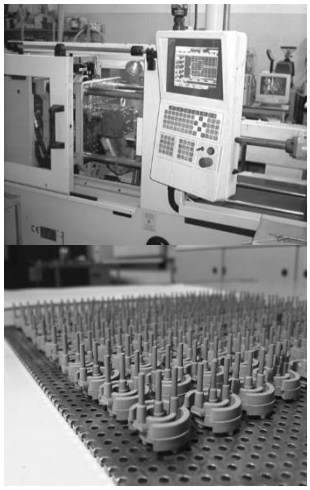

Fig. 10 Left: injection moulding press; right: moulded MIM parts placed on trays

Debinding

Debinding is the binder removal process, and is very dependent on the feedstock selected, that dictates the debinding strategy. The modern approach to binder removal includes normally 2 steps: the first is carried out separately but the second is normally executed inside the sintering furnace. The first step is normally one of these:

- a solvent debinding, where a solvent (even water for some binders) is used to remove the soluble ingredients of the binder by immersing the parts at low temperature in it;
- a thermal debinding, where the parts are exposed to temperatures where the polymer binder evaporates and extracted by gas flow or vacuum in the debinding furnace;
- a catalytic debinding, exploiting the decomposition of POM feedstock using gaseous nitric acid or oxalic acid (very popular)

All these processes can be carried out in batch or continuous debinding equipment.
After the debinding the parts contain a small residue of the original binders, tend to be fragile and sometimes difficult to handle but maintain roughly the same dimensions as green parts. Careful debinding is needed to avoid warping, blistering, cracking, and subsequent problems in sintered parts (for instance, due to insufficient binder removal in some areas of the parts).
The secondary debinding is normally a thermal step and as anticipated is carried out during sintering.

Fig. 11 Left: catalytic debinding furnace (courtesy Nabertherm GmbH); right: solvent debinding units (courtesy Lömi GmbH)

Sintering

The high temperature sintering process brings the parts to their final size. Depending on the initial binder volume content the linear shrinkage is between 12 and 20% (mostly 15-18%). As sintering is a thermal diffusion process based on thermodynamics, it is the surface energy per volume of the fine MIM particles, much higher than that of coarse particles, that strongly promotes the diffusion of atoms, pushing the final density much higher than the sintering process of Press&Sinter, usually above 96% of the theoretical density of the alloy applied.
Sintering is performed in high temperature (just below the melting temperature) batch or continuous furnaces applying process gas (hydrogen, nitrogen, argon) or vacuum. The time-temperature-atmosphere scheme of the process is critical, a slower ramp and hold for secondary thermal debinding is sometimes needed and then the sintering temperature can be reached safely: MIM steel components are sintered between 1200°C and 1400°C depending on their specific chemical composition, but each material can have different optimal sintering schedules.
Special care must be placed in the choice of the ceramic materials for the trays and support of the parts (MIM parts have complex geometries and generally might need shaped supports to avoid gravitational slumping during sintering), as the high shrinkage can cause sticking and warping if the friction is not ideal, especially for heavier parts.

Fig. 12 Top: batch debinding and sintering furnace for MIM (courtesy Elnik Systems); bottom left: continuous debinding and sintering furnace for MIM (courtesy Cremer Thermoprozessanlagen GmbH); bottom right: MIM parts placed on special sintering supports to avoid distortions

Further treatments and variants

Metal injection moulded parts achieve a sufficiently high density after sintering, normally well above 96% of theoretical, to allow for most standard post-treatments, including deburring, surface finishing (even at very low R_a values, almost mirrorlike), coating and plating, and of course heat treatment, machining and mechanical deformation (sizing, coining, bending and straightening) when the alloy has sufficient ductility in the sintered state. Being normally net or near net shape parts, thermal treatments require suitable atmospheres as the part surfaces should not be damaged by oxidation or other surface contaminations.
MIM is actually a family of different processes, one for each binder variant, as binder properties influence mixing, mould design, injection moulding, debinding and partly sintering.
Extrusion is starting to be used to produce profiles, by using MIM feedstocks and applying the rest of the process on the extruded and solidified products. This experience is partly used in the Fused Filament Fabrication additive manufacturing route (see below).
For some alloys, even using fine powders, sintering is made difficult by the very tight sintering window in temperature (due to the small difference between solidus and liquidus), hardly attainable with industrial furnaces, so the common practice is to sinter the parts at a lower "safe" temperature to a lower final density but make use of Hot Isostatic Pressing (see below) to achieve full densification. The same procedure can be applied on already dense components for highly critical applications (in aerospace for instance) where no residual porosity or other internal defect is tolerated.

By using special presses and moulds, two-component MIM is possible, to combine in the same part for instance a magnetic and a non-magnetic steel, or a hard and a soft steel, or even metal and ceramic materials. Although this is not standard practice and a careful choice of feedstocks and processing conditions must be made to comply with all demanding requirements for the co-sintering of different materials, the first industrial applications are becoming reality.
The MIM process lends itself to produce micron-sized feature in very small parts, in a process variant named microMIM.

Materials and typical applications

Almost all metals that can be processed to obtain suitable MIM powders (usually spherical and fine) have been successfully processed by MIM, with some exceptions like aluminium and magnesium, whose oxide surface film and low sintering temperatures make industrial production difficult. A short list would include low alloy steels, stainless steels, tool steels and high speed steels, nickel based superalloys, cobalt alloys, copper alloys, titanium, intermetallics, magnetic alloys, refractory metals and hardmetals (cemented carbides), but the portfolio is constantly expanding. Even if the fine powders have a definitely higher cost than wrought steel and even compared to the powders used for P&S, the net shape capabilities of MIM can be leveraged to best effect for high value alloys as process scraps that are associated with machining are minimized.
In terms of volume, almost 50% of the global production is related to stainless steels, with 316L and 17-4 PH as main contributors (consumer electronics has been a large customer in the recent decades, especially in Asia where most of the production of mobile phone frames and electronics is undertaken), followed by low alloy steels and other steels. Titanium and superalloys are steadily increasing also because of the growth of applications in engines and turbines, some of which in aerospace applications.
Some examples of MIM aerospace parts will be shown in a following chapter. Other typical sectors for MIM are medical (orthodontics, special tools), consumer parts (watch cases and components, eyewear parts, the mentioned mobile phone and electronic parts), firearms (mechanical parts in smaller weapons), automotive (many small parts in sensors and actuators, and esthetic parts), electrical and hand tool parts, textile machinery parts, general industrial machinery parts, etc.

Hot Isostatic Pressing

Hot Isostatic Pressing (HIP) is a process to densify powders or sintered parts (or even cast parts) in a furnace at high pressure (100-200 MPa) and at temperatures from 900 to 1250°C, for example for steels and superalloys [17, 18]. The gas pressure acts uniformly in all directions to provide isotropic compression and 100% densification. It provides many benefits and has become a viable and high-performance alternative to conventional processes such as forging, casting and machining in many applications. Its positioning is very complementary to other PM processes such as MIM, P&S, or the new AM technologies. It is even used in combination with these PM processes for further part densification and the production of semi-finished bars or slabs.
A wide range of component types can be manufactured thanks to HIP. Its capabilities include large and massive near net shape metal components such as oil & gas parts weighing up to 30 tons, or net shape impellers up to one meter in diameter. Equally it can be used to make small PM High Speed Steel cutting tools, such as taps or drills made from PM HIP semi-finished products, which can weigh less than 100 grams, or even very tiny parts such as dental brackets. As a result, HIP has developed over the

years to become a high-performance, high-quality and cost-effective process to produce many metal (or ceramic) components.

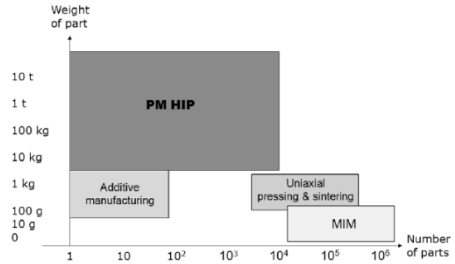

Fig. 13 Positioning of PM HIP technology vs. other PM technologies (source O. Grinder, Euro PM2009 Congress & Exhibition)

The production of a PM HIP component is leaner and shorter than usual conventional metallurgy processes, and the cost of HIP relative to energy and materials costs has decreased by 65% over the last two decades.
Main process steps are:

1. Container design and manufacturing
2. Container filling with powder and sealing
3. Hot Isostatic Pressing
4. Container removal
5. Post processing operations

Container Design and Manufacturing

Container manufacturing involves the following steps:

- Container sheet cutting and forming/shaping
- Assembly of steel sheets and optionally pipes and metallic inserts by TIG welding
- Leak testing, by evacuating the container and introducing helium or argon under pressure. If a leak is detected and located, repair is undertaken.

The integrity of welds is critical, otherwise when the vessel is pressurized, argon will enter the container and become entrapped in the powder mass. The argon will remain in the material and argon-filled pores will strongly deteriorate the mechanical properties.

Container filling with powder and sealing

Fig. 14 Example of container construction with filling/evacuation tubes (courtesy Rolls Royce)

Once assured that the container is leak-free, the powder is introduced via a fill-tube. In order to achieve maximum and uniform packing of the powder, which is necessary to ensure a predictable and consistent shrinkage, a vibration table is used, so that the powder better fills narrow spaces and remote areas. In special cases such as critical aerospace applications, the filling operation is done under inert gas or vacuum to minimize contamination of the powder.
The next step is outgassing to remove adsorbed gases and water vapor. After outgassing, the fill tube is welded under vacuum to seal the container. As explained, the absence of leaks is critical.

The Hot Isostatic Pressing Process

During the hot isostatic pressing process, the temperature, argon (in special applications, other gases or gas mixtures are used) gas pressure and holding time will vary depending on the material types. After filling and closing, the HIP vessel is evacuated to eliminate the air. Then, while heating up, Argon gas pressure is increased in the vessel. After reaching a set pressure by a compressor, the further increase in pressure is done through gas thermal expansion by heating. The gas pressure is equal inside and outside the insulation. But the gas density is higher outside the insulation than inside because of the lower temperature. In the holding time, gas pressure and temperature are constant. Chosen temperatures are below approx. $0.8 \cdot T_{solidus}$, to avoid having a liquid phase.
After this, a rapid cooling takes place, with decreasing pressure and temperature. Modern HIP systems can feature Uniform Rapid Cooling (URC) which circulates lower temperature gas to cool the part at a controlled rate of up to 100°C/min. The HIP quenching technique cuts cycle time dramatically by shortening the cooling stage by as much as 80%. It also provides the benefit of combining heat treatment with HIP in a single step. The URC restricts grain growth and thermal distortion of the parts and avoids surface contamination by using high purity argon gas. A HIP treatment cycle usually lasts from 8 hours up to 24 hours.
A HIP unit consists mainly of a pressure vessel, a heating system and an Argon gas system. Various HIP constructions are available:

- with or without a frame (for pressures above 100 MPa and HIP diameters above 900mm, frame construction is chosen for safety reasons)
- with or without top screw thread locking systems
- with different heating systems

Molybdenum furnaces are used for temperatures up to 1350°C and carbon graphite/tungsten furnaces up to 2200°C. Inside the pressure vessel, insulation (ceramic fibers and Molybdenum sheets) is used to protect the steel pressure vessel against the heat and to hold the high temperature inside the insulation. The bottom, cover and pressure vessel are water cooled to protect the sealing ring and the vessel against the heat. In large HIP units, diameters can reach 2200 mm and height of more than 4000 mm, with a capacity of up to 30 tons.

Fig. 15 Large-scale HIP unit (courtesy MTC/Avure)

After HIP, the container can be removed (when the container is not to be re-used) by machining, acid pickling or slipping off. After container removal, various additional operations can take place, including heat treatment, machining, finish grinding and surface treatment. Depending on the size and value of the parts being made various types of quality testing will be undertaken. Two of the most common are ultrasonic testing and dye penetrant inspection. CAT scanning is also used in critical high value applications.

Materials and typical applications

In addition to standard or customized compositions of steels, HIP is used for nickel-base and cobalt-base alloys, but also for titanium, copper, lead, tin, magnesium and aluminium alloys. As during hot isostatic pressing the elements do not have time to segregate like in cast parts, because the temperature is below the melting point, new alloy compositions can be successfully produced, like tool steels for higher wear or temperature resistance, stainless steels for high corrosion resistance in difficult environments, and even composite materials, e.g. wear resistant metal and ceramic composites.
Typical application sectors are aerospace, automotive, energy (even very large parts like valves, manifolds, rotors and impellers), tooling and wear resistant parts for manufacturing equipment, etc.

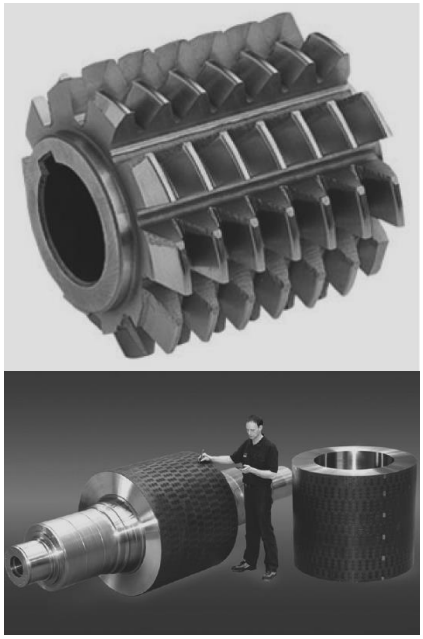

Fig. 16 Top: HIPped high speed steel automotive gear cutter (courtesy Erasteel); bottom: tool steel clad grinding roll for cement processing impeller (courtesy Köppen)

Metal Additive Manufacturing

Additive manufacturing, according to the ASTM standard F2792-10, is the "process of joining materials to make objects from 3D model data, usually layer upon layer, as opposed to subtractive manufacturing methodologies, such as traditional machining" [19]. Additive manufacturing technologies for metals are numerous, hence the development of a wide variety of terms and acronyms, as can be seen in the graph below. But today Additive Manufacturing (AM) is the most common term in industry markets while 3D printing is more used in the consumer market. An overview of metal additive manufacturing processes is given in Fig. 17.

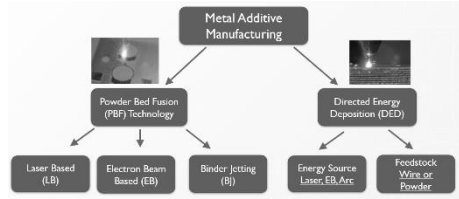

Fig. 17 Mapping of main metal powder additive manufacturing technologies

The use of AM with metal powders is a new and growing industry sector with many of its leading companies based in Europe. It became a suitable process to produce complex metal net shape parts, and not only prototypes, as before. Additive manufacturing now enables both a design and industrial revolution, in various industrial sectors such as aerospace, energy, automotive, medical, tooling and consumer goods.

AM for complexity

Metal additive manufacturing technologies offer many key benefits. The design ideas referring to maximum performance, or minimum weight that cannot be realized by conventional manufacturing techniques such as casting, and machining, are usually possible by AM. In general, the process is recommended for the production of complex parts in small series.
Benefits of AM technology can be summarized as:

- Increased design freedom versus conventional casting and machining.
- Light weight structures made possible either by the use of lattice design or by designing parts where material is only where it needs to be, without other constraints. This procedure is normally referred to as "topology optimization".
- New functions such as complex internal channels, or several parts built in one.
- Net shape process meaning less raw material consumption, up to 25 times less versus machining, important in the case of expensive or difficult to machine alloys. The net shape capability helps creating complex parts in one step only thus reducing the number of assembly operations such as welding, brazing.
- No tools needed, unlike other conventional metallurgy processes which require molds and metal forming or removal tools.
- Short production cycle time for complexity: complex parts can be produced layer by layer in a few hours in additive machines. The total cycle time including post processing usually amounts to a few days or weeks and it is usually much shorter than conventional metallurgy processes which often require production cycles of several months.

Beam based Technologies

In beam-based powder bed systems (LBM or EBM), a powder layer is first applied on a building platform. Then a laser or electron beam selectively melts the upper layer of powder. After melting, the platform is lowered and the cycle is repeated until

the part is fully built, embedded in the powder bed. During laser beam melting, the laser beam, with diameter of the order of 100 µm, will locally melt the upper powder layer on the powder bed. The laser will be partially absorbed by metal powder particles, creating a melt pool which solidifies rapidly. Laser power typically varies from 200 W up to 1000 W.

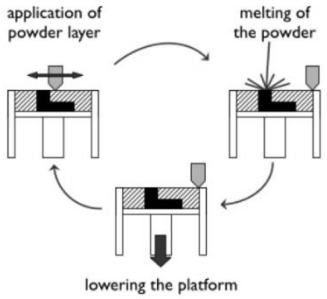

Fig. 18 The powder bed manufacturing cycle (courtesy Fraunhofer)

In the laser beam melting process, a powder layer is first applied on a building platform with a recoater (blade or roller) and a laser beam selectively melts the layer of powder. Then the platform is lowered by 20 up to 100 µm and a new powder layer is applied. The laser beam melting operation is repeated. After a few thousand cycles (depending on height of the part), the built part is removed from the powder bed.

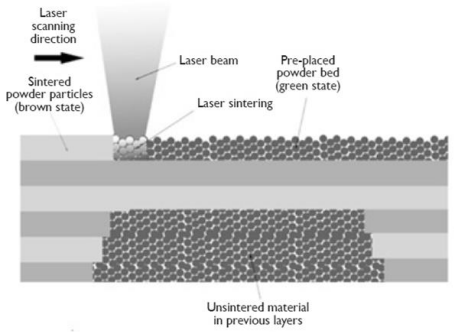

Fig. 19 Cross sectional view of the Laser Beam fusion process in powder bed

The Electron Beam Melting (EBM) process is based on a high-power electron beam that generates the energy needed for high melting capacity and high productivity. The electron beam is managed by electromagnetic coils providing extremely fast and accurate beam control. The EBM process takes place in vacuum (with a base pressure of 1×10^{-5} mbar or better) and at high temperature, resulting in stress relieved components. In fact, during the build the entire powder bed is heated at an optimal ambient temperature, specific for the material used. As a result, the parts produced with the EBM process are almost free from residual stresses and have a microstructure free from martensitic structures.

Binder based 3D printing

The Binder based 3D printing process is an indirect process in two steps. After applying a powder layer on the build platform, the powder is agglomerated thanks to a binder fed through the printer nozzle. Like in the beam based techniques, the operation is repeated by gradually lowering the platform and adding new layers of powder until parts are produced, which shall be then removed carefully from the powder bed, as they are in a 'green' stage. The metal part solidification takes place in a second step, during a debinding and sintering operation, sometimes followed by an infiltration step.

Fig. 20 Lightweight stainless screws made by binder based 3D printing (courtesy Höganäs AB - Digital Metal®)

The Binder based 3D printing technology is more productive than laser beam melting and requires no support structure. Besides it provides a good surface quality by using one of several post processing techniques:

- Peening/Blasting/Tumbling for average of R_a 3.0 µm
- Superfinishing for an average of R_a 1.0 µm down to < 1.0 µm

But the range of available materials is limited, and mechanical properties achieved can be lower than with laser and electron beam melting.

A variant not based on the same approach is the so called Fused Filament Fabrication (FFF): here, a thermoplastic feedstock containing a relatively high amount of metal powders is made into a thin wire, that is then fed into an extruder, that melts the binder and, being controlled in 3D, deposits the molten feedstock layer by layer to build the part gradually. In this case, the powder bed is missing; after printing, the part needs again to be subjected to debinding and sintering, to obtain a sintered part with a rather high shrinkage as in MIM sintering (even with higher shrinkage because the feedstock wires usually contain a lower amount of metal powders compared to common MIM feedstocks.

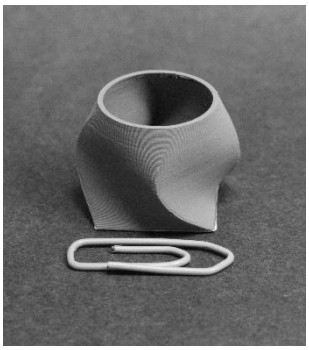

Fig. 21 316L stainless steel demonstrator part made by FFF (Courtesy Fraunhofer IFAM)

Direct Energy Deposition

With the direct energy deposition process, a nozzle mounted on a multi axis arm deposits melted material onto the specified surface, where it solidifies. This technology offers a higher productivity than selective laser melting and the ability to produce

larger parts, but the freedom in design is much more limited: for instance, lattice structures and internal channels are not possible.

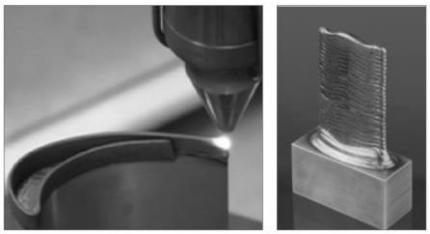

Fig. 22 Direct Energy Deposition process for blade repair or building (courtesy Fraunhofer ILT)

Benefits of Direct Energy Deposition process can be summarized as follows:

- New topological features possible
- Repair of parts that up to now were impossible
- Addition of functionalities on existing parts with either the same or a different material
- No dimensional limits (apart from the machine size)
- Excellent metallurgic quality at least as good as foundry
- Control of the material deposited (gradients, multi-materials, monolithic ...)

Further treatments and variants

Post processes are important in additive manufacturing such as removal of powder, support structures and platform, heat treatment and surface finishing, polishing, etc., and they can represent a significant part of the actual process. One of the most important post processes in Additive Manufacturing is HIPing. The density of parts produced by metal powder based additive manufactured is usually very high, but there is always the risk of defects in the material such as micro porosity or cracks, depending on the machine used as well as the type of powder. AM parts can contain a small amount of porosity for instance due to:

- Scanning calibration mismatch
- Key-hole beam-weld interaction
- Entrapped gas (can be internal to individual powder particles)
- Shrinkage as previous layers solidify
- Micro-cracks.

Eliminating the microporosity that forms during building can significantly improve fatigue life, impact toughness, creep strength and ductility. Besides, HIP provides stress relief to remove as-built residual stresses and reduces the extent of as-built segregation due to recrystallisation and homogenization of the microstructure.

Materials and typical applications

A very wide range of alloys are used on additive manufacturing machines thanks to the availability of suitable metal powders:

- Steels: stainless like 316L, 17-4PH etc., and also low alloy steels
- Nickel and cobalt base superalloys: 625, 718, CoCr F75 etc.
- Titanium alloys: Ti6Al4V, CPTi etc.
- Aluminium alloys: AlSi10Mg etc.

Many other metals are also evaluated and developing:

- Copper alloys
- Magnesium alloys
- Precious metals such as gold, silver, platinum
- Refractory metals such as Mo alloys, W and WC
- Metal Matrix Composites, etc.

Regarding the applications, additive manufacturing technology is strongly developing in many different industries such as:

- Aerospace
- Energy
- Medical, in particular in surgical implants and dental applications
- Tooling, in particular for plastics processing (and even MIM)
- Automotive and transportation
- Consumer goods

Fig. 23 shows the TRLs (Technology Readiness Levels) of AM in various industries. First four levels represent the evolvement of an idea until the lab-work, 5 to 7 until the prototype demonstration and 10 being system proven in operational environment.

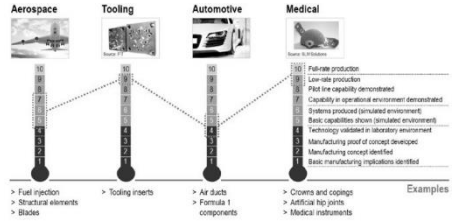

Fig. 23 Manufacturing readiness level of AM in various industry sectors (courtesy Roland Berger)

EXAMPLES OF PM PARTS FOR AEROSPACE APPLICATIONS

As already anticipated, aerospace is an industrial sector where powder metallurgy continuously finds new applications [20]. On one hand the technologies have evolved into high density-capable processes (and even P&S is improving the maximum density and consequently properties, although still distant from the full density performances that are usually needed), on the other hand the materials portfolio is now so wide that the designer can safely find good candidates, and reliable suppliers, even for very demanding applications.

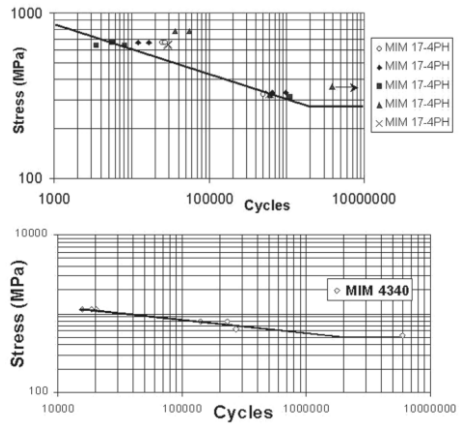

Fig. 24 Top: axial fatigue test plot for MIM-17-4 PH (R = 0); bottom: axial fatigue plot for MIM-4340 (courtesy LNEG)

High density implies lower and smaller porosities, and rounder pores: this is very helpful in reducing stress concentration around these defects and boosting the fatigue properties of the PM materials to reach, and sometimes go beyond the conventional materials. In fact, the use of fine powders, the isotropy of the composition, and the fine tuning of the microstructures achievable by microalloying sometimes allows the PM parts to outperform the wrought and machined counterpart. This is unfortunately still not the case of P&S materials, unless they are treated to full density (powder forging, HIPping), because of the limits in composition and the irregular pores normally left by the "incomplete" sintering experienced, but it is the case of many MIM (Fig. 24) and AM (Fig. 25) parts, especially after post-HIPping treatments.

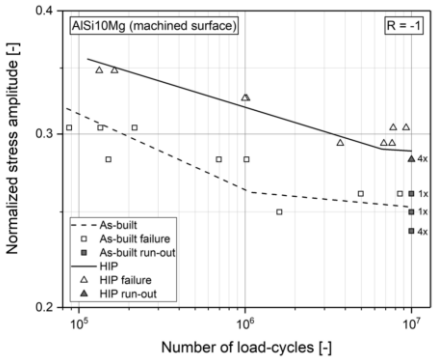

Fig. 25 The effect of HIP post processing on fatigue resistance of parts made by SLM (Laser Beam-AM) in AlSi10Mg [20]

PM, and especially AM but not only, is also increasingly used to produce special materials that can have application in aerospace. These are commonly referred to as "Functional Materials" as they are normally not use merely for their mechanical properties, but for their physical properties, like electrical, magnetic, thermal, etc. An outstanding example also in terms of market size is the already mentioned sector of the hard magnets; high temperature alloys are also to be included in this functional materials category, and biomaterials of different kinds. A very interesting family of functional materials is being developed for hydrogen storage in the solid state, using the characteristics of some metal hydrides [22]. With hydrogen becoming more and more a viable solution for mobility, including flying vehicles, PM materials might play a role in the future, even if the weight issue when considering aircraft applications is much more severe that for sea, rail or road transportation. Also in battery production powder metallurgy can be used to prepare e.g. sintered sheets of the battery materials, so PM is likely to play a major role in the electrification process.
In the following paragraphs some specific examples of PM parts (MIM, HIP and above all AM components) applied in aerospace are shown.

MIM part: high pressure compressor vane

This MIM application by the German producer Schunk Sintermetalltechnik GmbH is the first serial fabrication of a high pressure compressor (HPC) of a turbine engine. The part, a vane, substitutes a forged part without any reductions in performance, fulfilling all requirements of aerospace industry in quality assurance, reproducibility and traceability. The most important challenge was the guarantee the shape stability of the aerofoil and the prevention of contamination of the material with carbon, oxygen and nitrogen along the process, from powder production up to the sintered part. Additionally, the part had to go through a process of several gates and engine tests before being released for use in aerospace industry.

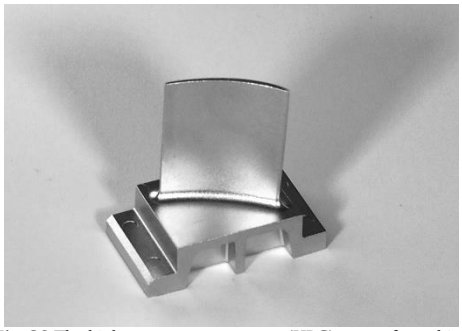

Fig. 26 The high pressure compressor (HPC) vane of a turbine engine (courtesy Schunk Sintermetalltechnik GmbH)

HIP part: Impeller for the cryogenic engine of Ariane V space rocket

Fig. 27 shows an example of HIP part. It is an impeller used in the Ariane 5 Rocket, produced by Aubert&Duval for Safran SA. The material is a Ti6Al4V alloy; the size of the part (larger diameter) is 100 mm. By using this powder metallurgy route, the customer obtained more freedom in vane design, as the shapes were impossible to machine. With a high dimensional reproducibility, the surfaces were in fact produced net shape. The material showed useful mechanical properties at the typical use temperature of only 20 K (-253.16°C).

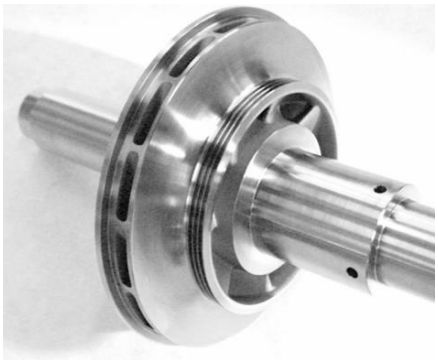

Fig. 27 The Ti64 impeller for the cryogenic engine of Ariane V space rocket (courtesy Aubert&Duval and Safran)

HIP part: Near net shape hipped Astroloy casing for high speed turbine

Current high speed turbine casing constitutive materials are designed to work at ca. 650°C, so that superalloys like Inconel 718 or Waspaloy are typically used. All aeronautic propulsion producers are trying to find materials and manufacturing routes capable to provide casings which can operate at higher temperatures, 700 to 800°C, a range of temperature that pushes conventional materials to the limit, to improve performances and efficiency, at the same time reducing emissions. Aubert&Duval used HIP to produce this part (Fig. 28) out of Ni-based alloy Astroloy, obtaining properties that exceed those of the competing forged Waspaloy AMS5704.

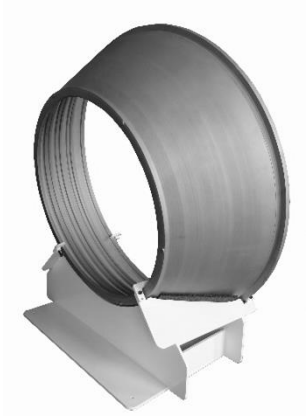

Fig. 28 The Astroloy casing for high speed turbine (courtesy Aubert&Duval)

These are some of the properties of the material produced by HIP:

- Density (g/cm^3): 7.92
- Tensile Strength (MPa): > 1300 MPa
- Yield Strength (MPa): >900 MPa
- Hardness: 340 HB10; 410 HV0.5
- Elongation (%): >25 from room temperature up to 760°C

AM part: Titanium insert for satellite sandwich structures

As weight reduction in space applications has an enormous driving force due to the cost of sending material to orbit (each kilogram put into orbit costs around $20,000), AM can help by providing lighter structures that could not be easily produced otherwise. Materialise & Atos used an optimized design to develop the new inserts (Fig. 29), produced by Laser Powder Bed Fusion out of Ti6Al4V. They are weighing just one-third of the initial weight of 1454g, that is 500g, with some improved properties added in. The obvious benefits compared to carbon fiber structures are:

- Weight reduction by using topology optimization and lattice design
- Reduction of thermo-elastic stress issues during the curing process of carbon fiber reinforced polymers
- Increased lifetime

Fig. 29 The titanium inserts for satellite sandwich structures (courtesy Atos and Materialise)

AM part: Support for a satellite antenna

By making use of the topology optimization feature in the AM process, this support for a satellite antenna (Fig. 30) has been produced at Poly Shape by Laser Powder Bed Fusion with a weight reduction of 55% from the original design. The material is Ti6Al4V, the part is about 300 mm high and weighs 3.3 kg now.

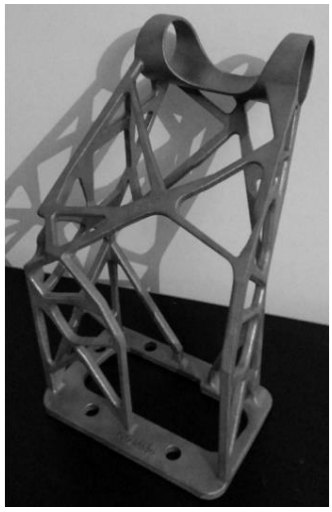

Fig. 30 The support for a satellite antenna (courtesy Poly Shape)

AM part: Bionic partition

Another example of the topology optimization feature in the AM process is this new Scalmalloy (AlMgSc) bionic partition for an A320 Airbus plane (Fig. 31). The use of topology optimization led to a huge weight saving, paving the way to new generations of aircraft cabin components that are more valuable, lighter, and thus create less impact on the environment. The material properties are:

- Density (g/cm^3): ~2.7
- Tensile Strength (MPa): 490
- Yield Strength (MPa): 450
- Hardness: 177 HV0.3
- Elongation (%): 8

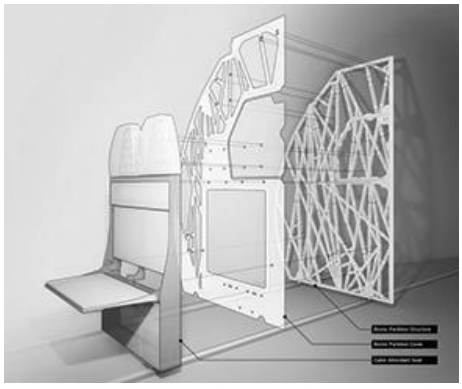

Fig. 31 The bionic partition (first object from the right) for an Airbus A320 (courtesy Airbus)

AM part: Borescope bosses for A320Neo geared Turbofan™ engine

The bosses (Fig. 32) are made by selective laser melting (SLM) on an EOS machine with Inconel 718 powders. They form part of MTU's low-pressure turbine case and allow the blading to be inspected at specified intervals for wear and damage using a borescope. The part volume is 15.600 mm³, and sizes are 42 x 72 x 36 mm.
Benefits of the AM technologies demonstrated here are the possibility of a series production of up to 2,000 parts per year, lower development production lead times and lower production costs, suitability for producing parts in materials that are difficult to machine, as, for example, nickel alloys, and for complex components that are extremely difficult, if not impossible to manufacture using conventional methods, and tool-free manufacturing and less material consumption.

Fig. 32 The boss for a borescope for the A320Neo geared Turbofan™ engine (courtesy MTU Aero Engines)

AM part: Bracket

The AM technology allowed Airbus and MBFZ Toolcraft GmbH to redesign a 30% lighter bracket for a cabin door (Fig. 33). Produced out of Ti6Al4V with Laser Powder Bed Fusion, the part has dimensions of 225 x 225 x 120 mm.

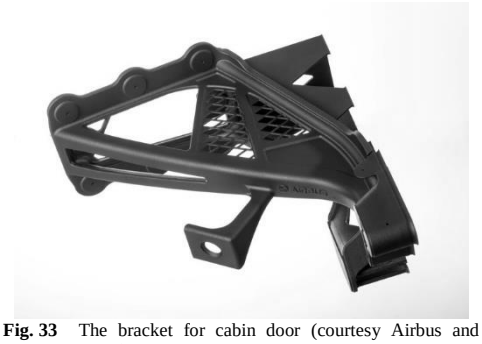

Fig. 33 The bracket for cabin door (courtesy Airbus and MBFZ Toolcraft GmbH)

AM Rocket parts

In recent years, space agencies have been investigating with increasing interest te use of AM for the fabrication of critical parts for space vehicles. For example, there have been wide reports of the activities to develop special nozzles for rocket engines. Stimulated from work done by GE Aviation for their GE9X engine [160], AM gave the chance to NASA to develop a new series of rocket engine components [24], including a bimetal (Cu/Inconel) rocket igniter [25], using a wide range of AM techniques, most of which based on powder metallurgy. ESA is working on similar programmes, for instance for the Ariane launcher.
In Germany, an interesting example is the demonstrator rocket engine developed by Fraunhofer IWS and TU Dresden, all made by Laser Powder Bed Fusion or L-PBF [26]. The engine is thought for microlaunchers that carry smaller payloads (about 350 kg) and uses incoming fuel to cool the nozzle structure by conformal cooling channels that are built by the AM technique. The design allows for a reduction of fuel consumption of about 30%.

Fig. 34 Aerospike nozzle for microlaunchers (courtesy Fraunhofer IWS and TU Dresden)

CONCLUSION

Powder Metallurgy is a set of technologies, continuously evolving but with a wide and established core, allowing the fabrication of solid, reliable and performant metal parts that can be used in several sectors, including aerospace.
Although decades ago the only widespread technology was Press&Sinter, with some limitations in terms of available compositions and properties, mainly because of the reduced ability to achieve low residual porosity, nowadays PM offers a variety of fabrication routes that deliver high quality, high density, high complexity parts, with specific compositions that can also be tuned to customer needs because of the ease of alloying given by the powdered raw materials.
In aerospace, the examples shown indicate a large amount of applications have already been demonstrated, and that great potential for further development can be envisaged especially in the emerging net and near net shape technologies, like AM and

MIM. Topology optimization in AM can drive further weight reduction, and improve sustainability in aerospace, at no expense of performance. This justifies the increasing interest of aircraft producers and space agencies in this field.

Acknowledgments
Authors are grateful for the support of the Sectoral Groups EuroPress&Sinter, EuroMIM, EuroHIP, EuroAM in the European Powder Metallurgy Association, whose members have given most of the information reported in this paper.

REFERENCES

1. W. Schatt, K-P Wieters: *Powder Metallurgy - Processing and Materials*, EPMA, Shrewsbury, UK, 1997.
2. R. M. German: *Powder Metallurgy & Particulate Materials Processing*, MPIF, Princeton, NJ, 1992.
3. R. M. German: *Particle Packing Characteristics*, MPIF, Princeton, NJ, 2011.
4. A. Lawley: *Atomization: The Production of Metal Powders*, MPIF, Princeton, NJ, 1992.
5. VV. AA.: *Introduction to Press & Sinter Technology*, 1st Edition, EPMA, Shrewsbury, UK, 2018.
6. L.F. Pease, W.G. West: *Fundamentals of Powder Metallurgy*, MPIF, Princeton, NJ, 2002.
7. VV. AA.: *Powder Metallurgy Design Manual*, MPIF, Princeton, NJ, 1998.
8. H. Kuhn, B. L. Ferguson: *Powder Forging*, MPIF, Princeton, NJ, 1990.
9. M. Nishihara, M. Koizumi, M. (eds): *Isostatic Pressing: Technology and Applications*, Springer, Netherlands, 1991.
10. K. J. A. Brookes, *Hardmetals and other hard materials*, 3rd edition, International Carbide Data, Hertfordshire, UK, 1998.
11. J. Konstanty, *Cobalt as a matrix in diamond impregnated tools for stone sawing applications*, 2nd edition, AGH, Krakow, 2003.
12. C. Lall, *Soft Magnetism, Fundamentals for Powder Metallurgy and Metal Injection Molding*, MPIF, Princeton, NJ, 1992.
13. R. M. German, A. Bose: *Injection Moulding of Metals & Ceramics*, MPIF, Princeton, NJ, 1997.
14. R. M. German: *Metal Injection Molding A Comprehensive MIM Design Guide*, MPIF, Princeton, NJ, 2011.
15. R. M. German: *Sintering Theory and Practice*, New York, NY, 1996.
16. VV. AA.: *Introduction to Metal Injection Moulding*, 4th Edition, EPMA, Shrewsbury, UK, 2018.
17. H. V. Atkinson, S. Davies: *Fundamental aspects of hot isostatic pressing: An overview*, Metallurgical and Materials Transactions A, volume 31, 2000, 2981–3000. https://doi.org/10.1007/s11661-000-0078-2.
18. VV. AA.: *Introduction to Hot Isostatic Pressing Technology*, 2nd Edition, EPMA, Shrewsbury, UK, 2018.
19. VV. AA.: *Introduction to Additive Manufacturing Technology*, 3rd Edition, EPMA, Shrewsbury, UK, 2019.
20. VV. AA.: *Spotlight on PM Case Studies: Aerospace*, 1st edition, EPMA, Shrewsbury, UK, 2019.
21. W. Schneller et al., Effect of HIP Treatment on Microstructure and Fatigue Strength of Selectively Laser Melted AlSi10Mg, J. Manuf. Mater. Process. 2019, 3(1), 16. https://doi.org/10.3390/jmmp3010016.
22. J. B. von Colbe et al.: International Journal of Hydrogen Energy, 44(15), 2019, 7780-7808. https://doi.org/10.1016/j.ijhydene.2019.01.104
23. [13.8.2020], https://3dprint.com/131192/ge-aviation-big-jet-engine/
24. [13.8.2020], https://3dprint.com/160079/nasa-3d-printed-engine-tests/
25. [13.8.2020], https://3dprint.com/188281/nasa-3d-printed-rocket-igniter/
26. [13.8.2020], https://tu-dresden.de/ing/maschinenwesen/die-fakultaet/news/3D-Raketentriebwerk?set_language=en

ACTA METALLURGICA SLOVACA
2020, VOL. 26, NO. 4, 161-165

RESEARCH PAPER

SIMULTANEOUSLY ENHANCING MECHANICAL PROPERTIES AND ELECTRICAL CONDUCTIVITY OF Cu-0.5%Cr ALLOY PROCESSED BY ECAP AND DCT

Zhu Qi Chu [1,2,3†], Kun Xia Wei [1,2†], Li Chen Yang [1,2], Wei Wei [1,2], Qing Bo Du [1,2], Igor V. Alexandrov [2,4]*, Jing Hu [1,2]*

[1] School of Materials Science and Engineering, Changzhou University, 1 Gehu Road, Changzhou 213164, P. R. China

[2] Jiangsu Key Laboratory of Materials Surface Science and Technology, Sino-Russia Joint Laboratory of Functional Nanostructured Materials, Changzhou University, Changzhou 213164, P. R. China

[3] School of Electronic Engineering and Intelligent Manufacturing, Anqing Normal University, 1314 Jixian North Road, Anqing 246011, P. R. China

[4] Department of Physics, Ufa State Aviation Technical University, 12 K. Marx St., 450008 Ufa, Russia

*Corresponding author: benjamin.wwei@163.com (W. Wei), Tel.:+86 519 8633 0095, School of Materials Science and Engineering, Changzhou University, Changzhou 213164, P. R. China; Igor V. Alexandrov@yandex.ru (I. V. Alexandrov), Tel.:+ 7-927-930-38-44, Department of Physics, Ufa State Aviation Technical University, 12 K. Marx St., 450008 Ufa, Russia
† These authors contributed equally to this work.

Received: 19.08.2020
Accepted: 20.09.2020

ABSTRACT

Mechanical properties and electrical conductivity of Cu-0.5%Cr alloy were simultaneously enhanced by combing the equal channel angular pressing (ECAP) and deep cryogenic treatment (DCT). The effect of DCT on the microstructure and properties of Cu-0.5%Cr alloy prepared by ECAP was investigated. The results show that the grains were elongated and refined along the deformation shear direction, and the dislocation density increased significantly by ECAP deformation. After the subsequent DCT, the grains were further refined, and at the same time, the dislocation density was further increased. With the increase of passes of ECAP, the microhardness and tensile strength of Cu-0.5%Cr alloy increased significantly, but the elongation to failure and electrical conductivity decreased slightly. After the DCT, the microhardness, electrical conductivity, tensile strength and elongation to failure of the Cu-0.5%Cr alloy were improved. After the ECAP (four passes) and DCT (12 h), the tensile strength, elongation to failure and electrical conductivity reached 483 MPa, 17.6% and 29%IACS respectively. The improvement of tensile properties could be attributed to the increase of dislocation density and grain refinement. The electrical conductivity was improved by the DCT due to the decrease of vacancy concentration.

Keywords: Cu-0.5%Cr alloy; ECAP; DCT; Microstructure; Mechanical properties; Electrical conductivity

INTRODUCTION

With the rapid development of electronics industry, it is essential to fulfil the growing performance demands of Cu-Cr alloys. More attentions have been paid to equal channel angular pressing (ECAP) in order to improve the microhardness and tensile strength of Cu-Cr alloys [1-3]. Grains were significantly refined after the ECAP, the dislocation density was also increased, thus resulting in the increase of microhardness and tensile strength of Cu-Cr alloys [4]. However, the electrical conductivity and elongation to failure were degraded. The microhardness and electrical conductivity of the alloys could be improved by the following aging treatment [5-6].

Deep cryogenic treatment (DCT) is known as an extension of traditional heat treatment process. The process of cooling materials at cryogenic temperature using the liquid nitrogen is utilized to enhance the mechanical and physical properties of materials [7-11]. After the DCT, The retained austenite of die steel was transformed into the martensite with the ultrafine carbide precipitation and residual stress elimination [12-13]. DCT could accelerate the dispersion and precipitation of the second phase particles in the aluminum alloy [14]. For copper alloys, the activation energy of the phase transition could be increased, and the duration of the phase transition can be shortened, thereby fine grains were formed [15-16]. The electrical conductivity of Cu-Be and Cu-Cr-Zr alloys increased significantly with the decrease of solute atomic concentration in the matrix by DCT [15, 17].

In the present, the effect of DCT on microstructure and properties of the ECAPed Cu-0.5%Cr alloy was investigated to simultaneously enhance mechanical properties and electrical conductivity of Cu-0.5%Cr alloy.

MATERIAL AND METHODS

Cu-0.5%Cr alloy were supplied by CHINALCO Luoyang Copper Co. Ltd. The samples with a size of 12×12×80 mm^3 were solid-solution treated at 1273 K for 0.5 hour in the NBD-

1200 tube furnace. The ECAP was performed at room temperature using a die with a channel angle 110°. The sample were pressed for totals of 4 passes and without rotation between each pass in the processing route designated A. The equivalent strain for each pass is 0.8 [18].

After the ECAP processing, the samples were treated with different time of cryogenic treatment. After precooling for 5 minutes, the timer is started, and the sample is taken out after the time is up. The time was 3h, 6h, 12h, 18h, 24h, 36h and 48h, respectively.

Microstructures of the material were examined on optical microscope and JEOL JEM2100 high-resolution transmission electron microscope (TEM). The samples for TEM were thinned by the Tenupol-5 twin-jet electro-polishing device in a solution of 33% nitric acid and 67% methanol at -25 ℃ with a current of 5-15V. X-ray diffraction (XRD) measurements were performed on a D/max-2500 pc X-ray with a Cu target operating at 40 kV/100 mA. A series of θ-2θ scans were performed to record the XRD patterns ranged from 30° to 120°. Microhardness was conducted on the samples with a load of 200 g for 15 s. Tensile tests were performed using a Shimadzu AGS-10kND machine with a cross-head speed of 1mm min^{-1}. The electrical conductivity was measured with a 7501-A eddy current conductor with an accuracy ± 2%.

RESULTS AND DISCUSSION

3.1. Microstructure characterization

3.1.1. Optical observations

The optical microstructures of Cu-0.5%Cr alloy are revealed after the DCT as shown in Figure 1. It can be observed that the grains are relatively large, and the grain boundaries are clear after solid solution treatment, meanwhile, twins are formed. The average grain size is about 70 μm in Fig.1 (a). After DCT for 12 hours, the grains are obviously refined, and the distribution is relatively more uniform, as shown in Fig.1 (b).

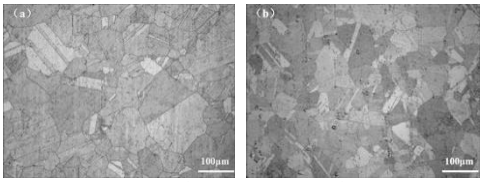

Fig. 1 Optical images of Cu-0.5%Cr alloy after DCT: (a) solid solution, (b) t =12h

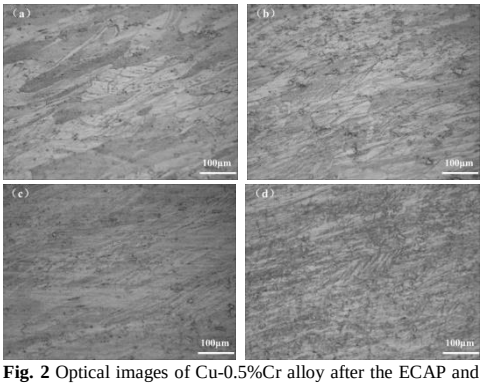

Fig. 2 Optical images of Cu-0.5%Cr alloy after the ECAP and DCT: (a) 1P, (b) 1P + DCT (12h), (c) 2P, (d) 2P + DCT (12h)

After one ECAP pass, the coarse grains of the solid solution state are elongated and refined along the direction of deformation and shear, and the grain boundaries are relatively clear (shown in Fig.2 (a)). With the increase of ECAP passes, the grains are significantly refined along the shear direction in Fig.2 (c). After the subsequent DCT for 12h, it can be seen that the grains are further refined by comparing Fig.2 (b) and Fig.2 (d).

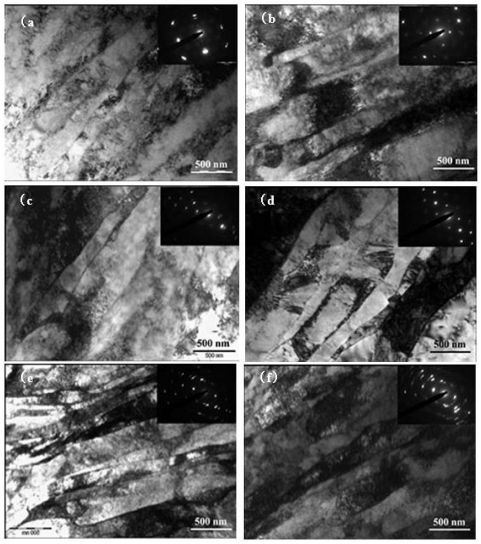

Fig. 3 TEM micrographs of Cu-0.5%Cr alloy after ECAP and DCT for 12h: (a) 1P, (b) 1P + DCT, (c) 2P, (d) 2P + DCT, (e) 4P, (f) 4P + DCT

3.1.2. TEM microstructure

From TEM micrographs, it can be observed that the disordered dislocations spread along the elongated boundaries and low-angle grain boundaries were formatted by one pass of ECAP, which can be speculated from the scattered spots in the selected area electron diffraction (SAD) pattern in Fig.3 (a). As the number of ECAP passes increases, grains are further refined, and dislocation density increases. The SAD in Fig.3 (e) with a continuous ring indicates the formation of large-angle grain boundaries.

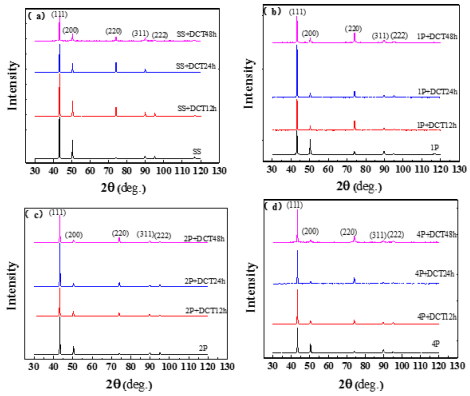

Fig. 4 X-ray diffraction pattern of Cu-0.5%Cr alloy after ECAP and DCT for different time

The dislocation density increases significantly along the grain boundaries and inside the grains by DCT treatment. After 4 passes of ECAP + DCT (12h), the banded grains with thickness of 200 ~ 300nm are obtained in Fig.3 (f). The almost continuous diffraction ring in the corresponding SAD pattern indicates that a nano-scale grain structure with a large-angle grain boundary is formed. Therefore, after DCT, the microstructure of Cu-0.5%Cr alloy is refined, while the dislocation density is significantly increased.

3.2 XRD

As shown in Figure 4. With the extension of the DCT time, the intensity of the diffraction peaks of {111}, {220} and {311} increased significantly in Fig.4 (a), while the intensity of the diffraction peaks of the {200} plane shows a downward trend. The results show that DCT causes slight changes in lattice constant. The intensity of the diffraction peak changes significantly through ECAP deformation and DCT treatment in Fig.4 (b-d). This is because the deformation process causes the microstructure to deform and thus results in the occurrence of a new preferred orientation.

Table 1 The average crystallite size and dislocation density of Cu-0.5%Cr alloy after ECAP and DCT

Samples		$<\varepsilon^2>^{1/2}$/%	d/μm	ρ/ 10^{-15} m^{-2}
ECAP	0P	0.080	65	0.1
	1P	0.120	0.418	1.62
	2P	0.140	0.288	2.55
	4P	0.150	0.224	2.83
ECAP+ DCT(12h)	0P+DCT	0.089	51	1.15
	1P+DCT	0.268	0.338	1.89
	2P+DCT	0.321	0.289	2.46
	4P+DCT	0.352	0.242	2.77
ECAP+ DCT(48h)	0P+DCT	0.092	47	1.26
	1P+DCT	0.273	0.326	1.95
	2P+DCT	0.327	0.279	2.54
	4P+DCT	0.358	0.237	2.81

Table 2 The lattice constants（Å）of Cu-0.5%Cr alloy after ECAP and DCT

Samples	0P	1P	2P	4P
DCT （0h）	3.62284	3.62316	3.62018	3.62046
DCT（12h）	3.61860	3.62054	3.62014	3.62016
DCT（24h）	3.62288	3.62104	3.62000	3.62053
DCT（48h）	3.62310	3.62300	3.62148	3.62170

The dislocation density was calculated by $\rho = \frac{2\sqrt{3}\langle\varepsilon^2\rangle^{1/2}}{d \cdot b}$ [19-20], where b is the Burgers vector and equal to $\sqrt{2}a/2$ for Cu (0.256 nm), which was listed in Table 1. It can be found that the grain size decreases and the dislocation density increases after the DCT treatment. During the rapid cooling process, Cu-0.5% Cr alloy generates a large amount of residual stress due to volume shrinkage, resulting in increased dislocations [16]. The lattice constants（Å）of Cu-0.5%Cr alloy after the ECAP and DCT are calculated by XRD analysis (Table 2).

It can be observed that the grain size decreases significantly after DCT (12h) treatment. As the number of ECAP passes increases, the effect of DCT treatment on grain refinement also gradually weakens, which is consistent with the results of the previous microstructure. DCT can increase the activation energy of phase transformation and shorten the phase transformation duration, thus fine grains are introduced to copper alloys [15, 16]. There are a large number of black flocculent distributions in the grain boundary and in the crystal by TEM, which is consistent with the results of XRD calculations, the dislocation density increases through DCT treatment. For pure copper, the DCT can increase the dislocation density, resulting in the formation of fine grains [21].

3.3. Mirohardness and electrical conductivity

With the increase of the ECAP passes, the microhardness value increases obviously in Fig.5 (a). After one pass of ECAP, the microhardness reaches 144HV. As the number of deformation passes increases, the upward trend of microhardness gradually decreases, and basically reaches saturation in four ECAP pass. This is due to the fact that the grain size does not change obviously, and the phase equilibrium of dislocation accumulation and annihilation [22-24].

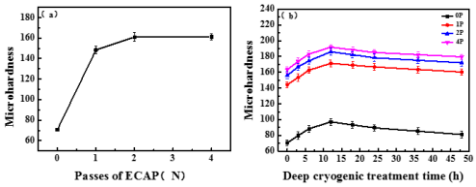

Fig. 5 Microhardness of Cu-0.5%Cr alloy processed by the different passes of ECAP and DCT for different time

Fig.5 (b) shows the microhardness of Cu-0.5%Cr alloy processed by the different passes of ECAP and DCT for different time. The microhardness increases first and then decreases with the increase of the DCT time. After four ECAP passes and 12 hours of DCT, the microhardness reaches the maximum value of 192HV. The DCT treatment is carried out in an environment of liquid nitrogen at -196℃, and the lattice shrinks at an ultra-low temperature [25, 26]. Due to the different shrinkage of each crystal plane, micro-deformation occurred, which causes the increase of dislocations and the formation of sub-crystalline structure, and at the same time produces a certain work hardening. From the microstructure and XRD analysis, it can be seen that the grains are refined after DCT treatment, Cr particles are precipitated in the matrix, and the dislocation density increases. With the extension of cryogenic time, the degree of grain refinement and dislocation density will not be further increased. When the material is taken out from the liquid nitrogen, the temperature environment will be changed significantly, and the recovery occurs at lower temperature environment [27], which may be an explanation of the decrease in microhardness.

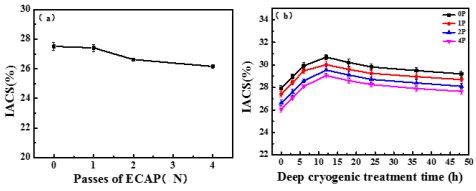

Fig. 6 The curves of the electrical conductivity of Cu-0.5%Cr alloy by the different passes of ECAP and DCT time

Fig.6 (a) is the curve of the electrical conductivity change of ECAP deformed Cu-0.5%Cr alloy. The results show that as the ECAP passes increase, the electrical conductivity decreases slightly. Compared with the solution treatment, the electrical conductivity decreases only about 6.1% after four ECAP deformations passes. From Table 1, it can be seen that after ECAP, crystal defects such as dislocations of Cu-0.5%Cr alloy increase, the electron scattering effect increases, and the electrical conductivity decreases slightly. Similar changes in

the electrical conductivity of Cu-0.5%Cr alloy with large strains were confirmed [28, 29].
After the subsequent DCT **(**12h**)**, the change curve of electrical conductivity is shown in Fig.6 (b). It is observed that with the extension of the DCT time, the electrical conductivity tends to increase first and then decrease. After DCT for 12h, the maximum solution solid Cu-0.5%Cr alloy is 30.7% IACS. After four ECAP passes and the DCT for 12 hours, it is improved by about 10.7% compared with no DCT. In other words, the electrical conductivity after DCT is higher than that of the ECAP before the DCT for 12h, which is similar to the change in electrical conductivity of pure copper DCT treatment [21].

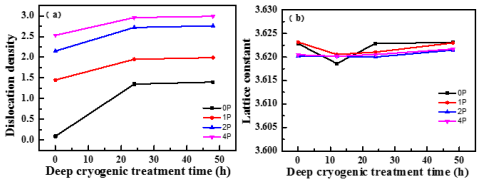

Fig. 7 The curves of the dislocation density and lattice constant of Cu-0.5%Cr alloy by the different passes of ECAP and DCT time

The lattice distortion leads to the increase of subgrain boundaries and grain boundaries, and increases the scattering effect on electrons, resulting in a slight decrease in the electrical conductivity. The similar result was found that the electrical conductivity of Cu decreased after large plastic strains [29]. The electrical conductivity is affected by the vacancy concentration. Some studies have shown that the ECAP process enhances the concentration of vacancy and leads to the decrease of electrical conductivity [30-31]. After the DCT treatment, the volume and lattice shrinkage, the concentration of vacancy decreases, thus improving the electrical conductivity. For the solution treated Cu-0.5%Cr alloy, the lattice constant tends to decrease first and then increase with the increase of DCT treatment time, as shown in Fig.7 (b). Similarly, the lattice constant has the same trend after ECAP + DCT. The lattice distortion makes the electron scattering stronger and reduces the electrical conductivity. The increased electron scattering results in reduced electrical conductivity, which is caused by lattice distortion. The effect of vacancy concentration is greater than the lattice distortion, so before the DCT for 12h, the electrical conductivity shows an upward trend. The former influence factors are opposite, the electrical conductivity has decreased. Therefore, after DCT, the electrical conductivity of Cu-0.5%Cr alloy has a similar trend to that of pure copper [21].

3.3 Tensile properties

In Figure 8 the tensile strength of the solution treated Cu-0.5%Cr alloy is 262MPa. After four ECAP passes, the tensile strength is increased to 451 MPa. After four ECAP passes and the DCT for 12 hours, it arrives at 483 MPa. The increase in the tensile strength of the Cu-0.5%Cr alloy is attributed to grain refinement and increased dislocation density.
Fig.9 (a) shows the tensile strength and elongation to failure of Cu-0.5%Cr alloy processed by the ECAP and DCT for 12h. It can be seen that the tensile strength is significantly improved before two passes of ECAP, and then slightly improved. The elongation to failure decreases significantly after ECAP deformation, as the number of deformation passes further increases**,** it remains basically constant (~16%). After DCT treatment, the tensile strength and elongation at break of Cu-0.5% Cr alloy are improved. After four ECAP passes and the DCT for 12 hours, the tensile strength is 483 MPa, and the elongation to failure is 17.6%.The strength properties of 316l stainless steel rolled at low temperature are significantly improved compared with that rolled at room temperature [32]. Asymmetric rolling at cryogenic temperature provides greater strength tensile properties of pure aluminium than rolling at ambient temperature [33].

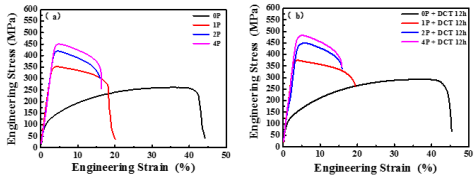

Fig. 8 Curves of tensile engineering stress-strain of Cu-0.5%Cr alloy subjected to ECAP and DCT for 12h: (a) ECAP (b) ECAP and DCT 12h

In general, the tensile strength can be improved by solution strengthening, precipitation, dispersion and work hardening. However, the electrical conductivity will also decrease, and vice versa. Fig. 9 (b) is the variations of the tensile strength and electrical conductivity of Cu-0.5%Cr alloy processed by ECAP and DCT. It can be seen that with the increase of ECAP passes, the tensile strength is inversely related to the electrical conductivity. However, after the DCT treatment, the tensile strength and electrical conductivity of Cu-0.5%Cr alloy is simultaneously improved. Shangina *et al.* [4] showed that the tensile strength of Cu-0.5%Cr after ECAP and aging treatment reached 462 MPa, and the electrical conductivity was 72% IACS. Although the electrical conductivity treated by ECAP and DCT failed to reach a high level (no more than 40% IACS), the combination of ECAP and DCT can balance the relationship between strength and electrical conductivity, which can be further tailored by the aging treatment in future.

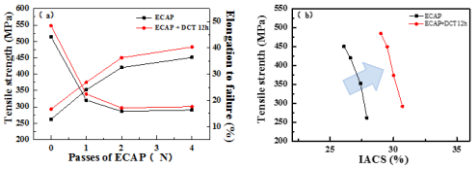

Fig. 9 Tensile strength, electrical conductivity and elongation to failure curves of Cu-0.5%Cr alloy treated with ECAP+DCT for 12 h

CONCLUSION

1) Uniform and fine equiaxed grains were observed in Cu-0.5%Cr alloy with the increase of ECAP passes and the grains were further refined, the dislocation density increased after the subsequent DCT. After 4 passes of ECAP + DCT (12h), the thickness of banded grains were refined to 200 ~ 300nm.
2) After the ECAP and DCT, microhardness and tensile properties were significantly improved due to the grain refinement and accumulated dislocations. The electrical conductivity was enhanced by DCT due to the decrease in lattice constant and the change in vacancy concentration.
3) After 4 passes of ECAP + DCT (12h), the microhardness, tensile strength, elongation to failure and electrical conductivity reached 192HV, 483MPa, 17.6% and 29%IACS, respectively. In comparison to the counterpart, the microhardness, tensile strength, elongation to failure and electrical conductivity are increased by 17.8%, 7%, 8% and 11%, respectively.

4) The process combing ECAP and DCT could simultaneously improve the tensile properties and electrical conductivity of Cu-0.5%Cr alloy.

Acknowledgments

Authors are grateful for the support of experimental works by the National Natural Science Foundation of China under Grant No. 51561001, the Priority Academic Program Development of Jiangsu Higher Education Institutions (PAPD), the Top-notch Academic Programs Project of Jiangsu Higher Education Institutions (TAPP), and the Science and Technology Project of Changzhou, P. R. China under grant No.CZ20180016 and CE20170028.

REFERENCES

1. X. Zhang, G. Chen, X. Chen: App. Mech. Mater., 455, 2014, 131-136. https://doi.org/10.4028/www.scientific.net/AMM.455.131.
2. W. Wei, K. X. Wei, G. J. Fan: Acta Mater., 56(17), 2008, 4771-4779. https://doi.org/10.1016/j.actamat.2008.05.025.
3. J. Bidulska, R. Bidulsky, M. A. Grande, T. Kvackaj: Materials, 12(22), 2019, 3724. https://doi.org/10.3390/ma12223724.
4. D. Shangina, et al.: Journal of Materials Science, 51(11), 2016, 5493-5501. https://doi.org/10.1007/s10853-016-9854-2.
5. S. V. Dobatkin, N. R. BocHvar, D. V. Shangina: Advanced Engineering Materials, 17(12), 2015, 1862-1868. https://doi.org/10.1002/adem.201500099.
6. W. Wei, K. X. Wei, Q. B. Du, F. F. Musin: Strength and electrical conductivity of bulk nanostructured Cu and Cu-Based alloys produced by SPD. In.: *Handbook of Mechanical Nanostructuring*, ed. by M. Aliofkhazraei, Wiley-VCH Verlag, 2015, p. 115-142. https://doi.org/10.1002/9783527674947.ch6.
7. S. Kalia: Journal of Low Temperature Physics, 158(5-6), 2010, 934-945. https://doi.org/10.1007/s10909-009-0058-x.
8. N. S. Kalsi, R. Sehgal, V. S. Sharma: Materials & Manufacturing Processes, 25(10), 2010, 1077-1100. https://doi.org/10.1080/10426911003720862.
9. W. Reitz, J. Pendray: Materials & Manufacturing Processes, 16(6), 2001, 829-840. https://doi.org/10.1081/AMP-100108702.
10. T. Kvackaj et al.: Acta Metall. Slovaca, 16(4), 2010, 268-276.
11. T. Kvackaj et al.: Acta Physica Polonica A, 131(4), 2017, 1105-1107. https://doi.org/10.12693/APhysPolA.131.1105.
12. B. Podgornik, I. Paulin, B. Zajec, S. Jacobsonc, V. Leskovšek: J. Mater. Process. Technol., 229, 2016, 398-406. https://doi.org/10.1016/j.jmatprotec.2015.09.045.
13. H. Li, W. Tong, J. Cui, H. Zhang, L. Chen, L. Zuo: Acta Metall. Sin. (Engl. Lett.), 27(3), 2014, 430-435. https://doi.org/10.1007/s40195-014-0075-x.
14. W. D. Zhang, P. K. Bai, J. Yang, H. Xu, J. Z. Dang, Z. M. Du: Transactions of Nonferrous Metals Society of China, 24(8), 2014, 2453-2458. https://doi.org/10.1016/S1003-6326(14)63370-7.
15. M. P. Ahmed, H. S. Jailani, S. R. Mohideen, A. Rajadurai: Metallography, Microstructure, and Analysis, 5(6), 2016, 528-535. https://doi.org/10.1007/s13632-016-0314-9.
16. Y. Wang et al.: Phase Transitions: A Multinational Journal, 85(7), 2012, 650-657. https://doi.org/10.1080/01411594.2012.659738.
17. Z. Wu, P. Shan, J. Lian, S. Hu: Materials and Design, 24(8), 2003, 687-692. https://doi.org/10.1016/S0261-3069(03)00029-3.
18. R. Z. Valiev, T. G. Langdon: Progress in Materials Science, 51(7), 2006, 881-981. https://doi.org/10.1016/j.pmatsci.2006.02.003.
19. Y. H. Zhao, X. Z. Liao , Z. Jin, R. Z. Valiev, Y. T. Zhu: Acta Materialia, 52, 2004, 4589-4599. https://doi.org/10.1016/j.actamat.2004.06.017.
20. K. Ushioda, S. Takebayashi, Y. R. Abe: Materials & Manufacturing Processes, 25(1-3), 2010, 185-194. https://doi.org/10.1080/10426910903202195.
21. K. X. Wei, Z. Q. Chu, W. Wei, Q. B. Du, I. V. Alexandrov, J. Hu: Advanced Engineering Materials, 21(7), 2019, 1801372. https://doi.org/10.1002/adem.201801372.
22. A. I. Almazrouee, K. J. Al-Fadhalah, S. N. Alhajeri, T. G. Langdon: Mater. Sci. Eng. A, 641, 2015, 21-28. https://doi.org/10.1016/j.msea.2015.06.016.
23. C. F. Zhu, et al.: Materials and Design, 52, 2013, 23-29. https://doi.org/10.1016/j.matdes.2013.05.029.
24. J. Li, X. J. Zhang, H. P. Wang, M. P. L: International Journal of Minerals Metallurgy & Materials, 20(1), 2013, 59-66. https://doi.org/10.1007/s12613-013-0693-8.
25. K. K. Wang, et al.: Mater. Sci. Eng. A, 743, 2019, 259-264. https://doi.org/10.1016/j.msea.2018.04.104
26. J. Liu, G. Li, D. Chen, Z. Chen: Chinese Journal of Aeronautics, 25(6), 2012, 931-936. https://doi.org/10.1016/S1000-9361(11)60464-0.
27. K. Han, P. R. Walsh, A. Ishmaku, V. Toplosky, L. Brandao, J. D. Embury: Philosophical Magazine, 84(34), 2004, 3705-3716. https://doi.org/10.1080/14786430412331293496.
28. N. Takata, S. H. Lee, N. Tsuji: Materials Letters, 63, 2009, 1757-1760. https://doi.org/10.1016/j.matlet.2009.05.021.
29. A. Habibi, M. Ketabchi, M. Eskandarzadeh: J. Mater. Process. Technol., 211, 2011, 1085-1090. https://doi.org/10.1016/j.jmatprotec.2011.01.009.
30. O. F. Higuera-Cobos, J. M. Cabrera: Mater. Sci. Eng. A, 571, 2013, 103-114. https://doi.org/10.1016/j.msea.2013.01.076.
31. M. J. Zehetbauer, G. Steiner, E. Schafler, A. Korznikov, E. Korznikova: Mater. Sci. Forum, 503-504, 2006, 57-64. https://doi.org/10.4028/www.scientific.net/MSF.503-504.57.
32. P. Petrousek, T. Kvackaj, R. Kocisko, J. Bidulska, R. Bidulsky: Acta Metall. Slovaca, 25(4), 2019, 283-290. https://doi.org/10.12776/ams.v25i4.1366.
33. D. Simcak, T. Kvackaj, R. Kocisko, R. Bidulsky, V. Puchy: Acta Metall. Slovaca, 23(2), 2017, 99-104. https://doi.org/ 10.12776/ams.v23i2.928.

ACTA METALLURGICA SLOVACA
2020, VOL. 26, NO. 4, 166-177

RESEARCH PAPER

INVESTIGATION OF DISTINCTIVE SOLUTIONIZING PROCESS PARAMETERS ON SIGNIFICANTLY INCREASING IN STRENGTH AND DUCTILITY OF As-CAST AZ80 Mg ALLOY

Mui Kheng Yeoh [1,2], XingHe Tan [1], Richard Wai Onn Kwok [3], Teik-Cheng Lim [2]*

[1]ST Engineering Land Systems Ltd, 249 Jalan Boon Lay, Singapore 619523

[2]School of Science and Technology, Singapore University of Social Sciences, 463 Clementi Road, Singapore 599494

[3]SMRT Corporation Ltd, 251 North Bridge Road, Singapore 179102

* Corresponding Authors: yeohmk@stengg.com, tel: +6568640721, School of Science and Technology, Singapore University of Social Sciences, 463 Clementi Road, Singapore 599494

Received: 24.10.2020
Accepted: 18.11.2020

ABSTRACT

A distinctive solutionizing process parameter was developed and performed to significantly enhance strength and ductility of aged AZ80 Mg alloy. The microstructure-processing-properties relationship was studied to help elucidate the mechanism. Microstructure and mechanical properties were studied by using optical microscopy, Field Emission Scanning Electron Microscopy, Transmission Electron Microscopy, X-ray diffraction, hardness and tensile testing. The results show that the solutionization at 380°C/10h followed by 420°C/10h promoted significant dissolution of eutectic $Mg_{17}Al_{12}$ and intermetallic phases. After standard aging at 200°C/10h, the formation of high-density precipitates $Mg_{17}Al_{12}$ with more spheroidization precipitates and lesser discontinuous precipitates morphology, which was not observed in conventional heat treatment for aged AZ80 Mg alloy. Fine precipitates $Mg_{17}Al_{12}$ resulted in a significant increase in ultimate tensile strength (50.3%), yield strength (35%), elongation (106%) and hardness (40%) compared to conventional heat treated cast AZ80 Mg alloy. These properties are comparable to the commonly used aerospace grade cast aluminium alloy A356.

Keywords: Cast AZ80 Mg alloy, Heat Treatment, Annealing Twins, Solutionizing, Strength, Ductility

1. INTRODUCTION

In today's market, demand for cast magnesium (Mg) alloys is considered one of the largest and fastest-growing due to their wide usage and application. In addition to the aerospace and automotive industries, demand for cast Mg alloys has been growing in the biomedical and military industries as well. The key factor for the increase in demand is their superior castability with a good combination of mechanical performance and lightness. Among the commercial cast Mg alloys, Mg-Al-Zn alloys have been widely used in many industrial sectors and defense industries owing to their attractive high specific strength to weight ratio and low cost. Nevertheless, cast AZ80 Mg alloy has relatively low strength and ductility and is restricted in its applications as compared with other cast alloys.

In order to increase uptake of cast AZ80 Mg alloy in the commercial markets, efforts have been directed towards development of materials through new processing techniques, alloying of elements and grain refinement. Recent research has shown increasing interest in enhancing the strength of cast AZ80 Mg alloy by the addition of nano-composites to create particulate reinforcements in a matrix of alloy [1-3]. Also, there has been greater focus on improving the mechanical properties of cast AZ80 Mg alloy with equal-channel angular pressing for grain refining prior to aging treatment [4, 5]. In addition, researchers have been trying to enhance the strengthening effect through micro-alloying elements such as Lithium [6], Yttrium [7], Neodymium [8], and Cerium [9] etc. Even though those processes can strengthen the properties of the material with good results, their production costs are comparatively higher and cycle time is longer. This has driven efforts to achieve strength enhancement through various heat treatment processes in order to expand its applications. In the past, many researchers focused their studies to develop and optimize heat treatment processes to achieve the desired mechanical properties of wrought AZ80 Mg alloy [10-13]. Only some investigations have been reported that relate to microstructure evolution and mechanical properties through heat treatment of as-cast AZ80 Mg alloy condition [14-17]. However, the strengthening effects reported in those studies are rather limited. In particular, Zhang et al. [15] studied heat treatment effects on the mechanical properties of cast AZ80 Mg alloy and achieved a tensile strength of 196-197 MPa and yield strength of 126-129 MPa, but ductility (3.66-4.42%) is still relatively low after aging. Besides, several researchers [14, 17] have suggested that it is possible to achieve good mechanical properties by controlling the microstructure, texture, dissolution of β-$Mg_{17}Al_{12}$ phase etc. through optimization of solution treatment. However, it is still difficult to achieve a good combination of strength and ductility, which may restrict their usage and application. More recently, several studies have been devoted to the development of better mechanical performance in as-cast AZ80 with different solutionizing times to enhance the dissolu-

tion of the eutectic $Mg_{17}Al_{12}$ phase [18, 19]. The findings suggest that the dissolution of β-$Mg_{17}Al_{12}$ phase is highly time and temperature dependent. The volume fraction of the β-$Mg_{17}Al_{12}$ phase decreased with time and temperature. These second-phase particles have been found to affect the mechanical properties of magnesium alloys [16, 18-20]. Although the results show significant differences in tensile properties, ductility is still a concern, which seem to be insufficient for high performance industrial applications. Therefore, significant efforts are still needed to develop a good combination of strength and ductility on as-cast AZ80 Mg alloy.

The dissolution of the β-$Mg_{17}Al_{12}$ phase has been reported to dissolve effectively into the matrix with the development of a two-step solution treatment method compared to a single step in some magnesium alloys [21-23]. This resulted in a better precipitation strengthening effect after subsequent aging. However, those suggested solution treating schedule may not be suitable for certain magnesium alloys although they are from the same alloy classes. By changing the heat treatment times and temperatures, the mechanical properties of different magnesium alloys can vary widely. Also, mechanical properties can be adversely affected by an increase in solution temperature or prolonging of solutionizing time. Hence, further modification of these heat treatments is required to develop for cast AZ80 Mg alloy in order to obtain the most desirable combination of properties.

To improve on what has been achieved by the research aforementioned, a distinctive solutionizing process parameter was developed and performed on as-cast AZ80 Mg alloy. The aim of this work is to investigate the effects of the solutionizing parameter and its age hardening response. Also, to elucidate the effects of dissolution of β-$Mg_{17}Al_{12}$ phase during solutionizing on enhancing the strength hardening effects leading to better mechanical properties of cast AZ80 Mg alloy. The relationship of precipitate morphology, mechanical properties and fracture failure mechanism of cast AZ80 Mg alloy is discussed.

2. MATERIAL AND METHODS

The commercial as-cast AZ80Mg alloy supplied ingot form was used in this study. The chemical composition of the as-cast AZ80 Mg alloy was determined by the inductively coupled plasma-AES method and its nominal composition by Mg-8.15Al-0.52Zn-0.20Mn (in wt.%). Prior to the solutionizing process, the as-cast AZ80 Mg specimens were homogenized at 300° C for 10 h at a heating rate of 1°C/min, followed by air cooled to reduce the segregation due to the casting solidification process and to obtain a better homogeneous microstructure. In order to investigate the effect of homogenization temperature on the microstructure, another homogenization at 380°C for 10 h (at heating rate of 1°C/min) with air cooling was studied to establish optimum homogenization conditions that would affect the subsequent solutionizing process.

The optimum homogenization conditions that have been established for the best microstructure will be selected and subjected to the subsequent solutionizing process. During the solutionizing process, a protective atmosphere with argon gas was used in the furnace for surface protection. In order to prevent fusion of eutectic compounds and voids formation [24], the specimens were loaded into the furnace at 260°C and heated to 420°C at a heating rate of 1°C/min, followed by holding at 420°C for 10 h and immediately quenched in water at room temperature (T4). Subsequently, aging treatment at 200°C for 10 h was applied on the solutionized specimens to study the effect of microstructure and mechanical properties in the as aged condition (T6). In this study, a distinctive solutionizing process (homogenization follow by solutionization) was denoted as T4X and denoted as T6X when inclusive of the ageing process. Figure 1 shows the schematic diagram of the entire heat treatment cycles that were carried out in this study.

To study the difference in microstructural morphology between as cast and heat treated AZ80 Mg alloy specimens, optical microscope (OM) and field emission scanning microscope (FESEM) equipped with energy dispersive spectrometer (EDS) were used to carry out microstructural characterization. For phase identification, X-ray diffraction using CuK_α radiation (k = 1.5406 A°) and a scan speed of 2°/min was conducted. Using Match! Software for XRD phase identification, the volume fraction V_f of the β-$Mg_{17}Al_{12}$ phase was measured. Metallographic specimens were prepared in accordance with ASTM E3-11, by first cross-sectioning, cold mounting, grinding and polishing. After obtaining a scratch free surface, specimens were etched with one of the following etchants to reveal their microstructures: acetic-glycol (20 mL acetic acid, 1 mL HNO_3, 60 mL ethylene glycol, 20 mL H_2O), acetic-picral (10 mL acetic acid, 4.2 g picric acid, 10 mL H_2O, 70 mL ethanol) and phosphor-picral (0.7 mL H_3PO_4, 5 g picric acid, 100 mL ethanol) [25]. Selection of etchants is dependent on the material condition of specimens. Quantitative analyses of the grain size and various phases were performed with Olympus Stream Image Analysis Software. The average grain size measurements were made using the linear intercept method in accordance with ASTM E112-13. TEM studies were also conducted using a combination of bright field (BF) and dark field (DF) TEM imaging, selected area electron diffraction (SAED). TEM was conducted on a JEM 2010F (JEOL) with an accelerated voltage of 200 kV. The TEM specimens were prepared by cross-sectioning them into thin slices of approximately 200µm thick and mechanically polished to thin foils of less than 30µm thick. Foils were then punched out with a disk punch to 3 mm diameter disks. They were subjected to ion milling thinning with a Gatan Precision Ion Polishing System (model 691) under operating conditions of 5.0 kV and an incident angle of 4-6° to a perforation thickness of less than 20µm. The perforations had been cleaned with ethanol after ion milling thinning.

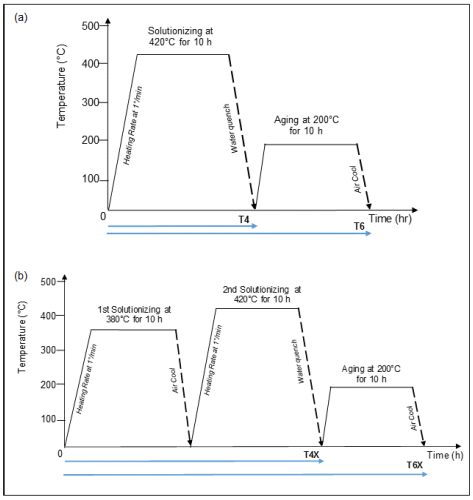

Fig. 1 Schematic diagram of the entire heat treatment cycles for (a) conventional heat treatment (T6); (b) current heat treatment (T6X) with two-step solutionizing and aging

Tensile tests were conducted at ambient temperature with a universal testing machine (Instron Model 8801) using a tensile speed of 0.5mm per minute in accordance with ASTM B557-15. After removal of the extensometer, speed was increased to 3mm per minute. A minimum of 3 specimens for each condition were

tested. SEM fractography was also performed on the fracture surface of the tensile test specimens. Vickers microhardness testing with 100g load applied and 15 seconds of holding time was performed on cross-sectioned and polished specimens in accordance with ASTM E384-17 using Matsuzawa microhardness tester MMT-X7. To ensure result reliability, 10 indentations were measured on each specimen.

3. RESULTS AND DISCUSSION

3.1 Heat Treatment Process

3.1.1 Homogenization at 300°C or 380°C

Homogenization treatment helps to increase the uniformity of the material by eliminating composition segregation, non-equilibrium phases and stresses induced during casting solidification. Studies showed that homogenization treatment can effectively improve microstructure uniformity and distribution of the $Mg_{17}Al_{12}$ phase, as well as enhance mechanical properties of magnesium alloys [26,27]. In order to improve the uniformity of microstructure, the as-cast AZ80 Mg alloy specimens were first homogenized at 300°C for 10 h followed by air cooled. A comparative study with homogenization at 380°C for 10 h with cooled air was conducted to determine the optimal homogenization temperature prior to solution treatment. The typical microstructure of AZ80 magnesium alloy in the as-cast condition and a microstructural comparison of dissolution of secondary phases in different temperatures are shown in Fig. 2. It can clearly be observed that dissolution of β-$Mg_{17}Al_{12}$ phase and eutectic α+β phase had occurred. Microstructures with dendritic arm segregation formed during the solidification process and discontinuous precipitation or lamellar eutectic α+β phase are clearly visible in the as-cast condition as shown in Fig. 2(a) and (b). At 300°C, the network β-$Mg_{17}Al_{12}$ phase along the grain boundary was found to have broken down, the thickness of β-$Mg_{17}Al_{12}$ phase was reduced and eutectic α+β phase was also partially dissolved into α-Mg matrix (see Fig. 2c and d). However, at 380°C, the coarse eutectic β-$Mg_{17}Al_{12}$ had clearly further broken down (see Fig. 2e and f). The dendritic structure and eutectic α+β phase entirely disappeared and grain formation could be observed. Also, the vast amount of coarse β-$Mg_{17}Al_{12}$ phase decreased dramatically and this helped to improve the microstructure homogeneity as compared to the as-cast condition. This can be seen consistently with an image analyzer in the area fraction of β-$Mg_{17}Al_{12}$ phase (see Fig. 2g). The area fraction of β-$Mg_{17}Al_{12}$ phase was decreased from 25.6% (as-cast condition) to 21.6% (at 300°C) and 7.3% (at 380°C). This implies that the higher the temperature is, the faster the rate of dissolution of the eutectic $Mg_{17}Al_{12}$ phase and the lower the fraction of β-$Mg_{17}Al_{12}$ phase are expected to be. However, too high a homogenization temperature or that which is above the eutectic should be avoided. Hence, homogenization at 380°C (denoted as 1st solutionizing) is selected as the optimum homogenization temperature to produce the best microstructure.

3.1.2 Solutionizing Process (T4 & T4X)

The selected solutionizing temperature used should be below the eutectic temperature of 437°C to prevent eutectic melting due to over-heating. In this study, as-cast AZ80 Mg alloy was first solutionized at a lower temperature to partially dissolve the eutectic of $Mg_{17}Al_{12}$ and subsequently heated near to the eutectic temperature for better dissolution of undissolved phases. Figure 3 illustrates the evolution of microstructure for as-cast, homogenization, solutionizing condition for T4 and T4X, and their respective area fraction of β phase. As presented in Fig. 3a, the as-cast alloy exhibits a rather inhomogeneous microstructure with coarse eutectic β-$Mg_{17}Al_{12}$ phase network mainly distributed around the grain boundaries. A relatively high proportion of coarse eutectic $Mg_{17}Al_{12}$ phase had clearly dissolved in α-Mg matrix after homogenization at 380°C for 10 h (Fig. 3b). Also, it can be seen that a fine β phase network is still segregated in the small remaining grain boundaries. In addition, the interdendritic structure was still observed to be segregated at the grain boundaries in T4 (Fig. 3c) as compared to T4X (Fig. 3d). This showed an increase in solute solubility for T4X and suggests a supersaturated of grains formation.

Moreover, from Fig. 3e and f, it were observed that there is a significant reduction in area fraction of β-$Mg_{17}Al_{12}$ phase after T4X. The amount of the dissolution of β-$Mg_{17}Al_{12}$ phase varies dramatically from 2.86% to 0.16% in the microstructure after T4 (Fig. 3e) and T4X (Fig. 3f), respectively. This implies that T4X could further improve the homogenization of microstructure, promote dissolution of eutectic phases and increase solute diffusion into the matrix while maintaining a stable grain microstructure. Further, the corresponding SEM images in Fig. 3g and h show that some insoluble particles are observed at grain interiors. These chunky, irregular shaped particles are identified by EDS as Al-Mn intermetallic compounds which are formed during solution treatment when traces of manganese and aluminium are present. This suggests that the intermetallic compound of Al-Mn was not significantly dissolved during solutionizing at 420°C. These results are in agreement with the findings of Braszczyńska-Malik [28] who reported that only the intermetallic compound Al_8Mn_5 did not undergo any notable changes after heat treatment.

After solutionizing, the grain size increased slightly as compared to as-cast specimens (see Table 1). The average grain size was increased from as-cast condition 91µm to 127µm (T4) and 111µm (T4X). This showed that the T4X involving an additional 10 h of soak time was supposed to lead to growth in grain size but in this case, it was still capable of maintaining a smaller grain size even though the soak time was longer. A complete dissolution of secondary phases occurred in T4X, followed by nucleation when grain growth stagnated. The smaller grains began to develop inside the larger grains and thus the finer grains were observed. The finer grains may be attributed from maximum solubility of solute elements that resulted from a supersaturated solid solution. With the maximum solubility of solute, the mobility of boundaries may be restricted and against the grain growth. Most research efforts studied were focused on explaining the solute content and the grain microstructure during casting solidification process in Mg-Al alloys [29-32]. In particular, Cáceres et al. [33] studied the solid solution strengthening on Mg-Al alloys and demonstrated that there is correlation between the solute Al content and the grain size, i.e. 8% Al more favorably to achieve a finer grain size of 95µm, which is in good agreement with current work. However, the effects of $Mg_{17}Al_{12}$ phase solubility on morphology during solution treatment were not clearly discussed in those studies. Another factor that contributed to the finer grain size could be due to formation of annealing twins during solutionizing process. It is interesting to observe from microstructural studies that multiple twinning variants are formed after solutionizing in T4, as shown in Fig. 4 (a) and (b). The variants appeared as both parallel lines and lenticular shape. Likewise, multiple twinning was observed in Fig. 4(c) and (d). In contrast, T4X induced more twinning as compared to T4 and has a more complicated microstructure with more complex morphology and texture. Also, T4X which is being susceptible to multiple twins formation, yielding better control in grain size stability. It is well known that pure magnesium and its alloys exhibit twinning after deformation by mechanical processing such as extrusion, compression, rolling etc. It can be identified as a type of twinning caused by deformation and annealing. However, most research works [34-37] have focused

on reporting the effect of deformation twins on AZ80 Mg alloys but limited studies were done on annealing twins. The studies on annealing twins on other cast alloys are rather limited. Figure 4(e) revealed multiples twins from one grain of T4X specimen. This result is in agreement with the findings of Syam Prasad et al. [38] and Jia Hongmin et al.[39] on ZE41 and Mg-4Zn alloys respectively, they consistently reported that thermally induced twins were observed in cast Mg alloy after solutionizing. The twin formations observed in this study are considered annealing twins. The annealing twins or transformation twins formed are caused by changes in the normal growth mechanism and phases during crystal transformation [40] Comparatively, T4X has a more complicated microstructure with more complex morphology. In this research work, the lenticular like lens shape twinning formed without being subjected to any mechanical deformation process. Lenticular shape twinning is usually formed during plastic deformation. According to literature, such formation of twinning could occur during the solid phase transformation or casting solidification process [40,41]. The initial homogenization process at 380°C for 10 h help improve the dissolution of $Mg_{17}Al_{12}$ eutectic structure and increase the solid solubility of Zn and Al in α-Mg matrix in the process. During the subsequent solutionizing at a higher temperature of 420°C for 10 h, recrystallization could occur in some grains and twin formation with parallel line occurred in association with grain growth. The mechanism for the formation of multiple annealing twins in T4X can be attributed to higher solute solubility in the matrix and the stored energy after homogenization providing a greater driving force for recrystallization [40]. This is also likely to promote the formation of stable fine grain sizes during the subsequent aging process. The experiment results indicate that T4X is susceptible to twin formation. It shows convincing evidence that the presence of twin formation is influenced by the development of texture of the solutionized condition, leading to stable grain size and finally enhancing the yield strength. This study revealed that twinning was suppressed after aging, and this led to a strong evolution of the aging texture. As a consequences, increase in strengthening effect on cast AZ80 Mg alloy.

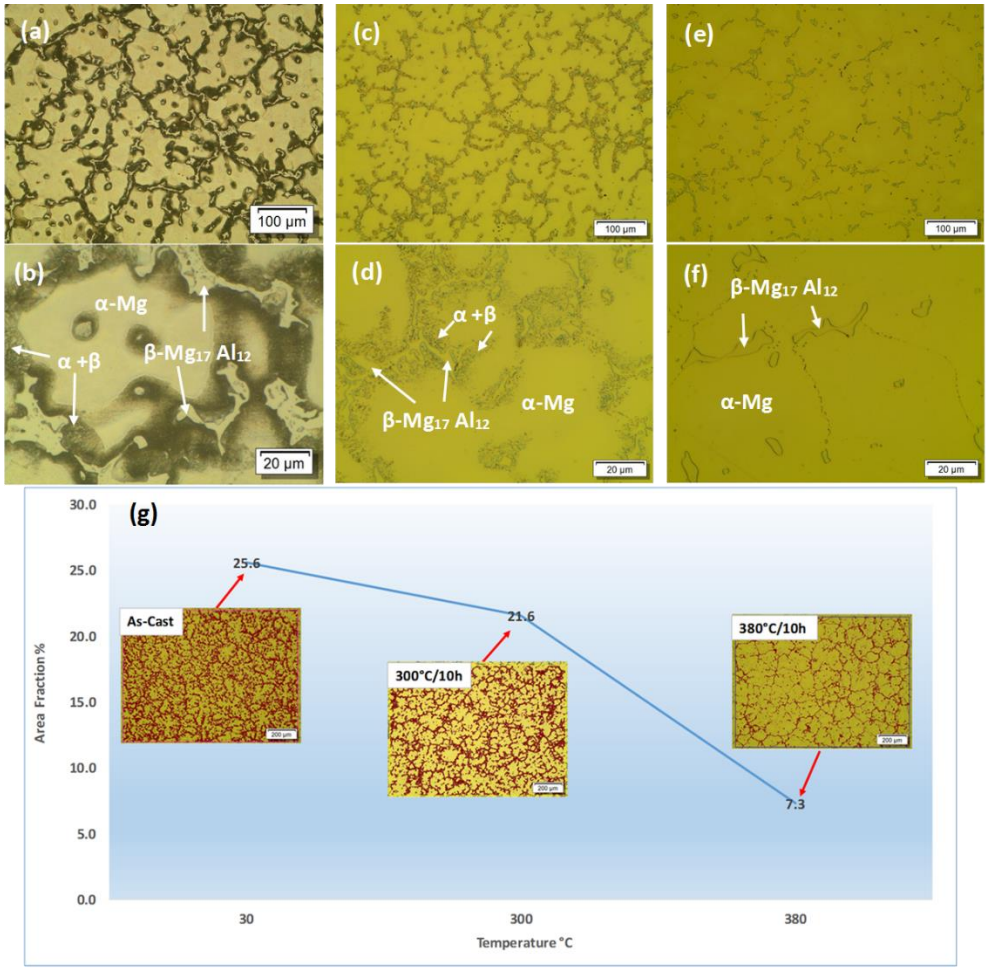

Fig. 2 Microstructure of AZ80 Mg alloy with OM (a)-(b) as-cast condition; (c)-(d) after homogenization at 300°C/10hours; (e)-(f) after homogenization at 380°C/10hours; (g) Effect of temperature on area fraction of β phase

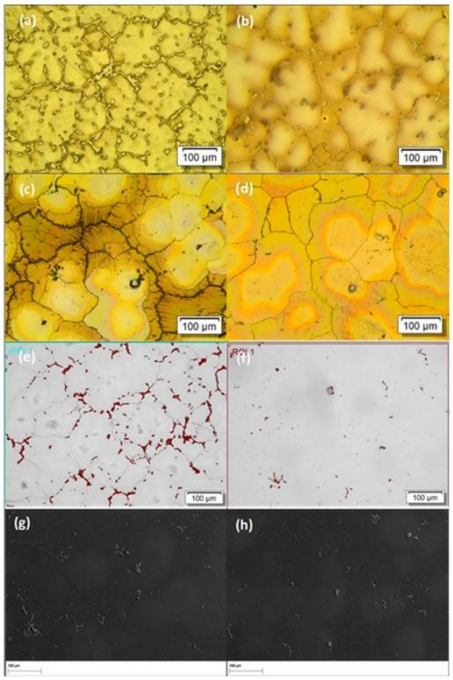

Fig. 3 Microstructure for (a) as-cast; (b) homogenized at 380°C; (c), solutionizing at 420/10 h with water quench (T4); (d) two-step solutionizing (T4X); (e) area fraction for T4 $F_A\beta$ = 2.86%; (f) area fraction for T4X $F_A\beta$ = 0.16%; (g) SEM image for T4; (h) SEM image for T4X

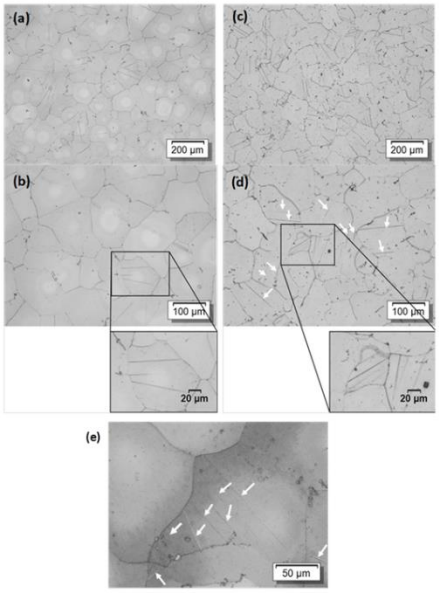

Fig. 4 Optical micrograph showing twinning formation in (a)-(b) T4 condition; (c)-(d) T4X condition; (e) multiples twins in a grain of T4X. Twins are labelled with arrows

Table 1 Grain size measurement and volume fraction ($Mg_{17}Al_{12}$) for HT Conditions

HT Conditions	Specimen ID	Average Grain Size (µm)	Volume Fraction % of $Mg_{17}Al_{12}$
F	As Cast	90.69±1.07	11
T4	S10WQ	127.25±7.10	2
T4X	SS10WQ	111.41±4.92	1
T6	S10WQ-A10	99.00±3.41	16
T6X	SS10WQ-A10	91.00±2.89	11

3.1.3 Solutionizing with aging (T6 & T6X)

SEM image as shown in Fig. 5 revealed that T6 and T6X condition developed with variations in precipitation morphology. The microstructure in as aged condition is generally characterized by the formation of continuous precipitates (CP) and discontinuous precipitates (DP). The nucleation for these two types of precipitates were shown to grow differently. Both types of precipitates occurred competitively and simultaneously. The precipitate morphology of the β-phase in Mg-Al is highly dependent on the temperature and soak time [42,43]. It is noticed that T6 (Fig. 5a) resulted in the formation of distinct DP and dominant morphology. Figure 5b show the formation of the DP with lamellar structures and the CP finely distributed in an orderly parallel manner. CP grows within the parent grain whereas discontinuous precipitate grows at grain boundaries. The CP as presented in Fig. 5c appeared to be lath shaped with long and short lengths, in a specific orientation with respect to the habit plane and matrix. However, a higher area fraction of fine CP is observed in T6X (Fig. 5d). The CP of lath structure for T6 and T6X constituted about 30-40% and 60-70% of area fraction, respectively.

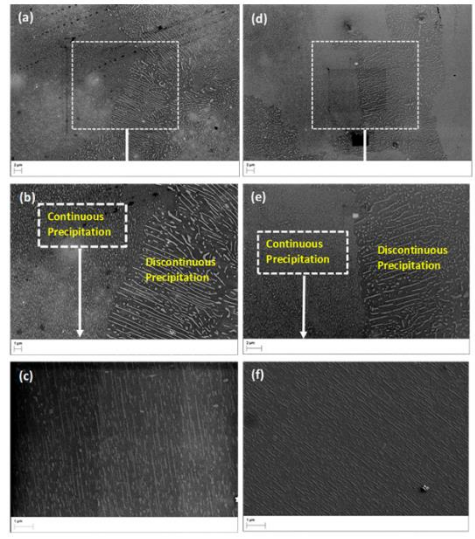

Fig. 5 SEM Micrograph showing DP and CP with different heat treatment: (a)-(c) T6 condition; (d)-(f) T6X condition

In this research work, it was observed that the CP were dominant as compared to DP in T6X. It can be attributed to the increase in supersaturated solid solution and twins formation that accelerates the formation of higher amounts of CP. The result is in

agreement with K.N. Braszcyńska-Malik [44] who reported that the twins boundary constitute favorable to form continuous precipitates after annealing of cast AZ91. The development of CP is important as the mechanical properties are highly dependent on its volume fraction. In Fig. 5(f), fine and thin lath shapes of CP are observed in SEM images of T6X. Also, the CP of T6X was observed to be denser as compared to T6.

In addition, it is known that the discontinuous precipitation reaction is characterized by a discontinuous change in orientation and composition between the matrix and across the migration boundary [45]. The DP nucleate and grow at the grain boundaries in the parent phase due to the relatively high energy that is a result of dislocations and defects [15]. With higher magnification as shown in Fig. 6a, SEM examination revealed clearly the DP at grain boundary growing behind a migration reaction front (RF). Its growth rate is dependent on volume diffusion of the solute in the matrix phase [46]. When the DP grow, the grain boundary was carried along with them. Besides the irregular shape of the lamellar structure, there were globular precipitates found surrounding the lamellar as shown in Fig. 6(b). This could be due to the spheroidization process, in which the partially lamellar structures break down into discrete precipitates. The occurrence of this reaction influences the changes in precipitate morphology. Figure 6(c) and (d) show a large volume of smaller globular formation with irregular slab structures observed in the DP region of T6X specimen. This shows that T6X leads to more fragmentation and spheroidite formation. There were more spherical shaped, discontinuous precipitates with thinner and shorter length, as well as more breakdowns of lamellar and globular precipitates at the grain boundaries. It was also observed that there was a lesser formation of lamellar with shorter length and width. The growth of DP was greatly reduced, though not completely suppressed. Similar to the T6, the T6X microstructure shows that there was a different orientation relationship between the precipitation habit plane and matrix [45]. Manna et al. [47] reported that the morphology of discontinuous precipitation is usually in lamellar structure, sometimes fibrous shaped and very seldom in a globular form. However, the current study showed theformation of larger amounts of globular structures instead of lamellar structures, indicating that T6X would enhance ductility. The presence of globular precipitates results in improvements in plasticity whereas lamellar precipitate decrease plastic properties of the alloys [48].

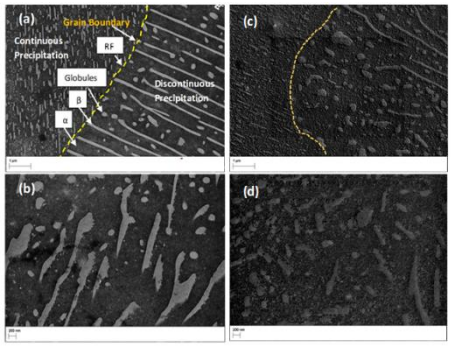

Fig. 6 The precipitate microstructure of AZ80 alloy with processes (a)-(b) T6 condition with long and wider discontinuous precipitates; (c)-(d) T6X condition with spherical shape and shorter discontinuous precipitate

Besides, TEM investigation was performed and revealed the growth of continuous precipitate particles with different morphology for T6 and T6X. Figure 7 showing TEM images with bright field imaging clearly showing the morphology and distribution of β precipitates in T6 and T6 specimens. The precipitates in both specimens appeared in lath shape with their habit planes and grow along a direction a parallel to the basal plane of the matrix $(0001)_\alpha$ and with small amount of lens-shaped precipitates are lying in the basal plane. These precipitates are reported with the predominant of Burger OR with the matrix [43,49,50]. In T6 specimen as shown in Fig. 7a, less precipitates particles had been formed in the Mg matrix as compared to Fig. 7b (T6X). Under the higher magnification (see Fig. 7c and d), it could be seen that most precipitates had shorter lengths, larger interparticle spacing distance and formed in small volume fractions in Fig. 7c. The sizes of precipitates were 17-47nm in width. In contrast, precipitates in Fig. 7d (T6X) had grown to their maximum length and are thin & long, lath shaped and with a larger aspect ratio as compared to Fig. 7c (T6). Their particle sizes were reduced to 13-30nm width morphology (Table 2). A few precipitates were short and lath shaped. More precipitates with the lath-shaped precipitates were dominated, the volume fraction and number density of precipitates are increases as well. Comparison with literature, the precipitates in T6 and T6X specimens were found to be much smaller in size (refer to Fig. 7e for ease of reference). In addition, the interparticle spacing measured are significantly reduced for T6X specimen with an average of 40nm and that will influence on the strength. This implies that T6X has better ability to produce fine dispersion of precipitates with smaller the interparticle spacing and that could further resist the dislocation movement and improved strength of this alloy. Table 2 shows the summary results of the measured particle size and interparticle spacing for both T6 and T6X specimens. Generally, the width and length of the precipitate in the T6X specimen was determined to be shorter than the T6 specimen. However, some longer length of precipitates still were observed in T6X specimen. As reported by Celotto [43], the lath had grown to the maximum length with no significant change in thickness when the maximum hardness is achieved. In this study, precipitates that were thinner in size could be due to longer soak times during T6X that resulted in changes in the morphology of the continuous precipitates.

Table 2 Particle size and interparticle spacing for representative specimens of T6 & T6X

HT Condition	Particle Size		Inter-Particle spacing (nm)	Hardness ($HV_{0.1}$)
	Width (nm)	Length (nm)		
T6	17 - 47	173 - 253	143-331	83.5
T6X	13 – 30	132 - 479	30-121	86.0

In addition, formation of greater amount of precipitates finely dispersed and with moiré fringes contrast were observed in T6X specimen, as illustrated in Fig. 8a (T6X). More dislocations appearing as curved dark lines running through the precipitates are lying primarily in the basal plane of T6X specimen as shown in Fig. 8b and c. It is clearly observed that some precipitates are bypass dislocation lines and this interaction could cause the climbed or bowed out between the precipitates by Orowan mechanism for strong obstacles. Also, most precipitates appear to be distributed on or near dislocation lines, and this dislocation is more favorable to the formation of a precipitate nucleation site. Besides, moiré pattern contrast showed dislocation-precipitate particles interaction at both ends and dislocation gliding was observed due to precipitate overlap. It also appears from the center of precipitate particles. This dislocation gliding in the matrix is not capable of cutting through those precipitates which act as strong obstacles for greater strengthening effect [52]. The

hardness of β-$Mg_{17}Al_{12}$ is much higher than α-Mg matrix. This observation further demonstrated that the T6X specimens produced strong precipitate particles that effectively hinder dislocation movements and resulted in a better age-hardening response compared to the T6 specimen, which is also in good agreement with the measured tensile results.

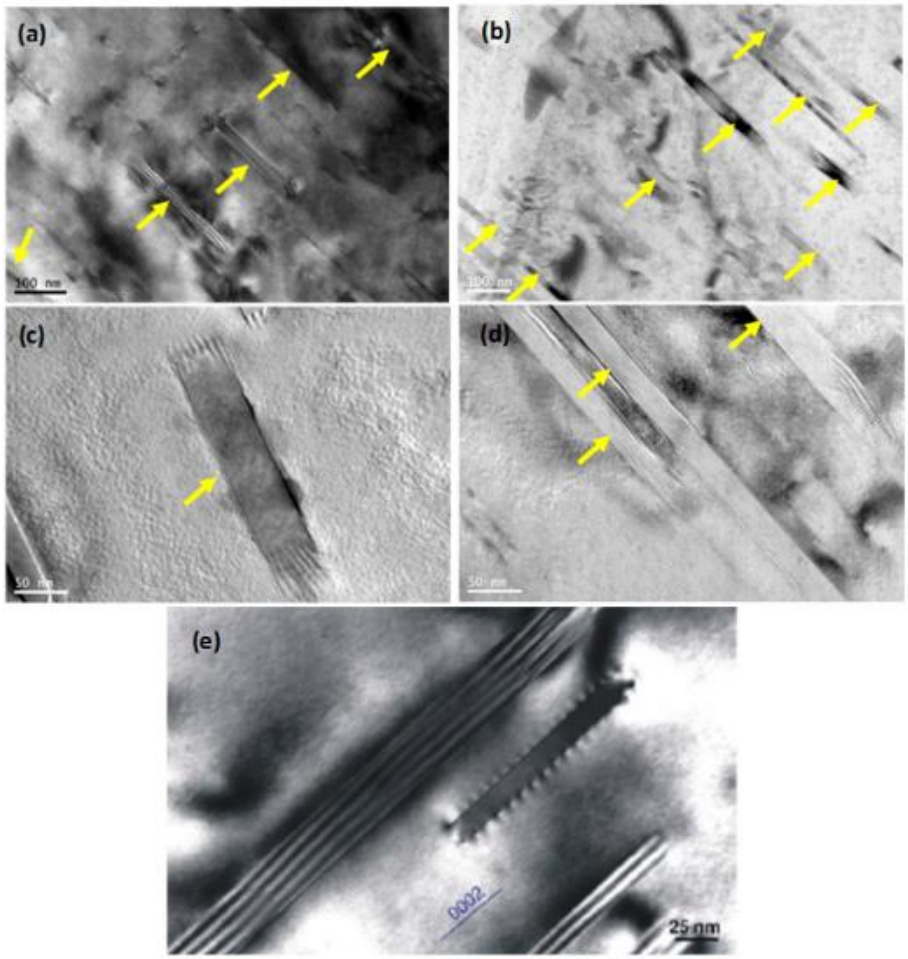

Fig. 7 TEM images showing lath-shaped precipitate morphology for (a)–(b) T6 condition; (c)–(d) T6X condition; (e) AZ91 after aged sample for ease of reference, source adapted from Ref.[51]. Precipitates are labelled with yellow arrow

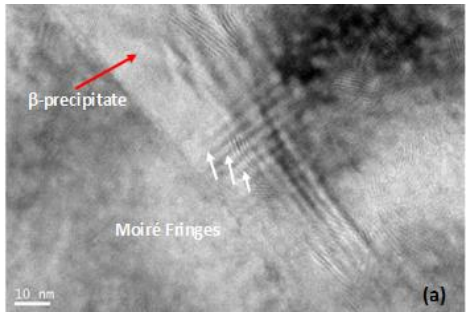

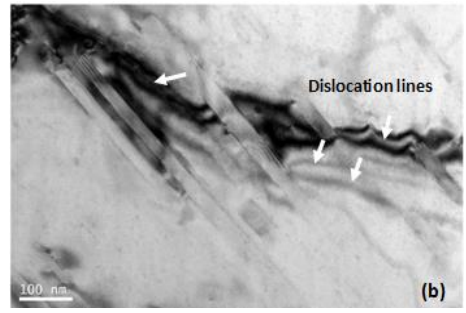

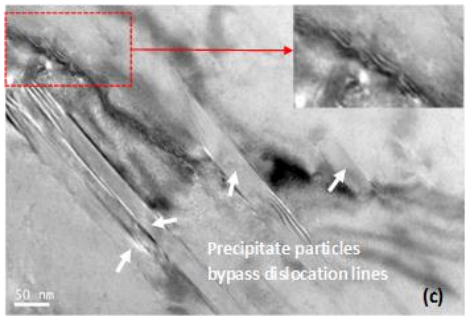

Fig. 8 TEM image for T6X condition showing (a) multiples overlapping of precipitates and with strong moirè patterns contrast (precipitates with white arrow); (b) dark curves showing the dislocation lines with dislocation bypass precipitate particles; (d) enlarge the image from (b)

Under the dark field images, the selected area electron diffraction (SAED) patterns showed that all precipitates particles as analyzed are identified as $Mg_{17}Al_{12}$ particles. TEM dark field image and corresponding diffraction pattern of T6 specimen and T6X specimen are illustrated in Fig.9a and c, respectively. SAED pattern shows the single crystals present in T6 specimen (see Fig. 9b) with diffraction spots that indexing (needs rephrasing) to be Mg. In contrast, ring diffraction patterns were observed for T6X (see Fig. 9d) due to multiple crystals. It was produced by diffraction from the polycrystalline Mg alloy which make-up of many tiny single crystals. Those precipitates are from different planes and within randomly orientated crystals. Evidence of Debye ring pattern formation in SAED showed that T6X condition is capable of attaining precipitate density with higher numbers compared to T6. From the diffraction rings obtained, the type of crystal structure and the lattice parameters is identified as fine $Mg_{17}Al_{12}$ precipitates. There is not possible to determine the orientation of a polycrystalline Mg, since there is no single orientation and flipping or turning the polycrystalline Mg will yield the same ring pattern. As for those diffraction spots, it was identified as Mg. However, further with the evidence of the diffraction ring pattern for detected on T6X specimen proved that the large formation of precipitates colonies with this process that changed of the morphology and produced a strong texture of microstructure.

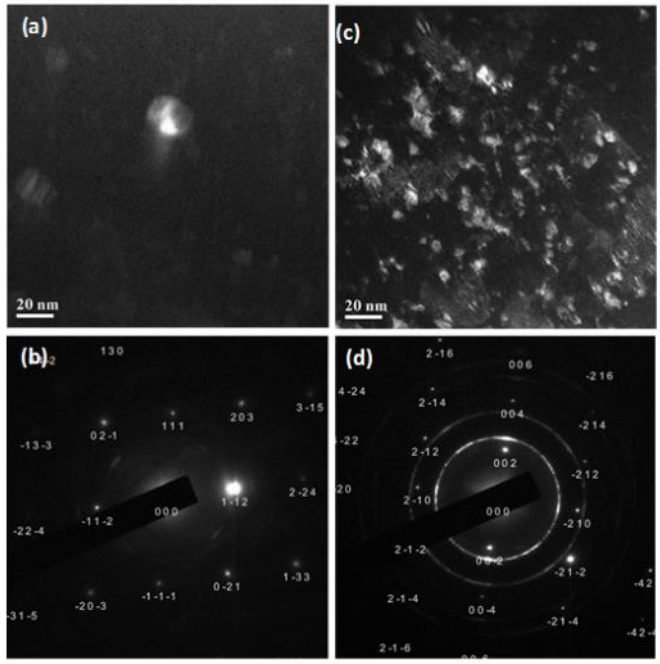

Fig. 9 TEM with dark field imaging showing distribution of precipitates for (a-b) diffraction spot and diffraction pattern corresponding for T6 specimen, (c-d) diffraction spot and diffraction pattern corresponding for T6X specimen

Under XRD analysis, there were no signs of β-$Mg_{17}Al_{12}$ phase for solution treated condition at T4 and T4X as shown in Fig. 10a. The XRD results further confirmed the dissolution of β-$Mg_{17}Al_{12}$ phase, these were consistent with the metallographic observations. However, the β-$Mg_{17}Al_{12}$ phase reappeared after aging, where its diffraction pattern was observed for T6 and T6X. The β-$Mg_{17}Al_{12}$ phase was found to have precipitated from the supersaturated solid solution and formed disperse precipitates. Also, it can be clearly observed that β-$Mg_{17}Al_{12}$ phase diffraction peak had less formation of $Mg_{17}Al_{12}$ for T6X specimen. Both enlargement spectrums shown in Fig. 10(b) indicated higher concentrations of β-$Mg_{17}Al_{12}$ phase. The result was consistent with the quantitative XRD analysis, in which the measured volume fraction was 11 and 16wt% of β-$Mg_{17}Al_{12}$ phase for T6X specimen and T6 specimen respectively (see Table 1). It is well known that as the $Mg_{17}Al_{12}$ content decreases, the ductility increases due to the brittleness of $Mg_{17}Al_{12}$ [53]. Hence, the evidence of presented results indicates that the lower volume fraction in T6X could lead to enhanced ductility.

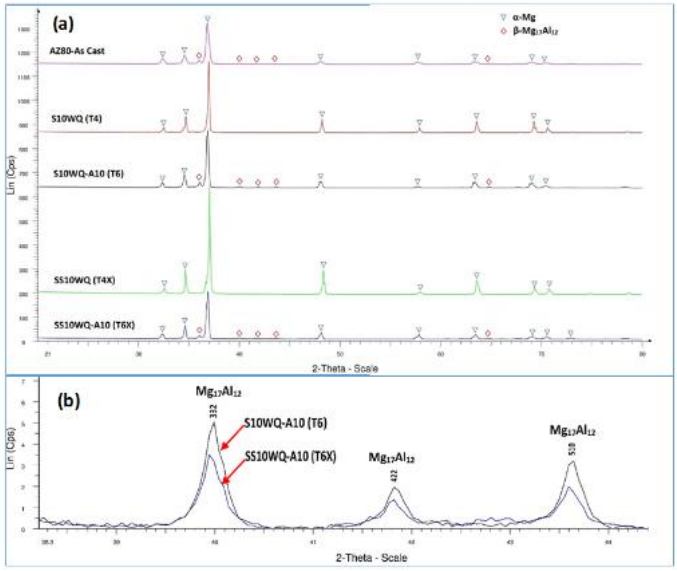

Fig. 10 Comparison on X-ray diffraction patterns of AZ80 in (a) As-cast, T4, T4X, T6 & T6X specimens; (b) enlargement of spectrum for T6 and T6X specimens

3.2 Mechanical Characteristics

Figure 11 shows the engineering stress-strain curves for cast AZ80 Mg alloy subjected to T6 and T6X condition. Also, a summary of the mechanical properties of current work at various heat treated conditions compared with published works for cast AZ80 Mg alloy are listed in Table 3. For this study, the UTS did not change significantly for T4X as compared to T4. It is most likely because the material had reached the peak of super-saturated and the effect of any rise in tensile strength is negligible even with the introduction of two-step solution treatment. In comparison to as-cast (106MPa) and solution treated condition, YS dropped almost 14% after T4 (91MPa). This can be attributed to grain growth and reduction in the volume fraction of β-$Mg_{17}Al_{12}$ phase, as shown in Table 1. Also, another contributing factor could be increased interlamellar spacing, which was studied in a previous work [19]. However, it is noticeable that the YS changed slightly in T4X (102MPa). This could be due to the fact that T4X tends to form higher amounts of multiple twins, which accounts for the stable structure and prevents further grain growth.

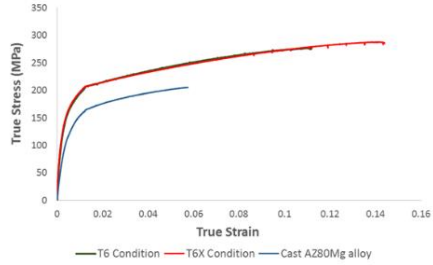

Fig. 11 True stress-strain curve for representative samples of as-cast, T6 and T6X conditions

Table 3 Mechanical Properties of AZ80 Mg alloy for various heat treatment processes

HT Condition	Specimen ID	Tensile Properties			Hardness ($HV_{0.1}$)	Ref.
		UTS (MPa)	YS (MPa)	Elongation (%)		
F	As-Cast	191 ± 1	106 ± 2	6.3 ± 0.3	61.2 ± 2.8	
T4	S10WQ	274 ± 6	91 ± 4	16.0 ± 1.3	64.0 ± 4.1	
T4X	SS10WQ	266 ± 7	102 ± 8	16.0 ± 3.1	63.7 ±2.8	
T6	S10WQ-A10	287 ± 1	156 ± 5	9.0 ± 0.5	83.5 ± 4.5	
T6X	SS10WQ-A10	287 ± 2	143 ± 1	13.0 ± 0.4	86.0 ± 3.0	
T6	Cast AZ80	199.41	126.32	3.66	76.3	Zhang et al. [15]
T6	Cast Al A356	221	152	2		AMS 4218J

After T6X, the yield strength was found to be slightly lower as compared to T6. It was likely caused by the slight grain coarsening in T6X (see Table 1) as compared to T6. An exceptional tensile result show both heat treatment processes achieved almost similar ultimate tensile strength at 287MPa. The tensile strength increased significantly (+50% compared to as-cast) after aging. Also, it was observed that the elongation to failure after T6 and T6X is 9% to 13% respectively. The results show that ductility of T6X increases almost 106% compared to the as cast condition (6.3%). This indicates that T6X contributed

greatly to the achievement of better integrated mechanical properties. This could be due to the T6X enhancing the nucleation rate by breaking down the lamellar into discrete particles. The reason for the combination of high strength and ductility of T6X is mainly attributed to the change in precipitation morphology. This can be explained by the combination of greater degree of supersaturated solution and formation of twinning that impeded the dislocation movement. Also, subsequent aging process (T6X) led to the formation of low volume fractions of $Mg_{17}Al_{12}$ and high volume fractions of CP with high density of precipitates. This can significantly improve strength and ductility simultaneously

After aging, the average hardness value was found to increase by 36-40% as compared to the as-cast condition ($61.2HV_{0.1}$). It reached $83.5HV_{0.1}$ and $86HV_{0.1}$ after aging on test specimens for T6 and T6X respectively. Overall, the hardness of aged AZ80 Mg alloy was higher as compared to the as-cast condition due to the solid solution strengthening effect involving the transformation of the supersaturated solid solution to fine precipitates in the matrix and for precipitation hardening.

In order to investigate the fracture behavior, the tensile fracture specimens were examined with SEM as shown in Fig. 12. The fracture behavior for as-cast condition, T6 and T6X specimens are illustrated in Fig. 12a, b and c, respectively. It can be observed in Fig. 12 b and c that both fracture surfaces for T6 and T6X were found to have many parallel plateaus and ledge morphologies which characterize as mixed cleavage fracture mode with the faceted feature and quasi-cleavage fracture. However, the ductile features appear to be more in T6X as compared to T6 specimen. A large plastic deformation zone was observed in Fig 12(c) as compared to Fig. 12(b). As the size of the plastic deformation zone increases, the mechanism of fracture tends towards ductile tearing which is considered as a more ductile fracture. However, both fracture surfaces were found to have many parallel plateau and ledge morphology which can be characterized as mixed cleavage fracture mode. Quasi-cleavage fracture was also observed. The T6X specimen showed a faceted cleavage fracture with more flat face steps but are less wide as compared to the T6 specimen. Under an enlargement of ductile surface region tensile fractography morphology of as-cast condition, T6 and T6X (see Fig. 12d, e and f), it clearly shows with dimples of different sizes and precipitated particles. It also indicates that T6X (Fig. 12f) exhibited more uniformly distribution of smaller precipitated particles as compared to T6 (Fig. 12e). Large colonies of relatively fine precipitated particles, which were nucleated in dimples, could be attributed to enhance both strength and ductility. During the application of tensile stress, plastic deformation is first initiated in the precipitated particles/Mg matrix interface and that leads to the occurrence of decohesion and microvoids formation. With more precipitated particles, it is enabling higher energy absorption with the grain pullouts and repulsion mechanism (needs rephrasing) and led to larger strain to fracture through the interface and thus, increasing ductility.

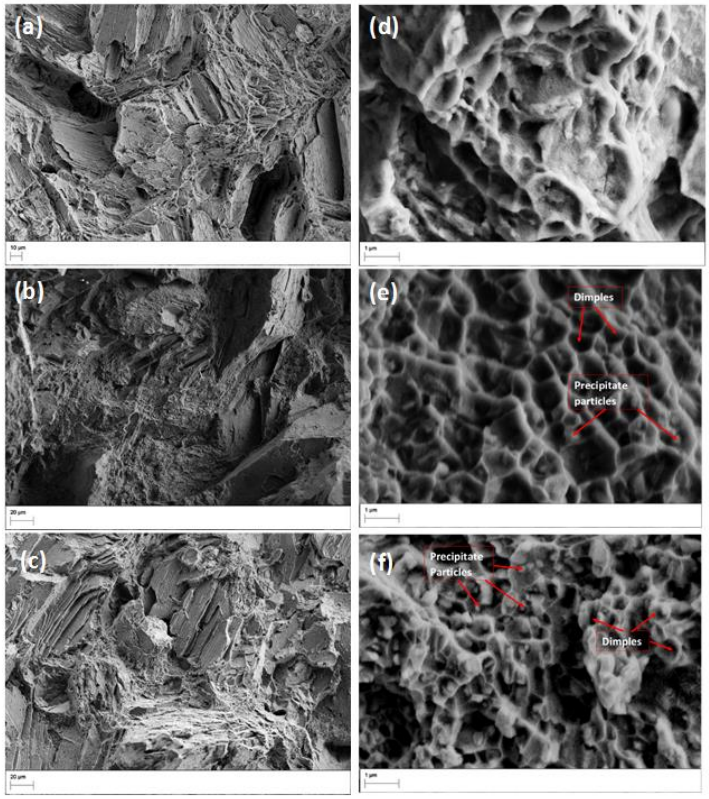

Fig. 12 SEM images showing the variation of appearances of tensile fracture surfaces with ductile features (a-b) as-cast condition; (c-d) T6 condition with large dimples with precipitated particles; (e-f) T6X condition with smaller dimples and a large number of precipitated particles

CONCLUSION

In this study, conventional heat treatment (T6) and current heat treatment (T6X) were performed on the as-cast AZ80 Mg alloy. The following conclusions were made:

- A distinctive solutionizing process was performed at 380°C/10 follow up 420°C/10 and aged at 200h/10h.
- T6X led to more fragmentation and spheroidization with smaller globular precipitates and lesser volume fraction of DP. This resulted in a higher proportion of lath CP dispersed uniformly in the matrix greatly produced an improved combination of mechanical properties. Besides, T6X exhibits more dislocation-precipitate interactions through the Orowan loop mechanism and has produced strong obstacles to dislocation movement. This indicated a better aged-hardening response.
- In addition, Debye ring diffraction pattern was observed for the T6X specimen. The evidence of the diffraction ring pattern proved that large formation of precipitates colonies and with a high number of density produced with this process would contribute to a strong microstructure texture.
- Moreover, tensile fractography studies have shown distinct features for both fracture surfaces of the T6 and T6X specimens. The results of the fractography examination showed that the combination of high ductility and high strength in T6X is due to the presence of large amounts of fine precipitate particles-nucleated in dimples, small dimples in size, decreased interspacing between precipitate and fine precipitate with a large volume fraction.
- The mechanical properties of cast AZ80 Mg alloy with T6X were superior to T6. Significant improvements in a combination of strength and ductility were achieved with increases in UTS (50.3%), YS (35%), elongation (106%) and hardness (40%) as compared with as-cast condition of AZ80 Mg alloy.

Acknowledgements

The authors are grateful for the funding support from ST Engineering Land Systems Ltd. Special thanks to the late Associate Professor Philip Cheang for his great support and encouragement.

REFERENCES

1. Huang SJ, Li CR, Yan KL: Particle reinforcement of magnesium composites SiCp/AZ80 and their mechanical properties after heat treatment. Kovove Materialy 51 (1), 2013, 45-52. https://doi.org/10.4149/km_2013_1_45.
2. Khoshzaban Khosroshahi H, Fereshteh Saniee F, Abedi HR: Mechanical properties improvement of cast AZ80 Mg alloy/nano-particles composite via thermomechanical processing. Materials Science and Engineering A 595, 2014, 284-290. https://doi.org/10.1016/j.msea.2013.12.029.
3. Matin A, Saniee FF, Abedi HR: Microstructure and mechanical properties of Mg/SiC and AZ80/SiC nano-composites fabricated through stir casting method. Materials Science and Engineering A 625, 2015, 81-88. https://doi.org/10.1016/j.msea.2014.11.050.
4. Yin DL, Weng LK, Liu JQ, Wang JT: Investigation of microstructure and strength of AZ80 magnesium alloy by ECAP and aging treatment. Kovove Materialy 49 (1), 2011, 37-42. https://doi.org/10.4149/km-2011-1-37.
5. Tang L, Zhao Y, Islamgaliev R, Valiev R: Enhanced strength and ductility of AZ80 magnesium alloys by spray forming and ECAP techniques, KnE Materials Science, 2016, 168-171. https://doi.org/10.18502/kms.v1i1.580.
6. Wang PC, Lin CC, Huang TY, Lin HC, Lee YH, Yeh MT, Wang JY: Effects of 2 mass % Li addition on the AZ80 Mg alloy. Materials Transactions 49 (5), 2008, 913-917. https://doi.org/10.2320/matertrans.MC200708.
7. Kashefi N, Mahmudi R: The microstructure and impression creep behavior of cast AZ80 magnesium alloy with yttrium additions. Materials and Design 39, 2012, 200-210. https://doi.org/10.1016/j.matdes.2012.02.036.
8. Wang YX, Fu JW, Yang YS: Effect of Nd addition on microstructures and mechanical properties of AZ80 magnesium alloys. Transactions of Nonferrous Metals Society of China (English Edition) 22 (6), 2012, 1322-1328. https://doi.org/10.1016/S1003-6326(11)61321-6.
9. Wei W, Xu C, Zhang J, Cheng W, Niu X: Effects of Ce addition on microstructure, mechanical properties and corrosion resistance of as-cast AZ80 magnesium alloy. China Foundry 11 (3), 2014, 157-162.
10. Uematsu Y, Tokaji K, Matsumoto M: Effect of aging treatment on fatigue behaviour in extruded AZ61 and AZ80 magnesium alloys. Materials Science and Engineering A 517 (1-2), 2009, 138-145. https://doi.org/10.1016/j.msea.2009.03.066.
11. Wu YJ, Zhang ZM, Li BC: Effect of aging on the microstructures and mechanical properties of AZ80 and ZK60 wrought magnesium alloys. Science of Sintering 42 (2), 2010, 161-168. https://doi.org/10.2298/SOS1002161W.
12. Zhu R, Ji W, Wu Y, Cai X, Yu Y: Effect of aging treatment on low-cycle fatigue behavior of extruded Mg-8Al-0.5Zn alloys. Materials & Design 41, 2012, 203-207. https://doi.org/10.1016/j.matdes.2012.05.015.
13. Yu S, Gao Y, Liu C, Han X: Effect of aging temperature on precipitation behavior and mechanical properties of extruded AZ80-Ag alloy. Journal of Alloys and Compounds 646, 2015, 431-436. https://doi.org/10.1016/j.jallcom.2015.06.126.
14. Yakubtsov IA, Diak BJ, Sager CA, Bhattacharya B, MacDonald WD, Niewczas M: Effects of heat treatment on microstructure and tensile deformation of Mg AZ80 alloy at room temperature. Materials Science and Engineering A 496 (1-2), 2008, 247-255. https://doi.org/10.1016/j.msea.2008.05.019.
15. Zhang J, Jiang B, Wang Z, Yuan S, Nan H, Luo H: Influence of aging modes on microstructure and mechanical properties of AZ80 magnesium alloy. China Foundry 4 (4), 2007, 296-299.
16. Kleiner S, Beffort O, Wahlen A, Uggowitzer PJ: Microstructure and mechanical properties of squeeze cast and semi-solid cast Mg-Al alloys. Journal of Light Metals 2 (4), 2002, 277-280. https://doi.org/10.1016/S1471-5317(03)00012-9.
17. Palai P, Prabhu N, Hodgson PD, Kashyap BP: Grain growth and β-$Mg_{17}Al_{12}$ intermetallic phase dissolution during heat treatment and its impact on deformation behavior of AZ80 Mg-alloy. Journal of Materials Engineering and Performance 23 (1), 2014, 77-82. https://doi.org/10.1007/s11665-013-0722-9.
18. Kadali K, Dubey D, Sarvesha R, Kancharla H, Jain J, Mondal K, Singh SS: Dissolution kinetics of $Mg_{17}Al_{12}$ eutectic phase and its effect on corrosion behavior of as-cast AZ80 magnesium alloy. JOM 71, 2019, 2209-2218. https://doi.org/10.1007/s11837-019-03470-3.
19. Yeoh MK, Tan XH, Cheang PHN, Lim TC, Kwok RWO: Effect of solutionizing time on improving the microstructure and mechanical properties of aged AZ80 Mg alloy. Journal of Materials Engineering and Performance 28 (11), 2019, 6836-6852. https://doi.org/10.1007/s11665-019-04382-8.
20. Dini H, Andersson NE, Jarfors AEW: Effect of $Mg_{17}Al_{12}$ fraction on mechanical properties of Mg-9%Al-1%Zn cast alloy. Metals 6 (10), 2016, 251. https://doi.org/10.3390/met6100251.
21. Liang S, Ma Y, Chen R, Han E: Optimization of heat treatment in AZ64 magnesium alloy. Materials Transactions 49 (5), 2008, 986-989. https://doi.org/10.2320/matertrans.MC200756.

22. Shuai D, Feng W, Zhi W, Zheng L, MAO P-l: Enhanced strengthening by two-step progressive solution and aging treatment in AM50-4%(Zn, Y) magnesium alloy. Transactions of Nonferrous Metals Society of China 28 (12), 2018, 2419-2426.
23. Zhang J, Yuan F, Du Y: Enhanced age-strengthening by two-step progressive solution treatment in an Mg-Zn-Al-Re alloy. Materials and Design 52, 2013, 332-336. https://doi.org/10.1016/j.matdes.2013.05.074.
24. *Heat Treating*, Vol 4., ASM International, Ohio, 1991 .
25. *Metallography and Microstructures*, Vol 9, ASM international, Cleveland, 2004.
26. Wu YJ, Zhang BH, Yang YB, Zhang ZM: Effects of homogenizing and extrusion on elongation of as-cast AZ80 magnesium alloy. Advanced Materials Research 626, 2013. https://doi.org/10.4028/www.scientific.net/AMR.626.386.
27. Zheng L, Nie H, Liang W, Wang H, Wang Y: Effect of prehomogenizing treatment on microstructure and mechanical properties of hot-rolled AZ91 magnesium alloys. Journal of Magnesium and Alloys 4 (2), 2016, 115-122. https://doi.org/10.1016/j.jma.2016.04.002.
28. Braszczyńska-Malik KN: Discontinuous and continuous precipitation in magnesium–aluminium type alloys. Journal of Alloys and Compounds 477 (1-2), 2009, 870-876. https://doi.org/10.1016/j.jallcom.2008.11.008.
29. Nagasekhar AV, Easton MA, Cáceres CH: Solute content and the grain microstructure of high pressure diecast magnesium-aluminium alloys. Advanced Engineering Materials 11 (11), 2009, 912-919. https://doi.org/10.1002/adem.200900175.
30. Hou DH, Liang SM, Chen RS, Dong C, Han EH: Effects of Sb content on solidification pathways and grain size of AZ91 magnesium alloy. Acta Metallurgica Sinica (English Letters) 28 (1), 2015, 115-121. https://doi.org/10.1007/s40195-014-0178-4.
31. StJohn DH, Dahle AK, Abbott T, Nave MD, Qian M: *Solidification of cast magnesium alloys*. In: TMS Annual Meeting, 2003, 95-100.
32. Zhang L, Cao Z, Liu Y, Su G, Cheng L: Effect of Al content on the microstructures and mechanical properties of Mg–Al alloys. Materials Science and Engineering: A 508 (1-2), 2009, 129-133. https://doi.org/10.1016/j.msea.2008.12.029.
33. Cáceres CH, Rovera DM: Solid solution strengthening in concentrated Mg-Al alloys. Journal of Light Metals 1 (3), 2001, 151-156. https://doi.org/10.1016/S1471-5317(01)00008-6.
34. Cui Y, Li Y, Wang Z, Ding X, Koizumi Y, Bian H, Lin L, Chiba A: Impact of solute elements on detwinning in magnesium and its alloys. International Journal of Plasticity 91, 2017, 134-159. https://doi.org/10.1016/j.ijplas.2016.09.014.
35. Jain J, Poole WJ, Sinclair CW: The deformation behaviour of the magnesium alloy AZ80 at 77 and 293K. Materials Science and Engineering A 547, 2012, 128-137. https://doi.org/10.1016/j.msea.2012.04.003
36. Jain J, Zou J, Sinclair CW, Poole WJ: Double tensile twinning in a Mg-8Al-0.5Zn alloy. Journal of Microscopy 242 (1), 2011, 26-36. https://doi.org/10.1111/j.1365-2818.2010.03434.x.
37. Lou Y, Li L, Zhou J, Na L: Deformation behavior of Mg-8Al magnesium alloy compressed at medium and high temperatures. Materials Characterization 62 (3), 2011, 346-353. https://doi.org/10.1016/j.matchar.2011.01.004.
38. Syam P, Kondaiah V, Akhil K, Kumar V, Nagamani B, Jhansi K, Dumpala R, Venkateswarlu B, Ratna S: Effect of heat treatment on microstructure, microhardness and corrosion resistance of ZE41 Mg alloy. Koroze a ochrana materialu 63, 2019, 79-85. https://doi.org/10.2478/kom-2019-0010.
39. Jia H, Feng X, Yang Y: Influence of solution treatment on microstructure, mechanical and corrosion properties of Mg-4Zn alloy. Journal of Magnesium and Alloys 3 (3), 2015, 247-252. https://doi.org/10.1016/j.jma.2015.08.006.
40. Humphreys FJ: *Recrystallization of single-phase alloys*. In: Recrystallization and related annealing phenomena. 2nd edn. Elsevier, Australia, 2004, 215-267.
41. Han K, Hirth J, Embury J: Modeling the formation of twins and stacking faults in the ag-cu system. Acta materialia 49 (9), 2001, 1537-1540. https://doi.org/10.1016/S1359-6454(01)00057-X.
42. Duly D, Simon J.P, Brechet Y: On the competition between continuous and discontinuous precipitations in binary Mg-Al Alloys. Acta Metallurgica et Materialia 43(1), 1995, 101-106. https://doi.org/10.1016/0956-7151(95)90266-X.
43. Celotto S: TEM study of continuous precipitation in Mg-9wt%Al-1wt%Zn Alloy. Acta Materialia 48(8), 2000, 1775-1787. https://doi.org/10.1016/S1359-6454(00)00004-5.
44. Braszczyńska-Malik K.N, Kamieniak J: Non-standard heat treatment of cast AZ91 magnesium alloy. Archives of Foundry Engineering 8(1), 2008, 31-34.
45. Epler M: Structures by Precipitation from Solid Solution. In: Vander Voort GF (ed) Metallography and Microstructures, vol 9. ASM International, 2004, 134-139. https://doi.org/10.31399/asm.hb.v09.a0003731.
46. Mendis CL, Hono, K.: *Understanding precipitation processes in magnesium alloys*. In Fundamentals of Magnesium Alloy Metallurgy, Pekguleryuz MO, Kainer KU, Arslan KA, eds., Woodhead Publishing, 2013, 125-151. https://doi.org/10.1533/9780857097293.125.
47. Manna I: Discontinuous reactions in solids. International Materials Reviews 46 (2), 2013, 53-91. https://doi.org/10.1179/095066001101528402.
48. Łabanowski J, Olkowski T: Effect of microstructure on mechanical properties of BA1055 bronze castings. Archives of Foundry Engineering 14 (2), 2014, 73-78. https://doi.org/10.2478/afe-2014-0040.
49. Braszczyńska-Malik K: *Precipitates of Gamma-$Mg_{17}Al_{12}$ Phase in Mg-Al Alloys*. In: Magnesium Alloys-Design, Processing and Properties. IntechOpen, 2011. https://doi.org/10.5772/13115.
50. Crawley AF, Milliken KS: Precipitate morphology and orientation relationships in an aged Mg-9% Al-1% Zn-0.3% Mn alloy. Acta Metallurgica 22 (5), 1974, 557-562. https://doi.org/10.1016/0001-6160(74)90152-7.
51. Nie JF, Xiao XL, Luo CP, Muddle BC: Characterisation of precipitate phases in magnesium alloys using electron microdiffraction. Micron 32 (8), 2001, 857-863. https://doi.org/10.1016/S0968-4328(00)00094-9.
52. Matsukawa Y: Crystallography of precipitates in metals and alloys:(2) Impact of crystallography on precipitation hardening. In: Crystallography. IntechOpen, 2019. https://doi.org/10.5772/intechopen.84273.
53. Horst E, Friedrich BLM: *Physical Metallurgy - Chapter 3*. In: Magnesium Technology, Design Data, Applications. Springer, 2006. http://doi.org/10.1007/3-540-30812-1_3.

ACTA METALLURGICA SLOVACA
2020, VOL. 26, NO. 4, 178-183

RESEARCH PAPER

ANALYSIS OF PLASTIC FORMING PARAMETERS IN AISI 441 STAINLESS STEEL

Orlando Di Pietro[1], Giuseppe Napoli[1], Matteo Gaggiotti[1], Roberto Marini[2], Giulia Stornelli[3], Andrea Di Schino[1]

[1]Engineering Department, University of Perugia, Via G. Duranti 93, 06125, Perugia, Italy

[2]Acciai speciali terni S.p.A., Viale B. Brin, 05100 Terni

[3]University of Rome "Tor Vergata", Department of Industrial Engineering, Via del Politecnico 1, 00133 Rome, Italy

*Correspondence: andrea.dischino@unipg.it, Engineering Department, University of Perugia, Via G. Duranti 93, 06125, Perugia, Italy

Received: 26.08.2020
Accepted: 10.09.2020

ABSTRACT

Plastic deformation is the most common technique adopted to manufacture complex shape pieces in the most efficient way. Even higher requirements need to be faced in the different applications. In order to target such requirement quality and compliance tests are carried out aimed to guarantee that these standards are faced. This often means a waste of material and economic resources. A far as concerns welded stainless steel pipes many criticises affecting the general trend of subsequent machining need to be considered. Such critical issues are more evident in the case of ferritic stainless steel with respect to austenitic ones. Therefore, the study of operating and geometric parameters is fundamental in the production process of ferritic stainless-steel tubes, whose use is mainly for the automotive industry. The possibility to simulate by finite element method (FEM) allows to evaluate the effect of geometric parameters and process constraints on plastic deformation tubes capability, thus allowing to properly fit the plastic deformation process to the target shape as a function of the adopted steel.

Keywords: stainless steel; forming process; mechanical properties

INTRODUCTION

The high mechanical and corrosion resistance [1, 2] allows stainless steels to be used in a wide variety of fields like automotive [3, 5], aeronautical [6-8], food [9, 10], energy [11, 12], sintered [13, 14] and three-dimensional (3D) printing [15, 16]. In automotive industry the forming process allow to produce very complex geometries, [17, 18] and up today several tests are carried out to validate the quality with the subsequent requirement of very high times and costs. This is still of greater importance in aeronautical industry: in the last years, a lot of research papers have been published has been concerning materials for aeronautics [19-21]. Relevant results have been achieved in preparing structural and engine metal alloys with optimized properties [22, 23]. The choice of the material to be adopted strongly depends on the type of component, owing to specific stress conditions, geometric limits, environment, production and maintenance [24, 25]. The strong competition in the industrial aeronautic sector pushes towards the production of aircrafts with reduced operating costs, namely, extended service life, better fuel efficiency, increased payload and flight range. From this perspective, the development of new materials and/or materials with improved characteristics is one of the key factors [26]. As a matter of fact in the aeronautical industry, even a tendency to progressively replace steels by composite is growing, stainless steels are still are commonly used for manufacturing aircraft parts such as landing gears, airframes, turbine components, fasteners, shafts, springs, bolts, propeller cones and axles [27, 28]. A successful solution able to optimize the production process reducing costs and times, is the realization of models that allow to simulate the procedure and confirm the quality of product. The numerical simulation is nowadays an essential tool able to improve the production process in terms of reliability and sustainability; through this method is possible to reduce time to market, cost of developing new components and to have a much more accurate knowledge of processing conditions, like forming [29-32]. The finite element method (FEM) is one of this approach mainly used for the prediction of forming car body parts [33-35], in fact is extremely important guarantee a proper procedure of tube bending and a correct simulation of pipe yielding after bending. During the analysis is also necessary to consider the impact of previous production process which create dispersion in mechanical properties and which show a character no longer deterministic bust stochastic. The plastic deformation of pipes caused by mechanical processing, leads an anisotropic behavior which must be studied by mathematical models; Von Mises and Johnson-Cook [36, 37] criteria for example describe the elastic-plastic behavior of isotropic materials, Hill's criterion instead defines the equations for orthotropic and anisotropic materials [38, 39].

In this paper is used a commercial software package adopting Hill's criterion to study the deformation process of ferritic stainless-steel tubes and the results are compared to those resulting from experimental test.

MATERIAL AND METHODS

The material studied in this paper is an AISI 441 stainless steel (X2CrTiNb18 – EN 1.4509). The chemical analysis of the adopted steel is reported in Table 1.

Table 1 Chemical analysis of AISI 441 (main elements, mass %)

Steel grade	C	Cr	Ni	Mo	Others
AISI 441	0.02	17.5-18.5	-	-	TI+NB=0.55%

Pipes with outer diameter OD ranging from 40 to 60 mm and thickness ranging from 1.0 to 1.8 mm are considered (Table 2).

Table 2 Materials used for simulations with their geometric characteristics

Steel grade	Tube diameter (mm)	Tube thickness (mm)
AISI 441	40; 45; 50; 55; 60	1.0; 1.2; 1.5; 1.8

Steel cold rolled and annealed coils are transformed into tubes. The tube has been then welded adopting laser or high-frequency welding techniques [40, 41]. Examples of welded joints microstructure as achieved in the AISI 441 steel by such techniques are reported in Figure 1.
The tube is then tested based on the UNI EN 69892 (6892-1 e - 2) standard.
Tubes are bended according to a process including the adoption of a mandrel, with an upper pressure die of 750 mm and an offset swiper die of 100 mm.
The maximum steel deformation capacity is reported in a type of diagram named *Formability Limit Curve* (FLC), contained in *Formability Limit Diagram* (FLD); these data are obtained by performing repeated Nakazima tests. The deformation process is studied by drawing a pattern of circles on the sample and is measured by the grid method: the circles distortion creates ellipses by which strains can be measured and on the FLD diagram is possible to identify the deformation state points of the material. This diagram, as shown in the Figure 2, contains the Formability Limit Curve (FLC) showing the maximum capacity of a material to be deformed, calculated by carrying out repeated drawing tests and measuring the ultimate breaking deformation along the two perpendicular directions.
The simulation of bending process on tubes with small diameters is carried out using a software that allows to exploit the Hill 48' yield function [42], taking into account parameters like bending radius, bending angle and rotational speed. The numerical calculations are carried out by means of Altair-HyperWorks™ (2017 version). The FEM model used in such investigation is based on the rigid-plastic variational principle and is reported in detail in [5]. The materials properties needed as input parameter for subsequent modelling include: steel density, Young modulus, Poisson ratio, Lankford value and strain hardening coefficient. Numerical values of such properties as adopted in the following calculations are reported in Table 3.The outputs calculated by the software are mapped to obtain information like internal stress, thinning and deformation; the maximum values observed on the grid will be considered the critical point on the geometry. An example of the obtained maps is reported in Figure 3.

a

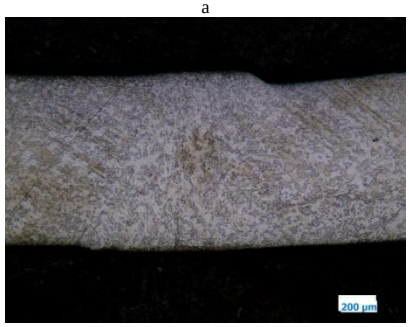

b

Fig. 1 Examples of welded joins in AISI 441 stainless steel tubes. a) laser welded joint, b) high-frequency welded joint

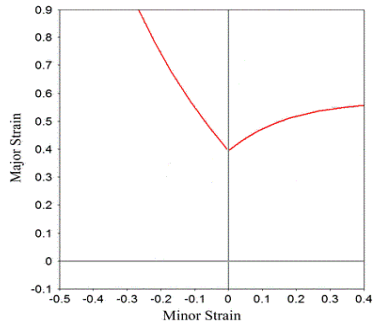

a

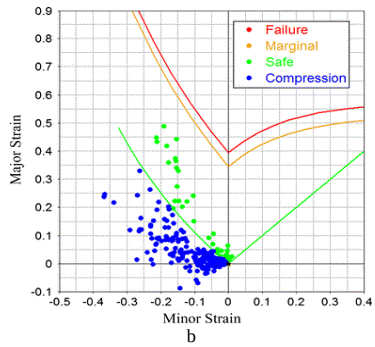

b

Fig. 2 Formability Limit Curve (a); Formability Limit Diagram with deformation state points (b)

Table 3 Steel properties valued adopted in the calculations

Density $\left[\frac{g}{cm^3}\right]$	Young modulus $\left[\frac{N}{mm^2}\right]$	Poisson ratio	Lankford value	Strain hardening
7.8×10^{-9}	210000.0	0.30	1.30–1.40	0.20–0.25

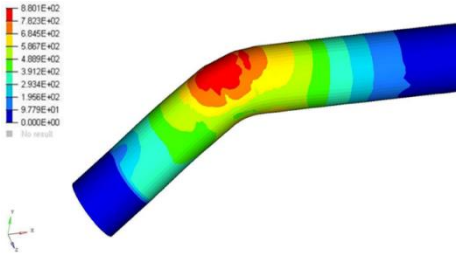

Fig. 3 Stress mapping on tube ben

RESULTS AND DISCUSSION

In the following paragraphs are reported the effects of plastic deformation on the geometry of the tubes.

3.1 Tubes diameter effect

In Figure 4 the stresses behavior as function of the diameters is shown. Results show an effect of approximately 5% of the tubes diameter on the stresses. A similar effect is visible on the tube thinning in Figure 5.

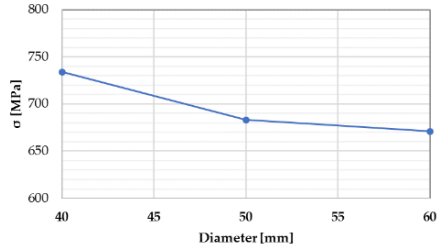

Fig. 4 Mean maximum stress behavior as a function of diameter size for AISI 441 steel - 1.5 mm thickness

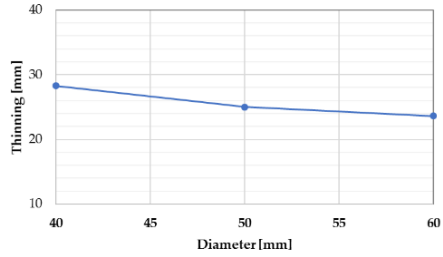

Fig. 5 Maximum thinning as a function of diameter size for AISI 441 steel - 1.5 mm thickness

The results are carried out fixing the ratio between bend radius and diameter R/D at 1.0 value.
The FLD diagrams in Figure 6 reports the behavior of the AISI 441 stainless steel with a diameter sizes ranged between 40 mm and 60 mm; such figure confirms that increasing the diameter decreases considerably the breakage risk.

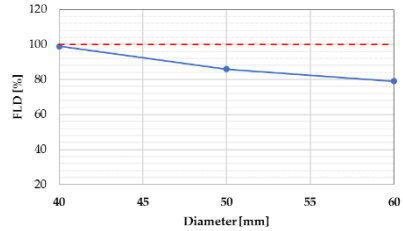

Fig. 6 Formability limit percentage as a function of the tube's diameter for AISI 441 - 1.5 thickness

3.2 Tube thickness effect

The mapping of stresses as a function of thickness is clearly shown in Figure 7, Results report about a not significative stresses distributions (< 2%) when thickness is varied. Different behavior is shown in Figure 8 instead, in which the thinning percentage increases as the tube's thickness increases (variation about 6%).

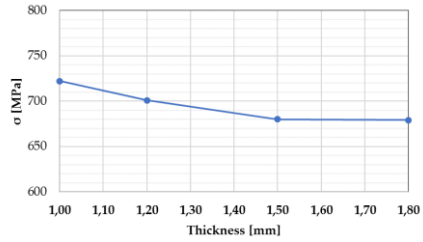

Fig. 7 Mean maximum stress behavior as a function of thickness for AISI 441 steel - 50 mm diameter

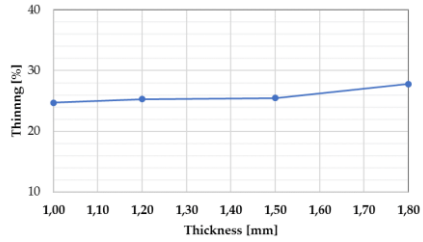

Fig. 8 Maximum thinning as a function of diameter size for AISI 441 steel - 50 mm

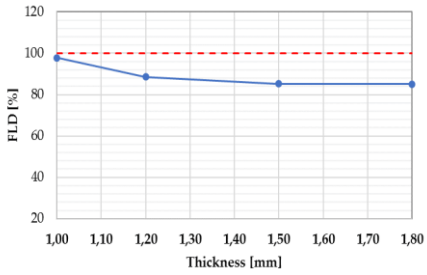

Fig. 9 Formability limit percentage as a function of the thickness for AISI 441 - 50 mm diameter

The FLD plot in function of tube's thickness (Figure 9), shows that an increase of thickness improves the success of bending process.

3.3 Speed rate and bend angle effect

In this section is analyzed the influence of speed variation for bending angle in a common manufacture process range (30° and 90°), in Figure10a and Figure 10b is shown the percentage of formability limit for the combination of angle and thickness. In particular, the geometric parameters were fixed together with the relationship between the diameter and the thickness.

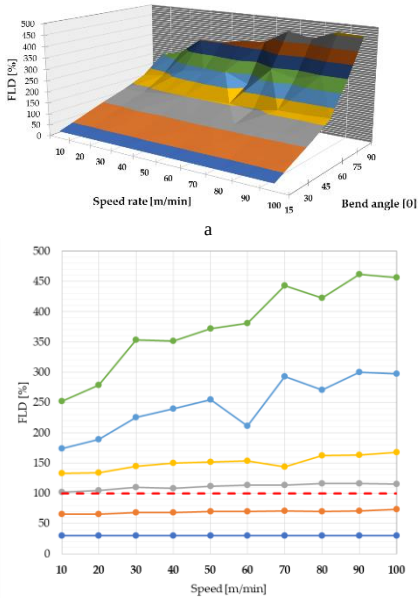

Fig. 10 Graph 3D (**a**) and 2D (**b**) of formability limit percentage for each speed and angle combination

Figure 10 reports an interpolation of data shown in Figure 9b, to have a better vision of the speed rate influence. For this reason, the percentage variation between the percentages of formability limits obtained at minimum and maximum feed speed for each angle, calculated according to equation (1), is reported in Figure 12.

$$\Delta FLD = FLDv_{max} - FLDv_{min} \quad (1.)$$

In Figure 12 is possible to see that, in the angle region ranging the 30° and 90° degrees, ΔFLD is related to the slope of interpolated line and this parameter varies almost linearly to the bend angle.

To have a more specified analysis, the study has been repeated using values that fit better the industrial process, the curvature radius was increased, the interpolations were re-performed (Figure 13) and FLD deltas were calculated for the new data obtained.

Figure 14 shows the importance of R/D ratio on the process, the improvement of this parameter in fact leads to an improvement in the sample formability; the ΔFLD increases in the bending angle range 30° - 90° and then tends to be stable away from breaking conditions.

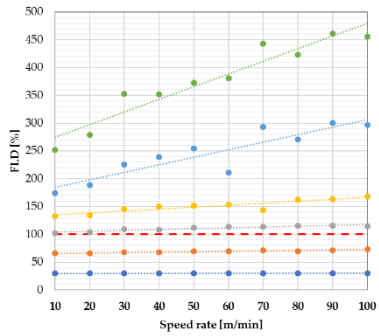

Fig. 11 Linear interpolation of the percentage of the radius of the formability limit for each combination of speed and angle

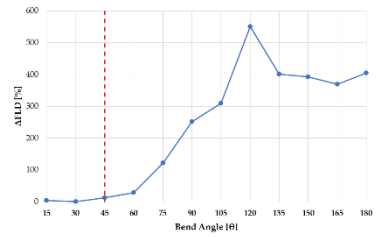

Fig. 12 Goodness of the simulation output beyond the breaking of the worked piece (red dotted line)

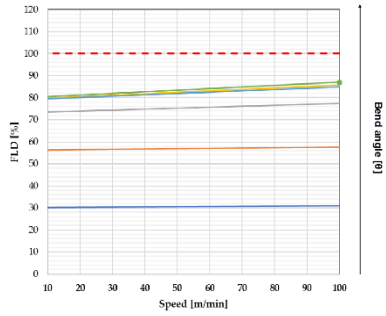

Fig. 13 Improved linear interpolation of the new percentages reached for the formability limit for each combination of speed angle

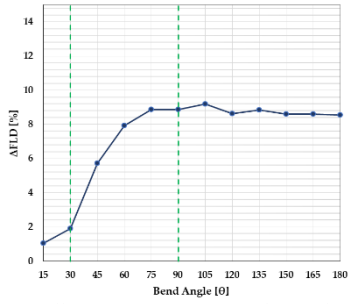

Fig. 14 New difference in the percentage of radii of the formability limit between minimum and maximum speed as a function of the bend angle

3.4 Ratio between bend radius and tube diameter effect

The R/D ratio is a parameter really important in industrial process, in standard conditions the value is between 1.0 and 1.5, in fact for values below 1 the risk of breakage increases. In this case is fixed an R/D = 1 because 1.5 is not used in the automotive field. Performing the simulations with a constant diameter, increasing the bend radius, results show that the stresses do not vary significantly (Figure 15). On the other hand a marked R/D ratio effect is found on the tube's thinning (Figure 16).

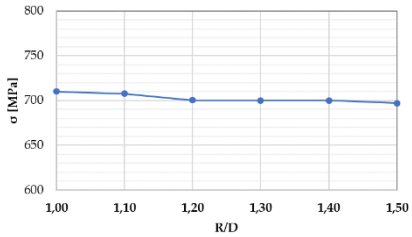

Fig. 15 Maximum equivalent stress dependence on a R/D ratio

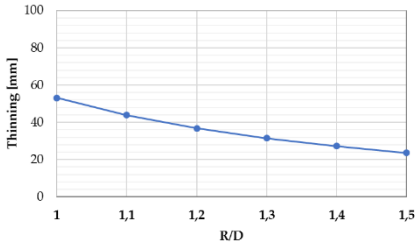

Fig. 16 Maximum equivalent stress dependence on a R/D ratio

CONCLUSION

This paper analyzes the influence of geometric and operational parameters on the bending process of AISI 441 ferritic stainless-steel pipes. It is evaluated an effect of about 5% of tube's diameter on internal stress and the thickness of the tube seems to be a determining factor for the failure and/or undesired deformation of the piece. The variation within the standard industrial operational range (between 1.0 and 1.5) of the R/D ratio, is extremely important because identified the transition between the failure and the success of the operation. Particularly for AISI 441 the variation of this parameter leads to a 60% increase in feasibility. The study of bending angle and speed carried out on the rotational, has shown the tendency to diverge and consequently to have inaccurate results when breaking the piece.

Staying in the non-breaking field instead, allowed to define a trend of influence for these operating parameters, showing how the increase in influence of the rotational speed has a strong impact on the feasibility of the process in the area between 30° and 90° of the angle of fold, while for greater angles there is a stabilization of the results and an effect of variation gradually less.

REFERENCES

1. P. Marshall: *Austenitic Stainless Steels: Microstructure and Mechanical Properties*. Elsevier Applied Science Publisher, Amsterdam, 1984
2. A. Di Schino,Metals, 10, 2020, 327. https://doi.org/10.3390/met10030327
3. W. Liu, J. Lian, J. Munstermann, C. Zeng: Fang, Int. J. of Mech. Sci., 176, 2020, 105534. https://doi.org/10.1016/j.ijmecsci.2020.105534
R. Rufini, O. Di Pietro, A. Di Schino: Metals, 8, 2018, 519. https://doi.org/10.3390/met8070519
4. O. Di Pietro, G. Napoli, M. Gaggiotti, R. Marini, A. Di Schino: Metals, 10, 2020, 1013. https://doi.org/10.3390/met10081013
5. A. Di Schino, L. Alleva, M. Guagnelli: Materials Science Forum, 715-716, 2012, 860. https://doi.org/10.4028/www.scientific.net/MSF.715-716.860
6. A. Di Schino, P.E. Di Nunzio: Acta Metall. Slovaca, 23, 2017, 62. https://doi.org/10.12776/ams.v23i1.852
7. G. Napoli, A. Di Schino, M. Paura, T. Vela: Metalurgija, 57, 2018, 111.
8. A. Di Schino, L. Valentini, J.M. Kenny, Y. Gerbig, I. Ahmed, H. Haefke: Surf. Coat. Technol. 161, 2002, 224. https://doi.org/10.1016/S0257-8972(02)00557-1
9. L. Valentini, A. Di Schino, J.M. Kenny, Y. Gerbig,, H. Haefke: Wear, 253, 2002, 458. https://doi.org/10.1016/S0043-1648(02)00140-0
10. D.K. Sharma, M. Filipponi, A. Di Schino,F. Rossi, J. Castaldi: Metalurgija, 58, 2019, 347.
11. A. Di Schino, C. Testani: Metals 10, 2020, 552. https://doi.org/10.3390/met10040552
12. Z. Brytan, M. Actis Grande, M. Rosso, R. Bidulsky, L.A. Dobrzansky: Materials Science Forum, 627, 2011, 165. https://doi.org/10.4028/www.scientific.net/MSF.672.165
13. R. Bidulsky, M. Actis Grande, E. Dudrova, M. Kabatova, J. Bidulska: Powder Metallurgy, 59, 2016, 121. https://doi.org/10.1179/1743290115Y.0000000022
14. C. Zitelli, P. Folgarait, A. Di Schino: Metals, 9, 2019, 731. https://doi.org/10.3390/met9070731
15. M. Ridolfi, P. Folgarait, A. Di Schino: Materials 13, 2020, 1424. https://doi.org/10.3390/ma13061424
16. K.H. Lo, C.H. She, J.K.L. Lai: Mat. Sci. Eng. R, 65, 2009, 39. https://doi.org/10.1016/j.mser.2009.03.001
17. L. Gardner: Prog. Struct. Eng. Mat., 7, 2005, 45. https://doi.org/10.1002/pse.190
18. F.C. Campbell: *Manufacturing Technology for Aerospace Structural Materials*. Elsevier: Amsterdam, Netherlands, 2006.
19. X. Zhang, Y. Chen, J. Hu: Prog. Aerosp. Sci. 2018, 97, 22. https://doi.org/10.1016/j.paerosci.2018.01.001
20. Z: Huda, P. Edi: Mater. Des. 2013, 46, 552. https://doi.org/10.1016/j.matdes.2012.10.001
21. J. Schijve: *Fatigue of Structures and Materials*. Kluwer Academic Publishers: Dordrecht, Netherlands, 2001.
22. J. J. Cwiek: Achiev. Mater. Manuf. Eng. 43, 2010, 214.
23. W. W Jian et al.: Mater. Res. Lett., 1, 2013, 61. https://doi.org/10.1080/21663831.2013.765927
24. K. Lu. S. Suresh: Science 2009, 324, 349. https://doi.org/10.1126/science.1159610
25. A. Gloria, R. Montanari, M. Richetta, A. Varone: Metals. 9, 2019, 662. https://doi.org/10.3390/met9060662
26. R.L. Klueh, D.S. Gelles, S. Jitsukawa, A. Kimura, G.R. Odette, B. van der Schaaf, M. Victoria,: Nucl. Mater. 2002, 307–311, 455. https://doi.org/10.1016/S0022-3115(02)01082-6
27. M. Wang, Z. Zhou, H. Sun, H. Hu, L. Li: Mater. Sci. Eng. A 2013, 559, 287. https://doi.org/10.1016/j.msea.2012.08.099
28. M.C. Oliveira, J.B. Fernandes: Metals, 9, 2019, 1356. https://doi.org/10.3390/met9121356
29. A .Cherouat, H. Borouchaki, J. Zhang: Metals, 8, 2018, 991. https://doi.org/10.3390/met8120991
30. T. Kvackaj et al.: J. Mater. Eng. Perform., 29, 2020, 1509. https://doi.org/10.1007/s11665-020-04561-y
31. T. Kvackaj et al.: Arch. Metall. Mater., 58, 2013, 407. https://doi.org/10.2478/amm-2013-0008

32. P. Mulidran, M. Siser, J. Slota, E. Spisak, T. Sleziak: Metals, 8, 2018, 435. https://doi.org/10.3390/met8060435
33. M. Mei, G. Khun, Y. He: Chin. J. Aeron., 29, 2016, 305. https://doi.org/10.1016/j.cja.2015.10.011
34. H.J. Bong, F. Barlat,, M. Lee, D.C. Ahn: Int. J. Mech. Sci. 2012, 64, 1. https://doi.org/10.1016/j.ijmecsci.2012.08.009
35. T. Scott, H. Kotadia: Mater. Charact. 163, 2020, 110288. https://doi.org/10.1016/j.matchar.2020.110288
36. S: Wang et al.: Mater. Lett. 2019, 342. https://doi.org/10.1016/j.matdes.2019.108355
37. M. Kaushal, Y.M. Moshi: Soft Matter, 15, 2019, 4915. https://doi.org/10.1039/C9SM00492K
38. O. Cazacu, B. Revil-Baudard, N. Chandola: *Plasticity-Damage Couplings: From Single Crystal to Polycrystalline Materials*. Solid Mechanics and its applications, Vol. 253, Springer International Publishing: Zurich, Switzerland, 2019. https://doi.org/10.1007/978-3-319-92922-4
39. L.D. Frame: Welding Journal, 2012, 34.
40. A. Di Schino, P.E. Di Nunzio, G.L. Turconi: Mater. Sci. Forum, 558-559, 2007, 1435. https://doi.org/10.4028/0-87849-443-x.1435
41. T.B. Yang, Z.Q. Yu, C.B. Xu, S.X. Li: J. Shanghai Jiaotong Univ.,45, 2011, 6.

ACTA METALLURGICA SLOVACA
2020, VOL. 26, NO. 4, 184-187

RESEARCH PAPER

INTERMETALLIC COMPOUNDS FORMATION OF SOLDER ALLOYS ON Ni/Au SURFACE FINISH COPPER

Binh Ngoc Duong[1]

[1]School of Materials Science and Engineering, Hanoi University of Science and Technology, Hanoi, Vietnam

*Corresponding author: binh.duongngoc@hust.edu.vn, tel.: +84 973 002988, School of Materials Science and Engineering/Hanoi University of Science and Technology, Hanoi, Vietnam

Received: 08.10.2020
Accepted: 29.11.2020

ABSTRACT

Intermetallic compounds (IMCs) formation between lead-free solder alloys (Sn-9Zn and Sn-8Zn-3Bi) and Ni/Au surface finish copper substrate were studied. Reaction between the solder and the substrate was carried out at regular soldering temperature, approx. 50 °C above the melting temperature of the solder alloys. Results indicated that Au-Zn was the IMC formed at the interface and the Au layer which is electro-plated on the substrate has completely dissolved into the solder alloys. The amount of Au available at the interface is an important factor that influent the morphology of the IMC with thicker Au layer on the substrate resulted in thicker layer of IMC at the interface. Although Bi does not taken part in the composition of IMC, it influent the formation of IMC, the IMC formed in the Sn9Zn/substrate interface was Au_5Zn_3, meanwhile it was γ_2-$AuZn_3$ in the Sn-8Zn-3Bi/substrate interface.

Keywords: intermetallic compound, solder alloy, Ni/Au surface finish

INTRODUCTION

In electronic products, all the common base materials, coatings, metallizations such as Cu, Ni, and Au, form intermetallic compounds (IMCs) with Sn, which is generally accepted to be the major element in solder alloys [1-4]. Therefore, during soldering, chemical reactions occur between solder alloys and conductor metals and IMCs will nucleate and grow at the solder/conductor interfaces.

It is well known that the presence of IMCs between solders and conductor metals is an indication of good metallurgical bonding. A thin, continuous and uniform IMC layer is an essential requirement for good bonding. However, due to their inherent brittle nature and the tendency to generate structural defects, too thick IMC layer at the solder/conductor metal interface may degrade the reliability of the solder joints [2,5-8]. Thus, knowledge of the solder/conductor metal interactions and phase evolution in the solder interconnections is important for the understanding of the reliability of the solder interconnections from the metallurgical viewpoint and for the optimization of the soldering process

Ni/Au surface finish is one of the important types of surface finish that have been widely used in the electronic industry. The surface finish consists of a layer of electro-plated Ni over the copper surface and a layer of Au which is electro-plated on the Ni surface. Ni is often used as a diffusion barrier layer between Cu and Sn, since the reaction rate of Ni with liquid Sn is typically smaller than that of Cu. The slower dissolution rate of Ni into Sn solders in comparison to Cu resulted in less IMC formation in the Ni-containing system [9]. It has been It has been reported that the Cu diffusivity in Sn is $2.5x10^{-7}$ cm^2/s [10] while Ni diffusivity in Sn is $5.4x10^{-9}$ cm^2/s at a temperature above 160 °C [11]. Thus, it is expected that due to the slower diffusivity of Ni, Ni tends to block the diffusion path of Cu at the Sn grain boundaries which leads to less IMC formation.

Au coatings have been used for a long time to protect conductor surfaces from oxidation and thereby to promote the solderability of the substrate [1,2]. Gold dissolves rapidly into Sn-based solder alloys [4,9], the system is characterized by a series of peritectic reactions and several intermediate phases exist in the system. The intermetallic phases of interest are hexagonal Au-Sn, showing a very small homogeneity range between 50.0 and 50.5 at.% Sn, orthorhombic $AuSn_2$ and orthorhombic $AuSn_4$ [12-14]. From the soldering point of view, the most interesting Au–Sn intermetallic is $AuSn_4$, because it is usually the first phase to form when using Sn-based Pb-free solders on conductor metals having thin Au coating [15]. However, when the solder has a sufficient amount of Zn, Au-Zn IMC will be the first phase to form. The reaction continued and the Zn content in the solder was gradually decreased. The formation of Au-Sn IMC will start if the amount of Zn in the solder reduces to approx. less than 3% [16].

Here in, reaction of lead-free solder alloys (Sn-9Zn and Sn-8Zn-3Bi) and the Ni/Au surface finish copper was carried out at 50 °C above the solder melting temperatures. Types of IMC formed at the solder/substrate interface and their morphology were extensively studied.

MATERIAL AND METHODS

Sn-9Zn and Sn-8Zn-3Bi solder pastes used in this study were obtained from Nihon Almit Co. Ltd., Japan. The Au/Ni surface finish copper substrate were purchased from Mitsui Mining and Smelting Co., Ltd, Japan. The substrate is oxygen free high conductivity (OFHC) copper foil of 0.4 mm in thickness which was electro-plated with a 5 µm Ni layer and a thin layer of Au.

Substrate with three different thicknesses of the Au layer were used, 0.1 µm, 0.3 µm and 0.5 µm. Hereafter, the substrates were referred as Au01, Au03 and Au05, respectively.
Copper substrate was cut into square of 30x30 mm and washed with acetone to remove surface tarnish. A cylindrical metallic mould was used to cast the solder pastes on substrate, the cylinder of solder paste has the dimension of 1.5 mm in height and 6 mm in diameter. The solder-substrate system was then placed above a metallic liquid bath which is kept at 50 °C above the melting temperature of the solder alloy for approx. 30 second. The specimen then removed from the metallic liquid bath and allowed to cold in air.
Morphological structures and composition of the IMCs form between the solders and the substrate were characterized by Scanning electron microscopy (SEM) and Energy Dispersive X-Ray Analysis (EDX)

RESULTS AND DISCUSSION

Sn-9Zn solder alloy

Figure 1 is a SEM image of the solder/substrate interface when Au05 substrate was used. As can be seen, a uniform layer of IMC was formed at the interface, the IMC layer is about 3 µm average in thickness. Point Energy Dispersive X-ray (EDX) analysis (Figure 2) shows that the IMC layer is an Au-Zn compound with the composition of 16.57 wt.% Zn and 83.43 wt.%Au (37.43 at.% Zn and 62.57 at.% Au). According to Au-Zn phase diagram, the IMC was identified as Au_5Zn_3. It has been reported that when Au substrate was used, Au-Zn IMC is formed at the interface if the amount of Zn in the solder was greater than 3%. In this case, the amount of Zn is 9% which is much higher than the requirement, thus explain the formation of Au-Zn IMC. The disappearing of Au layer at the interface means all the Au was reacted with Zn. The amount of Au available for reaction here was insufficient to depleted Zn in the solder from 9% to less than 3%, and thus Au-Sn IMC was not formed.

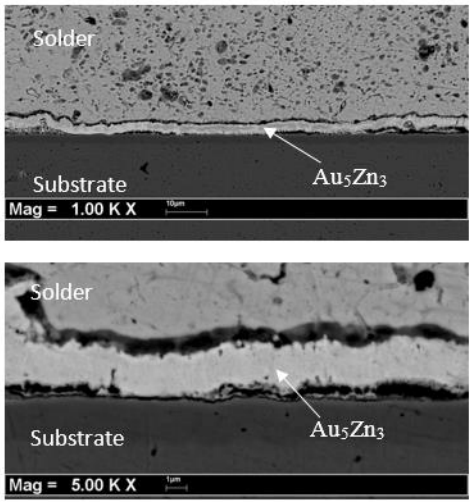

Fig. 1 SEM image of the Sn-9Zn/Au05 interface

The solder/substrate interface roughly consists of 4 layers; the copper, the Ni layer, the IMC layer, and the solder alloy. It's also noted that there is a thin, dark layer on the solder side of the IMC and some parts of the IMC are broken away from the Ni layer on the substrate. The thin layer on the solder side might be attributed to the Zn rich phase which was dissolved in the etching step while preparing SEM specimen (the etchant used was ferric chloride). A weak bond between IMC layer and the substrate could resulted in the IMC to break away from the surface and entering the solder.

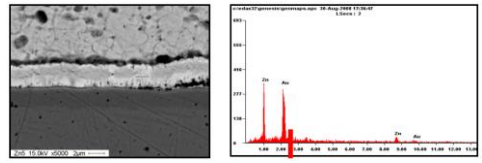

Fig. 2 EDX analysis of the IMC formed between Sn-9Zn and Au05 substrate

The morphologies of IMCs formed at the interface were difference and depended upon the thickness of Au layer on the substrate. On Au05 substrate, IMC forms a continuous layer which completely covered the substrate. The layer was thinner on the Au03 substrate, and almost become a discrete line on the Au01 substrate. The difference in thickness of IMC layers on substrate are shown in Fig. 3.

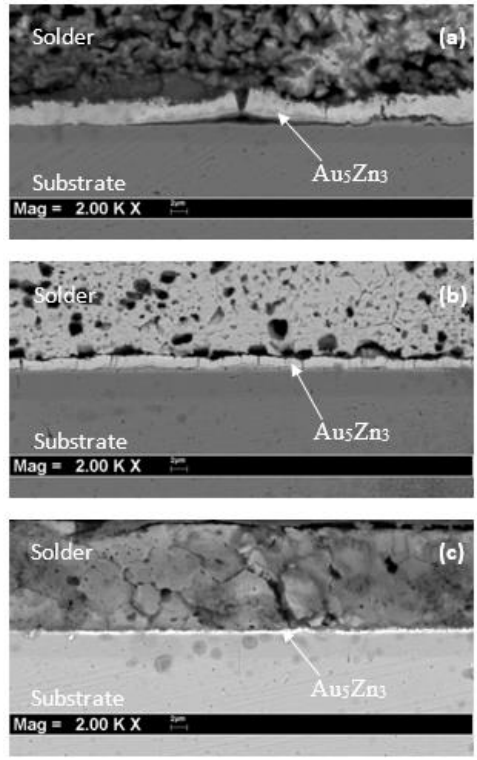

Fig. 3 SEM images of Sn-9Zn and Ni/Au surface finished copper substrate interface: (a) Au05, (b) Au03 and (c) Au01

The thickness of IMC layer on Au05 substrate was approx. 3 µm (Fig. 3a), whist that on the Au03 substrate was 1.3 µm (Fig. 3b) and the thinnest IMC was observed on the Au01

substrate, approx. 0.5 μm (Fig. 3c). As discussed above, a thin, continuous and uniform IMC layer is an essential requirement for good bonding. The thick IMC layers formed on Au03 and Au05 substrate might have weaken the bond between solder and substrate. Also, crack was already observed on those IMC layers, Figure 4 shows the interface of another specimen using Au03 substrate. The IMC layer was broken, and large pieces of IMC detaches from the interface and entering the solder.

A larger magnification SEM image of the interface when Au01 substrate was given in Figure 5. The IMC morphology is different from those formed on Au05 and Au03 substrates. Instead of a continuous layer, the IMC formed is in grain-like shape and aligns with the substrate surface. The difference in IMC morphology may due to the difference in the amount of Au available. Since there is no gold detected on the substrate surface after experiment, it can be suggested that all Au present on the substrate surface has reacted with the solder and formed the IMC. Due to different thicknesses of the Au layer, the amount of Au available on each substrate surface is different and therefore affects the formation of IMC. The difference IMC layers maybe due to the lack of Au and therefore, limited the amount of IMC formed.

It has been reported that the amount of Au available for reaction influents the morphology of IMC [5]. With little amount of Au, the Au containing IMCs were formed in small size and distributed in solder alloy. However, if there were more of Au present and the reaction time is long enough, then the IMC could form a continuous layer at the interface. Temperature and time of the soldering process have only a small effect on the morphology of the compounds. In this work, the morphology of the IMCs formed in the specimens varied depending on the substrate used. When Au05 substrate is used, there is plenty of Au available and the Au-Zn IMC formed a continuous layer (Figure 1). However, when the amount of Au decreases, as in the Au01 substrate, the IMC are grain-like in shape. Although Fig. 5 still depicted and alignment of IMC particles at the interface, it's possibility that the IMC particles will break away from the surface and scattered in the solder.

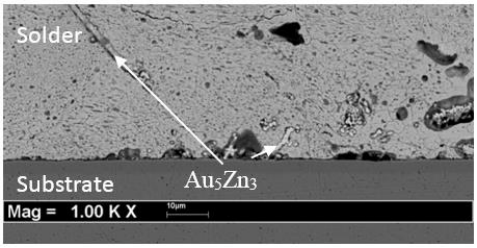

Fig. 4 IMC formed between Sn-9Zn and Au03 substrate

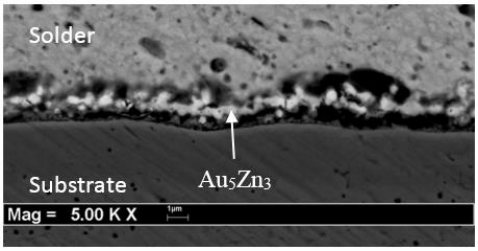

Fig. 5 IMC layer formed between Sn-9Zn and Au01 substrate

As mentioned by Laurila *et al.* [5], another requirement for the IMC to form a continuous layer is a long-enough reaction time. However, they did not specify how long should be considered long enough. In another study, Kim and Tu [12] studied the time dependence of the reaction between SnPb and Au and discovered that Au were able to react and formed IMC with Sn-based solder after only 2 seconds. Therefore, the experimental time in this study, which is 30 seconds, can be considered long enough for IMC to form a continuous layer. The experiment results confirmed a continuous IMC layer was formed at the interface when a substrate with thicker Au layer is used.

The interfacial reactions between Ni and Sn-based solder alloys have been investigated in a number of studies [17-20]. Most studies have identified Ni_3Sn_4 as the reaction product formed after soldering. This necessitates that solders used do not contain Cu and that there are no other Cu sources such as component or board metallization. Otherwise $(Ni,Cu)_6Sn_5$ would form. The formation of $(Ni,Cu)_6Sn_5$ precipitates on the Ni layer takes place rapidly during soldering [5]. In this case, the formation of Au-Zn IMC at the interface somehow limited the formation of Ni containing IMC. Since the Au layer was completely dissolved and the Au-Zn IMC layer wasn't completely covered the substrate's surface, the Ni layer could be in direct contact with the solder alloy. However, there wasn't any Ni-Sn IMC found in the specimen. Also, there is no Cu in the solder alloy and thus, $(Ni,Cu)_6Sn_5$ was not found.

Sn-8Zn-3Bi solder alloy

Figure 6 shows the SEM images of the interface between Sn-8Zn-3Bi solder alloy and Ni/Au surface finish substrates.

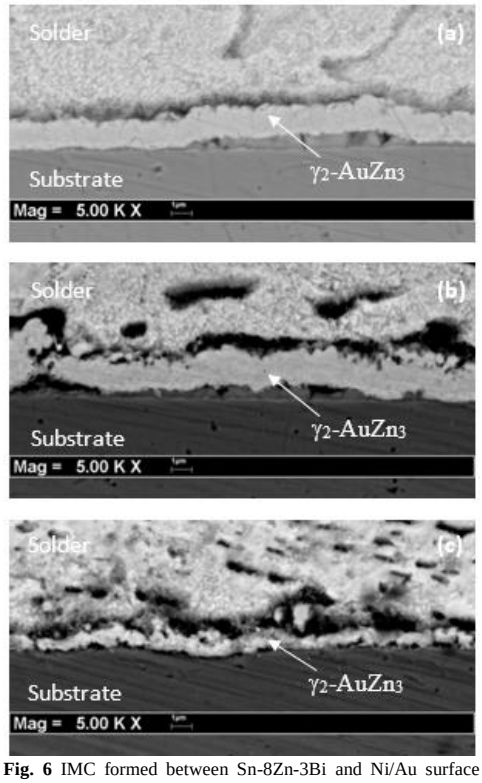

Fig. 6 IMC formed between Sn-8Zn-3Bi and Ni/Au surface finished copper substrate: (a) Au05, (b) Au03 and (c) Au01

Similar to the interface of Sn-9Zn and Ni/Au surface finish substrate, a thick layer of IMC is formed at the solder/substrate interface when Au05 is used (approx. 2 µm). When the substrate with thinner Au layer was used, thinner IMC layers were formed at the interface. The difference in thickness of the IMC layers, as discussed above, was due to the difference of the Au amount available on the substrate. The Au01 substrate has the thinnest Au layer or the smallest amount of Au available, and thus, resulted in the thinnest IMC layer at the interface.

EDX analysis confirmed that the IMC was an Au-Zn intermetallic (Fig. 7), the IMC compositions were 50.9 wt.% Au and 49.1 wt.% Zn (25.60 at.% Au and 74.40 at.% Zn). According to the Au-Zn phase diagram, the IMC can be identified as γ_2-$AuZn_3$. The difference between IMC formed in the Sn-9Zn and Sn-8Zn-3Bi solder may due to the presence of Bi in the Sn-8Zn-3Bi solder. As mentioned above, the addition of Bi into Sn-Zn solder reduces the solder's melting temperature and also improves its wettability. Thus, this addition has influenced the process of IMC formation. Although Bi does not take part in the IMC, the presence of Bi has led to the formation of γ_2-$AuZn_3$ IMC instead of Au_5Zn_3 IMC.

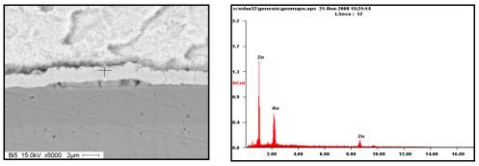

Fig. 7 EDX analysis result of IMC at Sn-8Zn-3Bi and Au05 substrate interface

The effect of Bi on the formation of IMC between solder and substrate was also reported by Ronka [21]. In their studies on the Cu/SnBi-eutectic system, they found that by changing the Bi composition (increase) led to the transformation of Cu_6Sn_5 to Cu_3Sn intermetallic. Since Bi does not react with other elements to form an intermetallic compound, the consumption of other elements to form IMC changes the local equilibrium condition (local composition changes as the composition of Bi increases). The change of local equilibrium condition leads to the transformation of the intermetallics.

CONCLUSION

During soldering, Sn-9Zn, Sn-8Zn-3Bi solder alloys reacted and formed IMCs with Ni/Au surface finish copper substrate. The Au_5Zn_3 IMC was form at the Sn-9Zn/substrate interface and it was the γ_2-$AuZn_3$ at the Sn-8Zn-3Bi/substrate interface. The difference in IMC composition could be attributed for the presented of Bi which was influence the local equilibrium condition in the process of IMC formation. The amount of Au available on the substrate's surface has influence the morphology of IMC formed. The thinner Au layer on the substrate, the thinner IMC layer at the interface and thus, ensure good bonding of the solder joint.

REFERENCES

1. M. Abtew, G. Selvaduray: Materials Science and Engineering Reports, 27(5-6), 2000, 95-141. https://doi.org/10.1016/S0927-796X(00)00010-3
2. K. N. Tu, K. Zeng: Materials Science and Engineering Reports, R34, 2001, 1–58. https://doi.org/10.1016/S0927-796X(01)00029-8
3. H. M. Howard: *Solders and Soldering*, 4th edition, New York: McGraw-Hill, 2001.
4. W.G. Bader: Welding Journal, 48(12), 1969, 551-557.
5. T. Laurila, V. Vuorinen, J.K. Kivilahti: Materials Science and Engineering R: 49(1-2), 2005, 1-60. https://doi.org/10.1016/j.mser.2005.03.001
7. P.L. Liu, J.K. Shang: Scripta Materialia, 53(6), 2005, 631-634. https://doi.org/10.1016/j.scriptamat.2005.05.033
8. C.M. Chen, C.H. Chen: Journal of Electronic Materials, 36, 2007, 1363-1371. https://doi.org/10.1007/s11664-007-0226-1
9. S.Bader, W.Gust, H.Hieber: Acta Metallurgica et Materialia, 43(1), 1995, 329-337. https://doi.org/10.1016/0956-7151(95)90289-9
10. B.F. Dyson, T.R. Anthony, D. Turnbull: Journal of Applied Physics, 38, 1967, 3408. https://doi.org/10.1063/1.1710127
11. F. Guo, J. Lee, S. Choi, J.P. Lucas, T.R. Bieler, K.N. Subramaniam: Journal of Electronic Materials, 30, 2001, 1073–1082. https://doi.org/10.1007/s11664-001-0132-x
12. M.S. Shin, Y.H. Kim: Journal of Electronic Materials, 32, 2003, 1448–1454. https://doi.org/10.1007/s11664-003-0114-2
13. R.R. Chromik, D.N. Wang, A. Shugar, L. Limata, M.R. Notis, R.P. Vinci: Journal of Materials Research, 20(8), 2005, 2161-2172. https://doi.org/10.1557/JMR.2005.0269
14. H.G. Song, J.W. Morris, M.T. McCormack: Journal of Electronic Materials, 29, 2000, 1038–1046. https://doi.org/10.1007/s11664-000-0170-9
15. P.G. Kim, K.N. Tu: Materials Chemistry and Physics, 53, 1998, 165-171. https://doi.org/10.1016/S0254-0584(97)02076-2
16. W.K. Liou, Y.W. Yen: Interfacial reactions between Sn-9Zn+Cu lead-free solders and the Au substrate, 2008 International Conference on Electronic Materials and Packaging, Taipei, Taiwan, IEEE, 2008. https://doi.org/10.1109/EMAP.2008.4784268
17. K. Zeng, K. N. Tu: Materials Science and Engineering R, 38(2), 2002, 55-105. https://doi.org/10.1016/S0927-796X(02)00007-4
18. W.J. Tomlinson, H.G. Rhodes: J. Mater. Sci., 22, 1987, 1769-1772. https://doi.org/10.1007/BF01132405
19. J.W. Yoon, C.B. Lee, S.B. Jung: Journal of Electronic Materials, 32(11), 2003, 1195-1202. https://doi.org/10.1007/s11664-003-0011-8
20. C.W. Hwang, K. Suganuma, M. Kiso, S. Hashimoto: Journal of Materials Research, 18(11), 2003, 2540-2543. https://doi.org/10.1557/JMR.2003.0354
21. K.J. Rönkä, F.J.J. van Loo, J.K. Kivilahti: Metallurgical and Materials Transactions A, 29, 1998, 2951–2956. https://doi.org/10.1007/s11661-998-0202-2